University of Strathclyde

Department of Physics

The Application of Quantum Cascade Lasers to Mid-Infrared Gas Sensing

by

Paul Richie Black

A thesis presented in fulfilment of the requirements for the degree of Doctor of Engineering

2011

This thesis is the result of the author's original research. It has been composed by the author and has not been previously submitted for examination which has led to the award of a degree.

This thesis is dedicated to my parents, John and Joyce Black.

Abstract

This thesis explains the development of a quantum cascade laser based gas sensor and the verification of performance of the resulting product. The capability to detect trace levels of multiple species in varying physical conditions, specifically high temperature is shown.

Optical designs capable of allowing the measurement technique to be used in a variety of applications have been developed, specifically multi-pass gas absorption cells. The accurate, precise and high speed analysis of the resulting data is made possible by spectral analysis algorithms. These developments and techniques were then applied to high temperature spectroscopic measurements. Spectra recorded at Rutherford Appleton Laboratory were used to calibrate high temperature measurements. The performance of the technology was thoroughly tested at the National Physical Laboratory. The resulting sensors have since been used to study the exhaust gases produced by a variety engine types ranging from cars to ships as well as atmospheric measurements.

Acknowledgements

First and foremost I would like to thank Prof. Geoff Duxbury, whose guidance and support have been invaluable and without whom I am sure I would not have completed this thesis. The research activities of the Quantum Cascade Laser group at the University of Strathclyde and specifically Dr. Nigel Langford, Stephen Wright and Kenneth Hay all furthered my own understanding of the subject.

The nature of the EngD degree is such that the majority of work is conducted in an industrial organisation within a team environment. Because of this much of the work that has been included in this thesis is the result of the efforts of my colleagues at Cascade Technologies. The experience of beginning at Cascade in its early stages and being there as it has grown to the company it is now has provided an unequalled environment for the EngD. Everyone who works at Cascade Technologies has contributed in some way to this thesis. Erwan Normand, Michael McCulloch, Iain Howieson, Raphael Cotty, Yann Hamonou, Ruth Lindley, Pete Hamilton and Barry Ferns all provided invaluable contributions.

Contents

List of Figures

List of Tables

Chapter 1

Introduction

1.1 Overview

The condition of the atmosphere has been a public issue for decades and research into the composition of the atmosphere has shown that the levels of greenhouse gases have been increasing at alarming rates. Figure 1.1 shows historic CO_2 concentrations in the atmosphere, obtained from ice core data [1] and the rising level that has followed the industrial revolution, obtained from infrared measurements of the atmosphere [2].

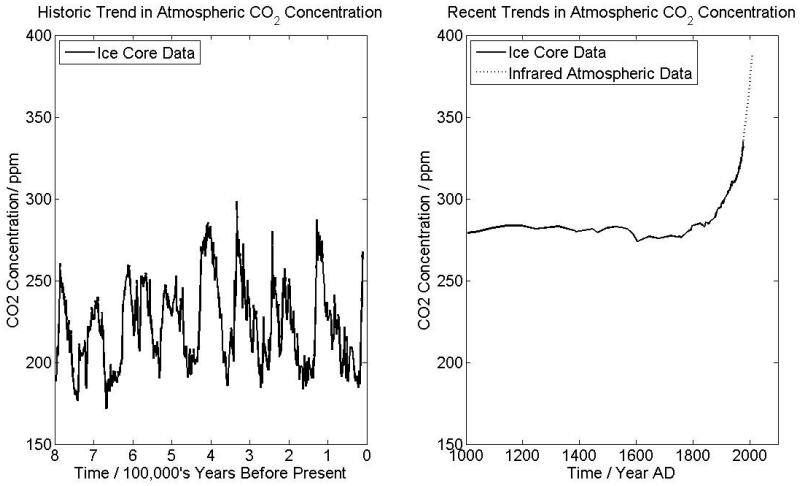

Figure 1.1: The historic trends in atmospheric CO_2 concentrations are compared with the rise following the industrial revolution. The historical measurements are obtained from analysis of ice core data [1]. The peaks and troughs in this data corrolates with global temperature. Infrared analysis [2] of the atmosphere shows the rising trend in CO_2 concentration.

In recent times efforts to combat the effects of pollution have become an issue of international importance. This arguably began with the 1956 Clean Air Act which followed the "Great Smog" of London in December 1952. The purpose of the act was to reduce air pollution and a reduction was observed following its introduction [3]. National and international legislation governing the emission of greenhouse gases is increasing in response to public concern. This leads to demand for methods of reducing emissions and for techniques to reliably and continuously monitoring the emission volumes of gases that can damage the environment.

The fundamental absorption transitions of many molecular species can be found in the mid-infrared region of the electromagnetic spectrum. Lead-salt semiconductor lasers have provided access to the mid-infrared region in the past, however the power output from these devices is low, they require cryogenic cooling and their spectral performance can be unreliable [4]. The quantum cascade (QC) laser, however is a high power device that does not require cryogenic cooling and is capable of accessing the mid-infrared wave-

lengths. The development of a gas detection method based on QC lasers from basic theory to a robust instrument that can operate in extreme environments is the basis of Chapters 2 and 3 where several key concepts are discussed. The testing and performance of prototype sensors based on these concepts is then demonstrated in Chapter 4. The last section of Chapter 4 discusses the results of measurements made on gases within low pressure flames.

1.2 Mid-infrared Spectroscopy

In broad terms, spectroscopy is concerned with the interaction of radiation and matter, although measurements are not necessarily made on the radiation itself. Spectroscopy can be split into different types based on the wavelength and type of radiation and the methods used to measure the interaction. Electromagnetic radiation can interact with matter by absorption, emission, polarisation and scattering processes.

There are a number of established spectroscopic techniques such as photo-acoustic spectroscopy, chemiluminescence, ion-mobility spectroscopy, electromagnetic absorption spectroscopy and Fourier transform spectroscopy [5, 6].

Photo-acoustic spectroscopy involves detecting an acoustic spectrum produced by a sample when the sample is exposed to laser light. When light is absorbed by a sample the electromagnetic energy is converted to kinetic energy and sound waves are produced from the sample. Information about the wavelength and intensity of the sound waves that are produced can be used to determine the content of the sample. The sound detection is performed by microphones and the resultant signal is often amplified by using a lock-in amplifier.

Chemiluminescence is the emission of electromagnetic radiation as a product of a chemical reaction. The intensity and wavelength of the emitted light can be monitored to characterise the identity and concentration of molecules.

An example is the reaction of nitric oxide with ozone, which produces a broad spectrum from the visible to the infrared.

Ion mobility spectroscopy (IMS) performs measurements by ionising samples which are introduced into drift cells where an electric field is applied to direct the ionised molecules towards a detector. Characteristics of the molecules such as the charge and mass define the expected time for migration, this allows the ionised compounds to be identified. IMS is a popular measurement technique for security applications such as passenger and baggage screening at airports.

Fourier transform spectroscopy is based on the interference of broadband light sources. A single source is split into two beams, the beams are recombined after reflection and the resultant beam is directed towards a detector. The optical path difference between the beams can be altered allowing an interferogram to be recorded by the detector. A Fourier transform of the interferogram produces a spectrum. Measurements are performed by directing the broadband light through a sample. High resolution spectra can be produced by this method, however precise measurements can take long times to collect and the instruments themselves can be bulky. Some of the work presented in this thesis involved the use of Fourier transform spectroscopy to investigate the accuracy and precision of computer simulations of absorption spectra.

This thesis is concerned largely with electromagnetic absorption spectroscopy and more specifically mid-infrared absorption spectroscopy. The mid-infrared range of the electromagnetic spectrum extends from approximately 2.5 to 20 μm (500-4000 cm^{-1}).

In absorption spectroscopy the interaction is measured by comparing the radiation before and after the interaction. In the case of the mid-infrared the absorption process takes place on a molecular level, the photon energy associated with the mid-infrared equates to vibrational or ro-vibrational transitions of many molecules. The spectra of different molecules are often easily distinguishable in this part of the electromagnetic spectrum which is why it

is often referred to as the fingerprint region. Also, the absorption lines of molecules in this region have the advantage of fundamental transitions with the strongest absorptions and are typically high enough to allow detection of trace level concentrations.

1.2.1 Vibrational and Ro-Vibrational Spectroscopy

Complex molecules can have many covalent bonds between the various atoms that the molecule is composed of. The atoms can vibrate and the molecule can rotate at specific frequencies which correspond to discrete energy levels or vibrational modes [5, 7]. This leads to infrared absorptions that are related to chemical groups. For example, the atoms in a methylene (CH_2) group, which is found in many simple compounds, vibrate in six different ways. Symmetrical and anti-symmetrical stretching involves a change in the length of a bond. Bending is a change in the angle between bonds, while rocking is a change in the angle between a group of atoms. Wagging and twisting involve changes in the angles of planes of atoms within the molecule. The spectra obtained from a species become more complex with an increasing number of infrared active bonds. Since the energy associated with the vibrational modes is dependent on the masses of the atoms involved the observed spectra can be used to identify the molecule under study. Examples of a mid-infrared Nitric Oxide (NO) spectrum and a Nitrogen Dioxide (NO_2) spectrum are shown in figure 1.2.

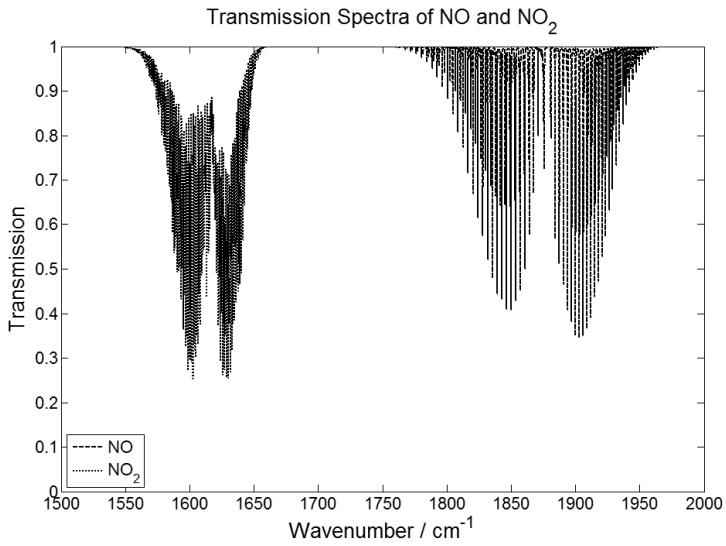

Figure 1.2: This figure shows an example of a mid-infrared spectrum of a simple molecule, Nitric Oxide (NO), together with a similar but slightly more complex molecule, Nitrogen Dioxide (NO_2).

1.3 Quantum Cascade Lasers

The Quantum Cascade (QC) laser is a type of semiconductor laser. Traditional semiconductor diode lasers utilise carrier transitions between the conduction and valence bands of the semiconductor. The recombination transitions are the basis for laser action within these devices. QC lasers are based on inter-subband transitions within the conduction band of the semiconductor, these transitions are possible due to semiconductor quantum wells within the device. The theory behind the QC laser was suggested in a paper from 1971 [8], however the fabrication technology available at the time made the device impossible to manufacture. It was not until 1994 that the first QC laser was constructed [9] using molecular beam epitaxy (MBE) fabrication methods. They are also known as unipolar, intersubband lasers since they involve transitions of only one type of carrier within only one energy band.

1.3.1 History

The quantum well heterostructure is created by sandwiching very thin layers of different semiconductors together; the difference in their respective energy bands leads to the spatial confinement of carriers. This causes the allowed energy of the carriers to become quantised into subband levels within the conduction band, as shown in figure 1.3. By manipulating the semiconductor materials used, layer thickness and doping concentrations, the energy gaps between the quantised subband energy levels can be altered. It is this change that determines the energy involved in a radiative transition and so the wavelength of light emitted.

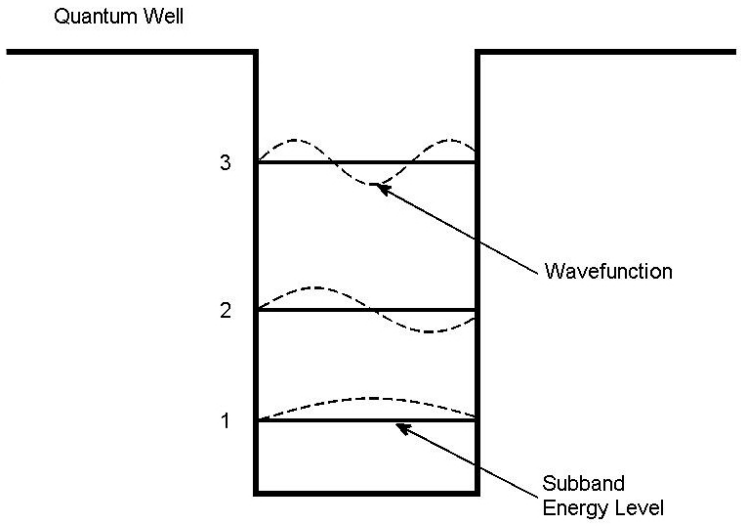

Figure 1.3: This figure shows an example of a quantum well in bold. The wave functions and the quantised subband energy levels are shown. The energy separation of the subbands allows radiative transitions to take place.

The first intersubband unipolar laser was invented and reported in 1994. Faist, Capasso, Sivco, Sirtori, Hutchinson and Cho developed the device at AT&T (Lucent Technologies) Bell Laboratories and they named it the Quantum Cascade (QC) laser. It was designed to emit at 4.3 μm and was made from a heterostructure of Al 0.48In 0.52As / Ga 0.47In 0.53As on an

InP material system, molecular beam epitaxy (MBE) was used to fabricate the device. When these layers are engineered to specific thicknesses and have an electric field applied to them, a cascade structure is created as shown in figure 1.4.

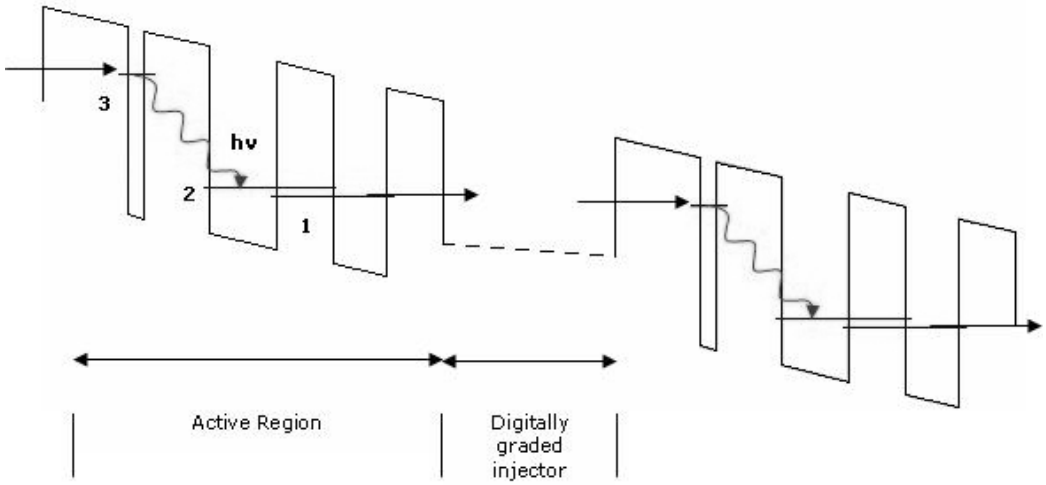

Figure 1.4: This shows a QC laser band diagram with the quantised energy levels where the significant transitions take place. The radiative diagonal transitions occur between energy levels 3 and 2. The effective conduction band edges of the injection regions are marked. An important aspect of these devices is that the carrier can be reused, when the carrier reaches energy level 1 it is injected into level 3 of the following active region.

Figure 1.4 shows the layers of semiconductor that lead to the cascade band structure. It begins with a 4.5nm AlInAs barrier that leads to the active region, which consists of 0.8nm and 3.5nm GaInAs wells separated by a 3.5nm AlInAs barrier and finally a 2.8nm GaInAs well between two 3nm AlInAs barriers. The confinement of the electrons to these wells results in three quantised energy levels as shown. Electrons are injected into the active region by means of resonant tunnelling through the AlInAs barriers. A photon-assisted or diagonal transition is made from level three to level two resulting in an emitted photon that corresponds to the energy gap of 295meV. This energy gap is equivalent to 4.3 μm, as shown in equation 1.1.

$$h\nu = E_3 - E_2 \tag{1.1}$$

The electrons then undergo a phonon transition to level 1 where they are injected into the next active region. The number of active regions in a QC laser is variable, however for the original device there were 25 injector/active regions meaning that each injected electron could in theory create up to 25 photons. A single injector/active region is equivalent to a 4-level laser system; a central requirement of laser operation is the ability to create a population inversion between levels 3 and 2. This is possible because the population inversion condition $\tau 32$ - $\tau 2 > 0$ is satisfied, where $\tau 32$ is the relaxation time from level 3 to level 2 and $\tau 2$ is the lifetime of carriers in level 2. This occurs because of the reduced spatial overlap of levels 2 & 3 and the large overlap and small gap between levels 1 & 2.

The original device was operated with an applied electric field of $\sim$105 V/cm and emitted with peak powers in excess of 8mW at $\sim$10K. The threshold current at this temperature was found to be 850mA. The device was operated up to a maximum temperature of 90K.

The following year (1995) saw advancements in the operation of QC lasers; a design involving vertical transitions, rather than diagonal transitions, was demonstrated [10], this is shown in figure 1.5. Vertical transitions were responsible for an increase in performance of QC lasers. Higher operating temperatures and output powers were achieved due to the reduction in threshold current density. A QC laser operating in continuous wave (cw) mode was demonstrated at cryogenic temperatures [11] and pulsed mode operation was demonstrated at room-temperature [12], this was also due to the inclusion of InP in the upper waveguide cladding since its thermal resistance was much smaller than the larger compounds of InAlAs.

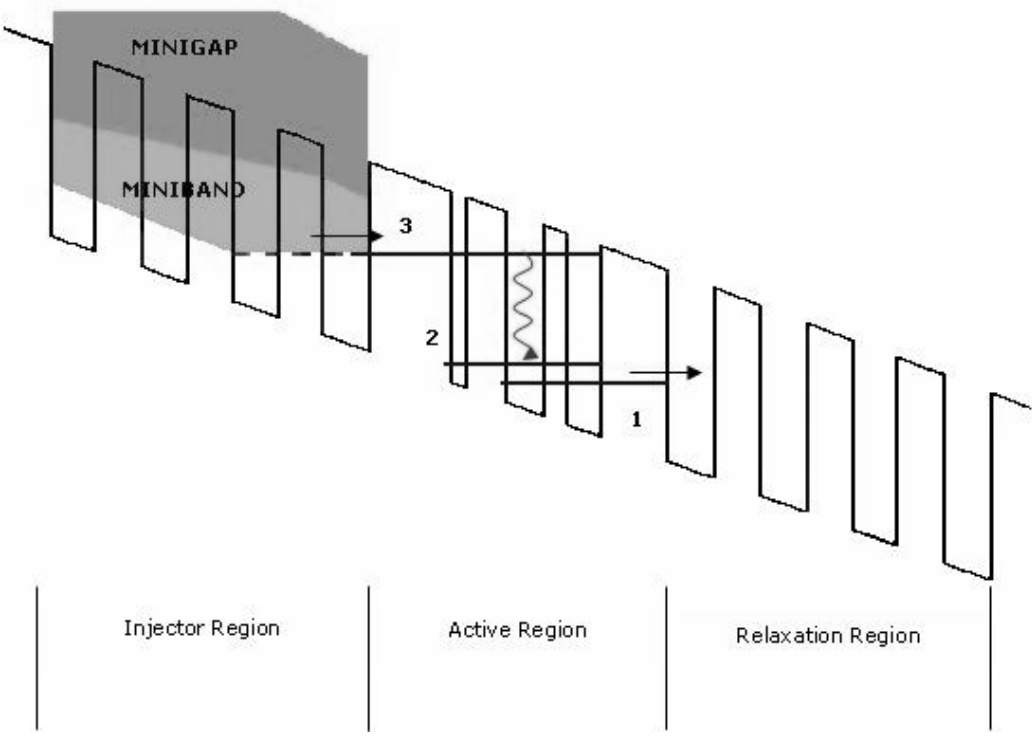

Figure 1.5: A QC laser Band diagram with vertical radiative transition. This shows a miniband energy level manifold and minigap area. The previous active region's relaxation region is used as the injector region of the current active region.

Among the improvements being made to QC lasers was waveguide design. The first distributed feedback (DFB) QC laser was created in 1996 [13], providing a continuously tunable single-mode laser output. Following the pursuit of higher power and longer wavelengths a superlattice active region quantum cascade laser (SL-QCL) was demonstrated in 1997 [14, 15]. This design incorporated minigaps and minibands in the injector/relaxation region of the QC laser as shown in figure 1.5. These allow an intrinsic population inversion to be created rather than relying on the design of the lasers quantum wells and therefore larger current flow is possible. This leads to an increase in optical output power and allows longer wavelengths to be emitted, which need an active region that can manage a larger threshold current.

The first paper detailing the application of QC lasers to spectroscopy was published in 1998 [16]. In the same year a QC laser was demonstrated using

a GaAs / Al 0.33Ga 0.67As on GaAs material system [17], this was the first time a QC laser had been fabricated from materials other than InGaAs / AlInAs on InP. The major advantage of this material system is that as a compound semiconductor fabrication technology it is the most developed, however GaAs based QC lasers do not generally perform as well as their InP equivalents.

1.4 Quantum Cascade Laser Spectroscopy

The characteristics of QC (Quantum Cascade) lasers are covered in section 1.3, the purpose of this section is to compare their different methods of operation when they are applied to spectroscopy. There are two basic modes of operating a QC laser to obtain an absorption spectrum, they can be driven in either pulsed [16] or continuous wave (cw) [18] mode. The availability of room-temperature cw QC lasers has limited the development of cw QC laser spectroscopy, however the availability of these devices has been increasing. As such, development into spectroscopic methods that exploit QC lasers has been increasing. The different methods of QC laser spectroscopy are shown in figure 1.6.

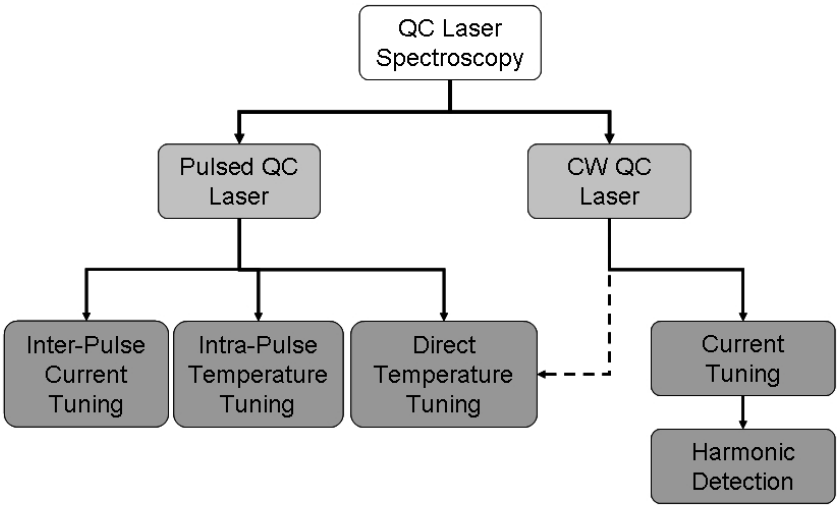

Figure 1.6: The different methods of QC laser spectroscopy are linked through the way the QC laser is driven. Both pulsed and cw methods of operation can be used to measure an absorption spectrum in different ways.

The pulsed method of driving a QC laser is the basis for much of the research described in this thesis. The pulsed method works by tuning the laser through a spectroscopic window. There are three methods of achieving this tuning, intra-pulse [19], inter-pulse [20] and by directly altering the temperature of the device.

The inter-pulse method uses pulse lengths of 10 to 50 ns, however an additional sub-threshold current ramp is applied between consecutive pulses. The difference in the applied current between pulses results in a slight change in the emitted wavelength of the device. A single measurement is made with each pulse and when several pulses are recorded a transmission profile can be built that will trace out an absorption line.

The intra-pulse method uses longer pulse lengths of 250 ns to 2 μs. The current pulse that is applied causes the temperature of the laser to increase. As the DFB grating expands as a result of the temperature change the wavelength of the device also changes. Several hundred measurements are

recorded during one single pulse which scans through a wavelength window.

The direct temperature tuning method could be applied to either pulsed or cw QC lasers, it is similar to the intra-pulse method in that the temperature of the laser is changed dynamically to create a spectral window. The temperature of the device would be controlled by a Peltier cooler. The process of changing the wavelength of the device through directly modulating the temperature is slow in comparison to the current ramp used in the inter-pulse method or with the intrinsic heating provided by the intra-pulse method.

When a cw QC laser is operated in a current modulation mode it is possible by means of a lock-in amplifier to monitor the second harmonic of the absorption signal. This presents the advantage of a reduction in the noise that is observed allowing a higher detection sensitivity [21].

The following chapters detail the optical development that has taken place, the analysis methodology and the algorithms that were developed to analyse the data presented in this thesis. The application of these developments are also highlighted in the type approval experiments intended to verify the performance of a sensor based on this development. The data resulting from industrial trials and the development that these trials prompted is also presented. Finally, the application of the developed techniques is applied to the measurement of gases and temperature within a low-pressure flame reactor during combustion of simple fuels. The final chapter explains the future direction that the work will follow.

References

[1] D.M. Etheridge, L.P. Steele, R.L. Langenfelds, R.J. Francey, J.M. Barnola and V.I. Morgan *"Historical CO_2 records from the Law Dome DE08, DE08-2, and DSS ice cores"*, Trends: A Compendium of Data on Global Change. Carbon Dioxide Information Analysis Center, Oak Ridge National Laboratory, U.S. Department of Energy, Oak Ridge, Tenn., U.S.A. (1998)

[2] Pieter Tans, NOAA/ESRL (www.esrl.noaa.gov/gmd/ccgg/trends)

[3] V Guissani, *"The UK Clean Air Act 1956: An Empirical Investigation"*, Centre for Social and Economic Research on the Global Environment, University College London and University of East Anglia (1994)

[4] M. Tacke, *"New developments and application of tunable IR lead salt lasers"*, Infra. Phys. Techn. **36**, 447-463. (1995)

[5] G. Duxbury, *Infrared Vibration-Rotation Spectroscopy: From Free Radicals to the Infrared Sky*, Wiley (1999)

[6] Dwayne Heard (Editor), *Analytical Techniques for Atmospheric Measurement*, Wiley (2006)

[7] P. Atkins, R. Friedman, *Molecular Quantum Mechanics*, Oxford (2005)

[8] R.F. Kazarinov, R.A. Suris, Sov. Phys. Semicond. 5, **207** (1971)

[9] J. Faist, F. Capasso, C. Sirtori, A.L. Hutchison, A.Y. Cho, *"Quantum Cascade Laser"*, Science, **264** (1994)

[10] J. Faist, F. Capasso, C. Sirtori, D.L. Sivco, A.L. Hutchinson, and A.Y. Cho, *"Vertical transition quantum cascade laser with bragg confined excited state"*, Appl. Phys. Lett., **66**, 538-540 (1994)

[11] J. Faist, F. Capasso, C. Sirtori, A.L. Hutchinson, and A.Y. Cho, *"Continuous wave operation of a vertical transition quantum cascade laser above T=80K"*, Appl. Phys. Lett. **67**, 3057-3059 (1994)

[12] J. Faist, F. Capasso, C. Sirtori, D.L. Sivco, J.N. Baillargeon, A.L. Hutchinson, Sung-Nee G. Chu and A.Y. Cho, *"High Power mid-infrared ($\lambda \sim 5\ \mu m$) quantum cascade lasers operating above room temperature"*, Appl. Phys. Lett. **68**, 3680-3682 (1996)

[13] J. Faist, C. Gmachl, F. Capasso, C. Sirtori, J.N. Baillargeon, and A.Y. Cho, *"Distributed feedback quantum cascade lasers"*, Appl. Phys. Lett **70**, 2670-2672 (1997)

[14] G. Scamarcio, F. Capasso, C. Sirtori, J. Faist, A.L. Hutchinson, D.L. Sivco, A.Y. Cho, *"High-power infrared (8-micrometer wavelength) superlattice lasers"*, Science **276**, 773-776 (1997)

[15] G. Scamarcio, C. Gmachl, F. Capasso, A. Tredicucci, A.L. Hutchinson, D.L. Sivco, andA.Y. Cho, *"Long-wavelength (lambda congruent to 11 μ m) interminiband Fabry-Perot and distributed feedback quantum cascade lasers"*, Semicond. Sci. Tech. **13** 1333-1339 (1998)

[16] K. Namjou, S. Cai, E.A. Whittaker, J. Faist, C. Gmachl, F. Capasso, D.L. Sivco, A.Y. Cho, *"Sensitive absorption spectroscopy with a room-temperature distributed-feedback quantum-cascade laser"*, Opt. Lett. **23** (3), 219-221, (1998)

[17] C. Sirtori, P. Kruck, S. Barbieri, P. Collot, J. Nagle, M. Beck, J. Faist, U. Oesterle, *"GaAs/AlxGa1-x as quantum cascade lasers"*, Appl. Phys. Lett. **73** (24), 3486-3488, (1998)

[18] AA Kosterev, AL Malinovsky, FK Tittel, C Gmachl, F Capasso, DL Sivco, JN Baillargeon, AL Hutchinson, AY Cho, *"Cavity ringdown*

spectroscopic detection of nitric oxide with a continuous-wave quantum-cascade laser", Appl. Opt. **40**, 30, 5522-5529 (2001)

[19] M.T. McCulloch, E.L. Normand, N. Langford, and G. Duxbury *"Highly sensitive detection of trace gases using the time-resolved frequency downchirp from pulsed quantum-cascade lasers"*, JOSA B **20** (8), 1761-1768 (2003)

[20] J Manne, W Jager, J Tulip, *"Sensitive detection of ammonia and ethylene with a pulsed quantum cascade laser using intra and interpulse spectroscopic techniques"*, Appl. Phys. B **94**, 2, 337-344 (2009)

[21] D Weidmann, FK Tittel, T Aellen, M Beck, D Hofstetter, J Faist, S Blaser *"Mid-infrared trace-gas sensing with a quasi-continuous-wave Peltier-cooled distributed feedback quantum cascade laser"*, Appl. Phys. B, **79**, 7, 907-913, (2004)

Chapter 2

Sensor Operation and Optical Design

2.1 Overview

The core topic of this thesis is the detection and monitoring of gases through the application of QC lasers emitting in the mid infrared. A significant amount of time was spent developing and testing the various components of an intra-pulse QC laser based gas sensor. In broad terms the sensor must consist of the elements shown in figure 2.1. These include the laser and drive electronics, the optical components that allow the light to interact with the medium under study, the detection and digitisation system and the analysis of the recorded data. The general method of operation and the more complex aspects of the optical system are covered in this chapter. The detection system and analysis are the subject of the following chapter.

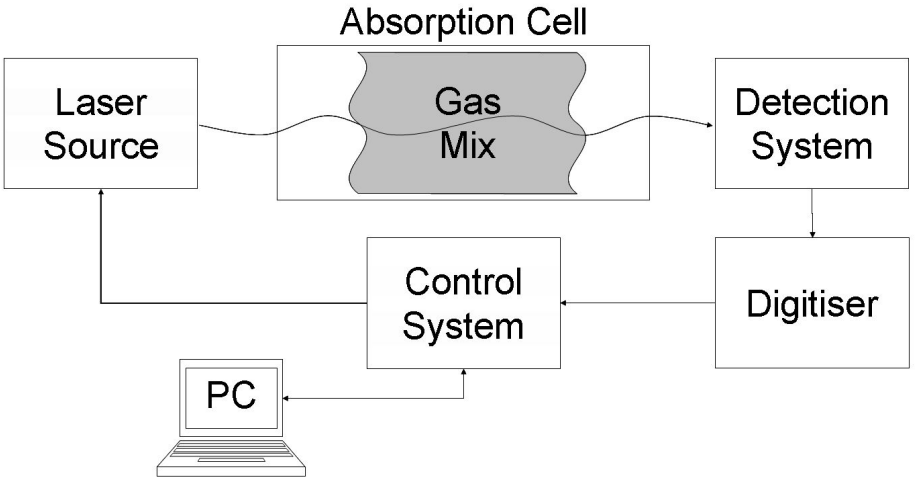

Figure 2.1: This shows the basic elements of an absorption based intra-pulse QC laser gas sensor. The QC laser source is directed through a gas mix and then detected and digitised in preparation for analysis by algorithms contained on the control pc.

2.2 QC Lasers and Operation

The intra-pulsed method of operating QC lasers is the basis for much of the research described in this thesis, other methods are described earlier in section 1.4. It is possible to produce high resolution ($<0.01\ cm^{-1}$) linear absorption spectra at rapid ($>40\ Hz$) speed by using the intra-pulse method [1]. The temperature tuning method is slower and the inter-pulse method requires sophisticated pulse normalisation electronics. The wavelength tuning behaviour of QC lasers can lead to distorted spectra when the time taken to sweep across an absorption line is less than the time between molecular collisions [2]. Whether any distortion occurs is dependent upon the time between molecular collisions and hence the pressure of the medium and the tuning rate of the laser.

2.2.1 QC Laser Operation

A requirement of the intra-pulse method is the need for high-speed electronics that are able to resolve and record the laser pulses that are generated. The intra-pulse method creates a spectral profile within a single laser pulse. The laser is driven with current pulses of 250 ns to 2 μs. These current pulses are applied at repetition rates up to hundreds of kHz. The current applied to the laser is typically in the region of 0.5-3A and the voltages required to form an electric field that creates the cascade structure are in the region of 6-18V. A current driver capable of meeting this specification must be used to create the current pulses that are applied to the laser. The resultant tuning of the laser creates spectral windows of 1-4 cm^{-1}.

The measurement sensitivity of a sensor is directly related to the quality of the current pulses created by the drive electronics. The signal to noise ratio of the pulse that is applied to the QC laser is one of the factors that determines the signal to noise ratio of the light pulse. The minimum absorption that can be detected is dependent upon this. Another important factor is the repeatability of the pulses, any significant amplitude fluctuations will make the digitised signal difficult to analyse. Since the pulses are averaged, any jitter between consecutive pulses will cause an effect similar to a low pass filter and will therefore reduce the bandwidth of the system. An example of a QC laser pulse created by suitable electronics is shown in figure 2.2.

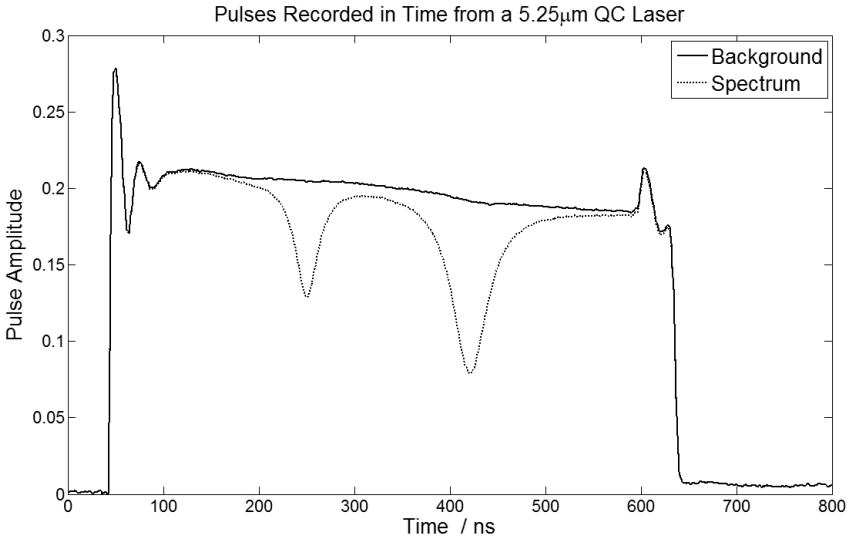

Figure 2.2: A $5.25\mu m$ QC laser pulse, recorded in time. The laser is driven with 600ns current pulses, the background pulse shows the laser free from absorption lines and the spectrum pulse shows the result of the light passing through 100cm of NO at a concentration of 500ppmv. The two distinct NO absorptions are produced from contributions from a number of individual absorption lines.

Within a single laser pulse the temperature of the laser increases, as this happens the refractive index of the waveguide changes and the distributed feedback (DFB) grating expands, this changes the wavelength of light that is supported by the waveguide. The instantaneous wavenumber position of the laser tunes downward during the current pulse, this creates a spectral window in time. The temperature change in the laser can be up to $50°K$ during a single pulse creating spectral windows of $1 - 4cm^{-1}$, depending on the QC laser. A thermoelectric cooler (TEC) or Peltier is used to control the base temperature of the laser. It also prevents damage and allows each new laser pulse to begin at the same temperature and hence the same wavelength. This means that the absolute spectral window is the same for all subsequent pulses. Changing the TEC set point also allows the starting wavenumber of the pulse to controlled, therefore the window can be shifted by approximately $1cm^{-1}$ for every $10°C$ and a specific set of absorptions can be viewed. An example of the tuning caused by this temperature change is shown in figure

2.3.

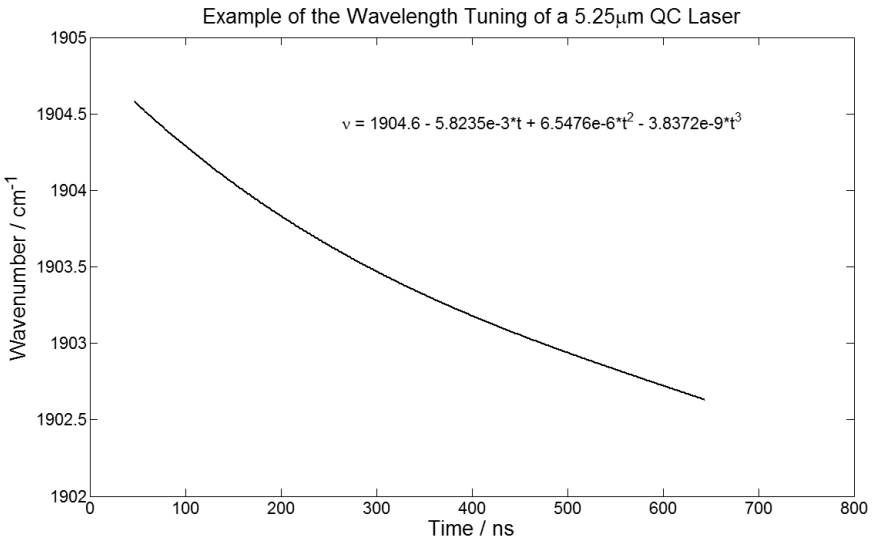

Figure 2.3: This plot shows the relationship between the time of a pulse and the wavenumber position. This is the tuning of the $5.25\mu m$ QC laser pulses shown in figure 2.2. A polynomial is used to characterise the tuning, over narrow ranges towards the end of the pulse it is almost linear, however using a polynomial leads to more accurate results.

Once the tuning has been characterised it is possible to display the pulses in a wavenumber scale rather than time, this is shown in figure 2.4. The region of the pulse that is used to detect the presence of gases and to calculate their concentrations is marked on the plot.

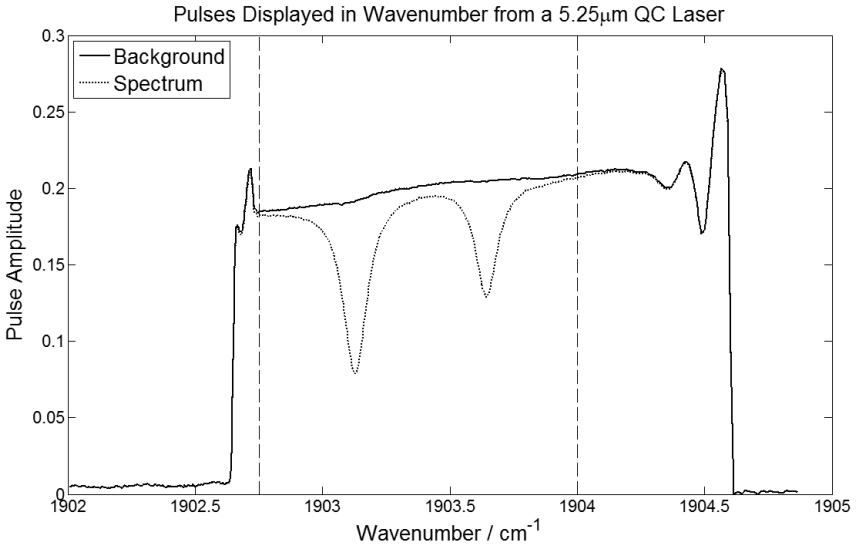

Figure 2.4: The $5.25\mu m$ QC laser pulse is now shown in wavenumber. The dashed vertical lines enclose the region of the pulse that is used to perform concentration measurements. This region excludes any feature caused by the switch on or off characteristic.

To properly analyse the spectra that are produced by the laser the absorptions must be normalised to the amplitude of the input light before the absorptions take place, this means that the spectra that are recorded are not dependent on laser power. Also, the regions of the pulse that are not of spectroscopic interest are typically discarded. This creates a transmission spectrum, which can be calculated by using equation 2.1.

$$Transmission = \frac{Spectra}{Background} \tag{2.1}$$

The section of the pulse that is used is usually in an area where there is no pulse switch on or off characteristics, this ensures that the spectra are as noise free as possible. It is also preferential to extract the data from the region of the pulse where the tuning is at its slowest and most linear, this maximises the spectral resolution of the measurements. An example of a transmission spectrum is shown in figure 2.5, this was calculated from the pulses shown above.

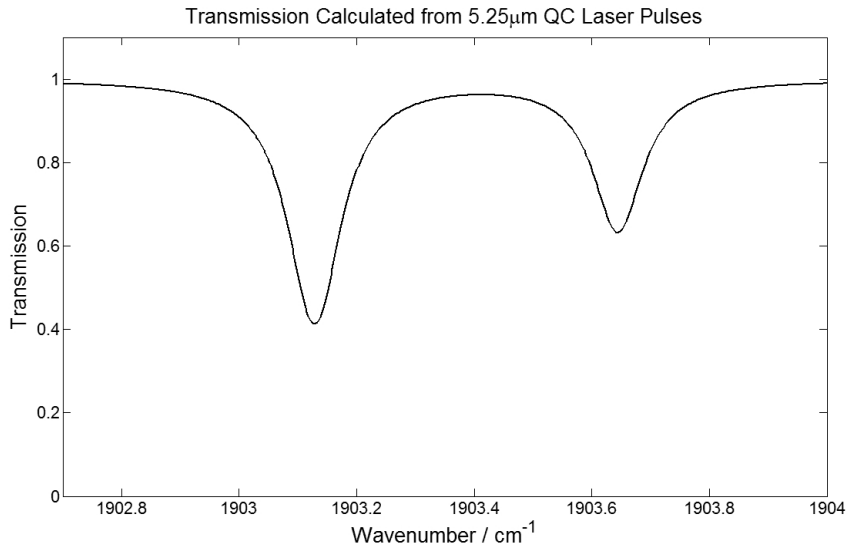

Figure 2.5: The $5.25\mu m$ QC laser pulse is now used to calculate an NO transmission spectra using equation 2.1. The plot only shows the region of the pulse that is used for spectroscopic measurements.

It is possible to generate transmission spectra using computer models and absorption line data. The recorded transmission spectra, such as the one in figure 2.5, can be compared to generated spectra in an effort to determine the composition and concentration ratios of a gas mix.

2.2.2 QC Laser Output

The output from a DFB QC laser is a linearly polarised beam with a typical divergence of 60° in the vertical axis and 40° in the horizontal axis. This large divergence means that it is necessary to use either reflective or transmissive collimation optics to allow the beam to be directed through a gas medium. The QC lasers used to record the data in this thesis were collimated with zinc selenide (ZnSe) lenses. The reflectivity of uncoated ZnSe is approximately 30%, therefore to the lenses must be anti-reflection (AR) coated to transmit as much of the laser beam as possible and avoid back-reflections which may damage the laser.

A typical beam profile produced by AR coated ZnSe collimation lenses, at a distance of 1m from a QC laser, is shown below in figure 2.6.

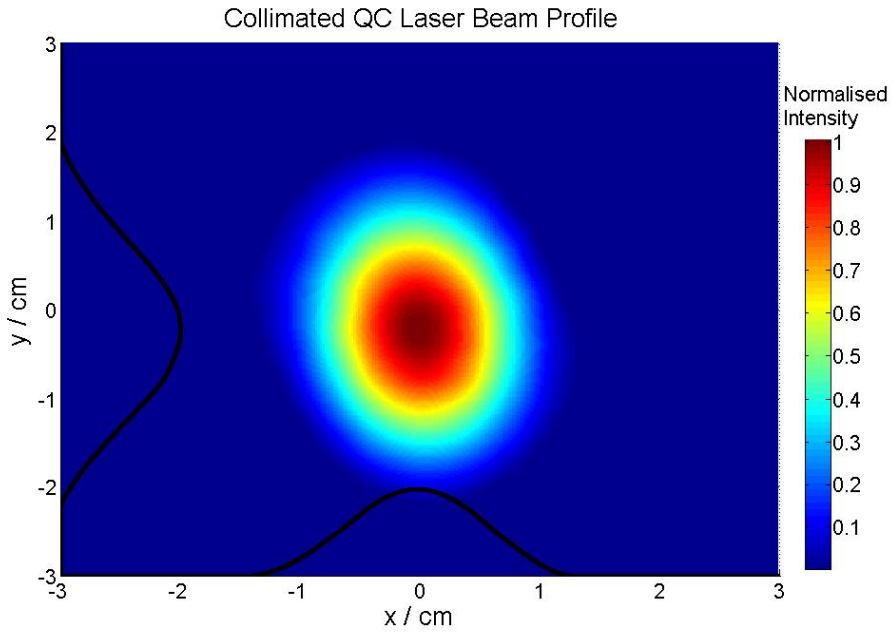

Figure 2.6: This shows a QC laser beam profile at a distance of 1m from the laser. The beam has been collimmated with AR coated ZnSe lenses.

A collimated or near-collimated beam is necessary to allow the laser output to be easily directed through an absorbing medium. This is particularly important when using multi-pass gas absorption cells which are often a component of gas sensing instrumentation.

2.3 Extractive and *In-Situ* Methods

One of the components shown in figure 2.1 is an absorption cell where the mid-infrared beam from the laser is passed through a gas mix to obtain a measurement. This absorption cell can take many forms and in some cases can simply be an open path between the laser source and the detector. The absorption cell defines the place where the QC laser light interacts with the gases being measured.

The medium that a gas sensor is monitoring is often the exhaust emission from an engine or part of a process in an industrial environment. There are cases in which the physical environment of the gas medium is not ideal for the sensitive measurement of low concentration values. As an example consider atmospheric CH_4 which has a typical concentration of 1.8 ppmv. To accurately measure this concentration at atmospheric pressure and temperature it would be necessary to have an open pathlength of 10's to 100's of metres. In an open path sensor this would be difficult to implement, the sensor would not be compact and a stable optical setup would be very difficult to maintain. The sensor would also be unable to sample the concentration at a single spatial point.

In other circumstances it is not possible to perform a direct measurement on the gas because of pressure, temperature or some other condition of the gas such as the presence of particulate matter. For example, in a multi-component gas mix it is often necessary to work at a reduced pressure in order to resolve absorption line contributions from different gases. The temperature of the gas mix can influence the absorption line strengths, if a particular range of measurement is required the ability to control the gas temperature can be necessary.

There are two general categories that the absorption cell can be described as, they are extractive or *in-situ*. In an extractive sensor the gas mix is taken from its source and brought to the sensor where analysis takes place. An *in-situ* sensor is coupled into the original enclosure containing the gas and the sensor performs its measurements directly on the gas in its normal environment.

2.3.1 Extractive Sensors

In an extractive based sensor, the medium being monitored is removed from its source and brought to the sensor for analysis. The gas mix may be continuously sampled by means of a pump and flow system or stored for

later analysis. The accuracy of this method is dependent on the condition and content of the extracted sample being consistent with its source. There can be a change in the composition and concentration of the gases through molecular processes such as chemical reaction or condensation. Many gases such as NH_3, H_2O or HNO_3 are adsorbent and will stick to the sides of sample lines or the gas cell, accurate measurement of gases like these can prove difficult when using an extractive sensor.

When the measurements are being recorded continuously or in a real time fashion the extractive sensor must include some kind of flow system to continually transfer gas from its source to the absorption cell and then exhaust the used sample. This adds the requirement of equipment such as filters, pumps and sample lines. However, it also allows the physical condition of the gas to be altered (i.e. the pressure or temperature of the gas can be changed to values more suitable to high sensitivity detection). Lowering the pressure can substantially reduce the width of the absorption lines being studied, this increases the selectivity of the sensor by reducing the interference effect that is caused by the presence of other gases. The strength of certain absorption lines can be enhanced by changing the temperature of the gas mix, thereby increasing the sensitivity of a sensor.

In certain situations measurements cannot taken continuously, this is often due to weight or space restrictions, for example with high altitude atmospheric sensors or in extremely hostile environments. This means that rather than including a flow system and integrating the sensor, a sample of the gas can be stored and then supplied to the sensor when it can be analysed at a more convenient time and place.

One of the greatest advantages to extractive sensors is the ability to control the pathlength through which the measurements are recorded. In an extractive sensor the sensitivity can be increased by extending the optical pathlength through the gas by using a multi-pass mirror arrangement. Equation 2.2, the Beer-Lambert law, describes how the light that is sent into a gas mix is absorbed thereby reducing the intensity of light that exits the

gas mix.

$$I = I_0 e^{-\alpha l c} \tag{2.2}$$

The I_0 and I terms denote the intensity of light before and after the gas mix, respectively. The l term is the optical pathlength through the gas medium, this parameter can be controlled to set a sensor to measure a specific concentration range. Increasing the pathlength has a direct effect on the sensitivity of a sensor, the use of multi-pass gas cells is discussed in further detail in section 2.4. The c term is the concentration of the gas and the α term is the absorption co-efficient.

The absorption co-efficient is composed of a lineshape function which is area normalised and a line strength. The line strength is expressed in units of $cm^{-1}/molecule\,cm^{-2}$. The parameters and units mentioned here are explored further in section 3.4.

2.3.2 *In-Situ* Sensors

There are a number of ways of configuring a laser based sensor to perform this kind of detection. From an optical perspective the major question is the positioning of the laser source and detection systems. As an example, consider an exhaust stack, an *in-situ* laser based sensor must send light into the stack and measure the resulting signal through some detection system. The most obvious solution is a cross stack system in which light is coupled into the stack and detected on the opposite side. When a cross-stack arrangement cannot be achieved, a mirror can be used to send light back towards the entrance to the stack allowing for a more compact sensor. An example of three *in-situ* sensors is shown in figure 2.7. In each of the arrangements shown their is limited scope for controlling the pathlength.

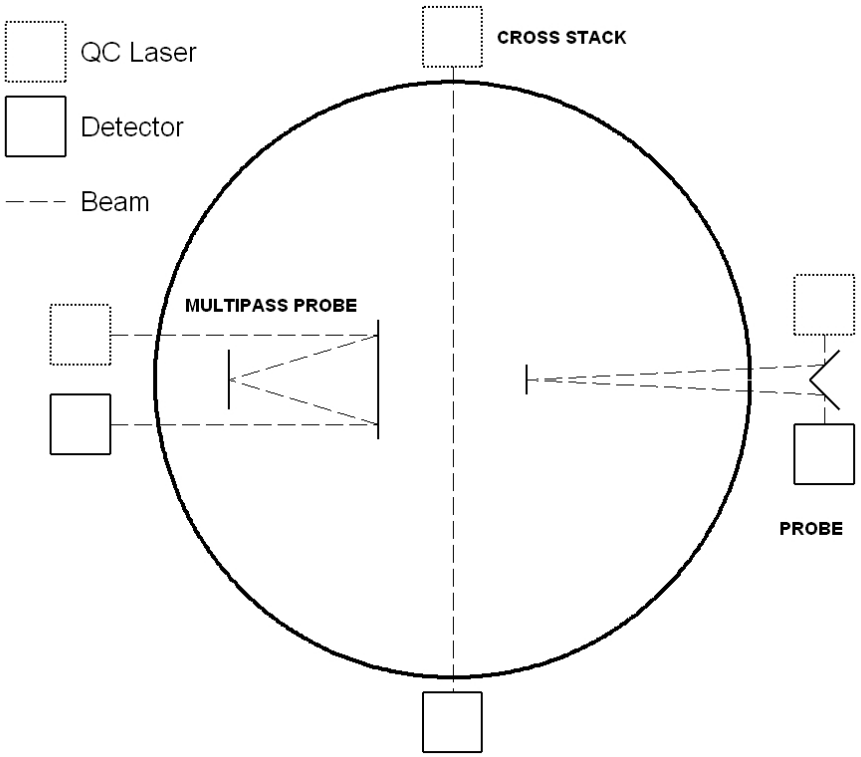

Figure 2.7: This shows three *in-situ* sensor arrangements for performing stack measurements. The most basic is the cross stack arrangement and the most complex is the multi-pass probe arrangement. In any of the cases, the pressure and temperature are set by the conditions within the stack and the options for pathlength extension or even selection are limited. However, measurement response time is fast and there is no need for additional flow system equipment.

It is possible in certain cases to use a multi-pass cell to increase the pathlength and hence the sensitivity of an *in-situ* sensor, however due to the often hostile conditions the maximum pathlength that can be obtained is much less than that available when using an extractive sensor. The pathlength of these systems is often limited by the diameter of the exhaust stack. In an industrial environment a gas mix can be at an elevated temperature or pressure, this can make it very difficult to position a sealed window fitting that is capable of transmitting light into the gas. It is also difficult to maintain optical components inside the stack when they are susceptible to tar or other forms of chemical deposit.

The physical conditions can make it difficult to distinguish between the absorption lines of different gases as well as limiting the sensitivity and precision of the measurements. Since neither the pressure nor temperature can be controlled, they must be measured or otherwise known to allow accurate comparison of the recorded data with spectroscopic models. Pressure and temperature sensors must be used to probe the conditions of the gas medium. The output from these sensors must then be read by analogue to digital converters (ADCs), which allow the measurements to be used in concentration retrieval algorithms. There are a few examples of *in-situ* sensors discussed in chapter 4, however where possible the use of extractive sensors is preferable.

2.4 Multi-Pass Gas Cells

A major element of laser spectroscopy is the Beer-Lambert law, equation 2.3 assumes a linear relationship between the input beam power and the absorption of the species being studied.

$$I = I_0 e^{-\alpha l c} \tag{2.3}$$

Where l is the optical path length through the medium, c is the concentration and α is the absorption coefficient. It states that the absorption of light within a medium is related to the optical pathlength through the medium. Therefore increasing the pathlength through a medium increases the absorption of light and hence the sensitivity of an absorption based gas sensor. Multi-pass gas cells are used to fold an optical path within a contained volume. This allows a sensor to have absorption pathlengths of up to several hundred meters through a low volume while remaining compact.

A major requirement of a highly sensitive and robust sensor is an absorption pathlength that is long enough to produce measurable absorptions while remaining optically stable and compact. There have been many multi-pass

mirror systems used to extend optical pathlengths, such as the White cell [3] and the Herriott cell, first devised by Herriott et al [4, 5]. A number of varieties of these cells were used for product development and research. The development of optical multi-pass cells was concentrated upon the Herriott cell and its astigmatic variant. This was due to the small volumes, fixed pathlength requirements and mechanical simplicity afforded by the two main types of Herriott cell.

2.4.1 Herriott Cell

The Herriott Cell [4, 5] was originally designed as an optical delay line. The original design consists of two opposing circular, concave mirrors, one of which has an off-axis coupling hole to allow light to enter and exit the cell. This is shown in figure 2.8.

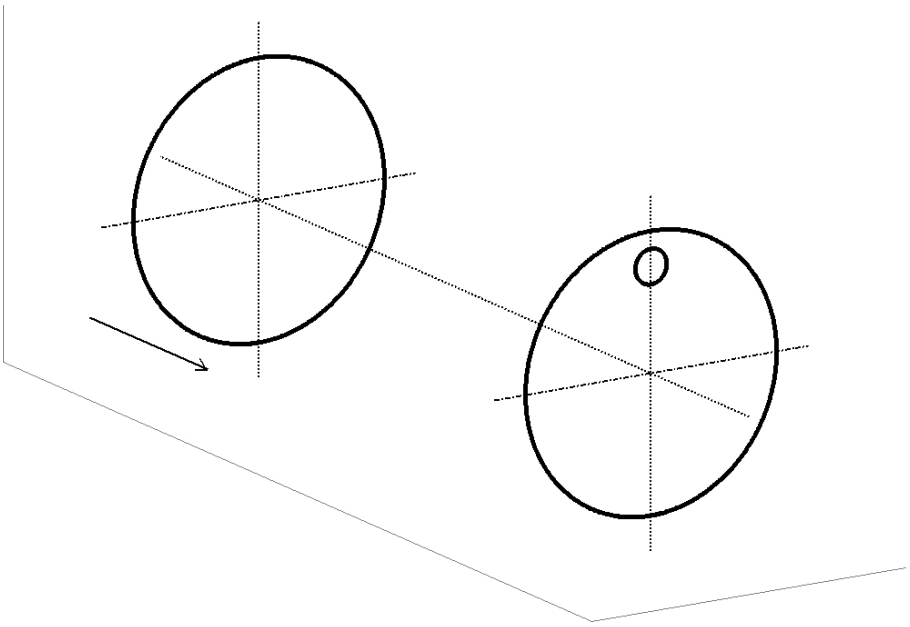

Figure 2.8: This shows the typical mirror placement in a Herriott cell. The circular, concave mirrors are placed facing each other. The coupling hole where light enters and exits the cell is shown on the front mirror. Adjustment of the supported pathlength is obtained through varying the separation of the two mirrors.

A beam of light coupled into the cell will trace an elliptical pattern on the surface of the mirrors as it passes between them. Assuming that the cell is stable, the beam will eventually be directed back through the coupling hole and exit the cell. An example of the spot pattern generated from a Herriott cell is shown in figure 2.9. The section following the figure describes the matrix models used to model the behaviour of a standard Herriott cell.

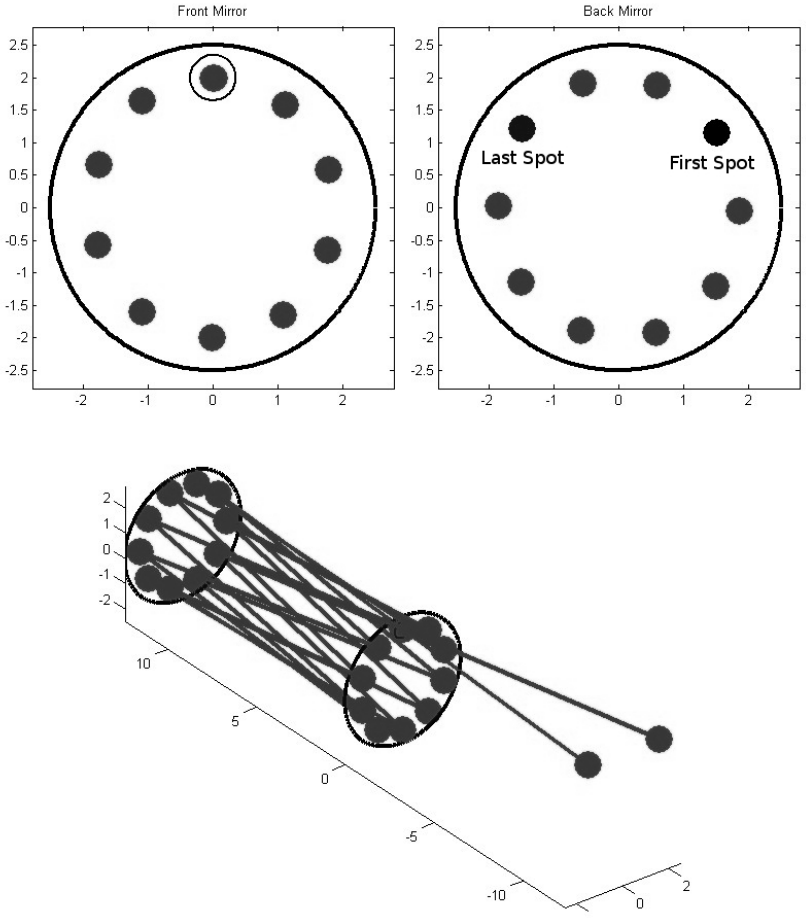

Figure 2.9: An example of a Herriott cell spot pattern and cell beam path. The beam traces an elliptical pattern on the surface of the mirrors and the beam eventually reaches the coupling hole where it leaves the cell. The first and last spots are indicated on the back mirror, the first spot has been positioned to produce a circular pattern.

The measurements and sensors presented in this thesis often required modifications to be made to the original design of a Herriott cell. This

was necessary to tailor the Herriott cell to a particular application, two of these designs are detailed in the following sections. A mathematical model of the Herriott cell is described below, this is followed by some examples of modifications that were made to the basic Herriott cell.

Matrix Model

Ray transfer matrix analysis [6, 7] can be used to mathematically model a Herriott cell, this technique uses matrices to describe an optical system which can be made up of various optical components, it assumes a paraxial approximation. When these matrices are multiplied by a vector which represents the beam of light before entering the optical system a result is obtained in the form of a vector which represents the beam of light after the optical component. Equations 2.4, 2.6 & 2.7 shown a set of simple matrices that represent a beam of light, a simple spherical mirror and a distance in space.

Equation 2.4 is the vector that describes a beam of light by its position, x_0 and y_0 and its direction of propagation, x'_0 and y'_0, which represent the gradient of the beam.

$$\mathbf{Z}_0 = \begin{bmatrix} x_0 \\ x'_0 \\ 1 \\ y_0 \\ y'_0 \\ 1 \end{bmatrix} \tag{2.4}$$

A mirror matrix is formed from the equations in 2.5, where r is the radius of curvature of the mirror and $-2/r$ is the resultant focal length. The two components represent the radius in both the x and y planes, since the mirror is rotationally symmetrical they are equivalent. The Δ terms relate to a displacement of the mirror along the corresponding axis and the δ terms relate to a tilt of the mirror in the corresponding axis.

$$\begin{aligned} x_1 &= x_0 \\ x_1' &= -\tfrac{2}{r}(x_0 + \Delta_x) + x_0' + \delta_x \\ y_1 &= y_0 \\ y_1' &= -\tfrac{2}{r}(y_0 + \Delta_y) + y_0' + \delta_y \end{aligned} \tag{2.5}$$

These equations are used to form the matrix in 2.6 which shows a ray transfer matrix of a spherical mirror. The Δ terms are incorporated by adjusting the position of the ray vector before it is multiplied by the mirror matrix and then returning the vector to its original position afterwords. In effect, this simply moves the position of the mirror in the x and y planes.

$$\mathbf{R} = \begin{bmatrix} 1 & 0 & 0 & 0 & 0 & 0 \\ -2/r & 1 & \delta_x & 0 & 0 & 0 \\ 0 & 0 & 1 & 0 & 0 & 0 \\ 0 & 0 & 0 & 1 & 0 & 0 \\ 0 & 0 & 0 & -2/r & 1 & \delta_y \\ 0 & 0 & 0 & 0 & 0 & 1 \end{bmatrix} \tag{2.6}$$

Equation 2.7 is a ray transfer matrix of a distance travelled, d, in the z-axis.

$$\mathbf{D} = \begin{bmatrix} 1 & d & 0 & 0 & 0 & 0 \\ 0 & 1 & 0 & 0 & 0 & 0 \\ 0 & 0 & 1 & 0 & 0 & 0 \\ 0 & 0 & 0 & 1 & d & 0 \\ 0 & 0 & 0 & 0 & 1 & 0 \\ 0 & 0 & 0 & 0 & 0 & 1 \end{bmatrix} \tag{2.7}$$

The distance matrix is formed from the equations in 2.8.

$$\begin{aligned} x_1 &= x_0 + dx'_0 \\ x'_1 &= x'_0 \\ y_1 &= y_0 + dx'_0 \\ y'_1 &= y'_0 \end{aligned} \tag{2.8}$$

For the case of a Herriott cell, in a single traverse of the cell the ray transfer matrix equation is given by 2.9. This allows the ray vector to be calculated after the optical components defined by **M**. The matrix **M** is formed in equation 2.10.

$$\mathbf{Z}_1 = \mathbf{M}\mathbf{Z}_0 \tag{2.9}$$

$$\mathbf{M} = \mathbf{R}\mathbf{D} \tag{2.10}$$

Therefore for n passes of the cell the resulting ray vector is given by equation 2.11.

$$\mathbf{Z}_n = \mathbf{M}^n\mathbf{Z}_0 \tag{2.11}$$

The beam will continue to propagate from mirror to mirror until it either walks off one of the mirrors in the case of an unstable cell or reaches the position of the coupling hole on the front mirror and exits the cell. Since the most efficient spot pattern of the Herriott cell forms a circle the maximum number of spots that it is possible to fit onto a mirror can be calculated by determining the perimeter of the circle and the number of spots that will fit into this perimeter. Equation 2.12 can be used to calculated the maximum number of passes, where y_0 is the position of the coupling hole from the centre of the mirror and hence the radius of the spot pattern and d_h is the size of the coupling hole.

$$N \leq \frac{4\pi y_0}{d_h} \tag{2.12}$$

In-plane Herriott Cell

The research detailed in section 4.5 was obtained from QC laser data that was recorded of flames in a low pressure reactor at the University of Bielefeld, Bielefeld, Germany. The flame reactor was 70cm wide and contained a 6cm burner upon which the flames were supported and supplied with fuel. This burner and hence the flame could be moved within the reactor, allowing different parts of the flame to be sampled with a laser-based spectrometer with a fixed position. Based on some initial measurements, it was determined that three passes through the flame was optimal, this allowed the smaller absorptions to be observed without saturating the stronger ones. In order to maximise the spatial resolution of the measurements the beam waist within the flame needed to be kept to a minimum, a modified version of a Herriott cell was designed to achieve this. A beam path was required where each pass of the beam crossed the centre of the cell at a shallow angle. This led to a small area around the centre of the cell having several passes within a small volume. A model of this cell is shown in figure 2.10.

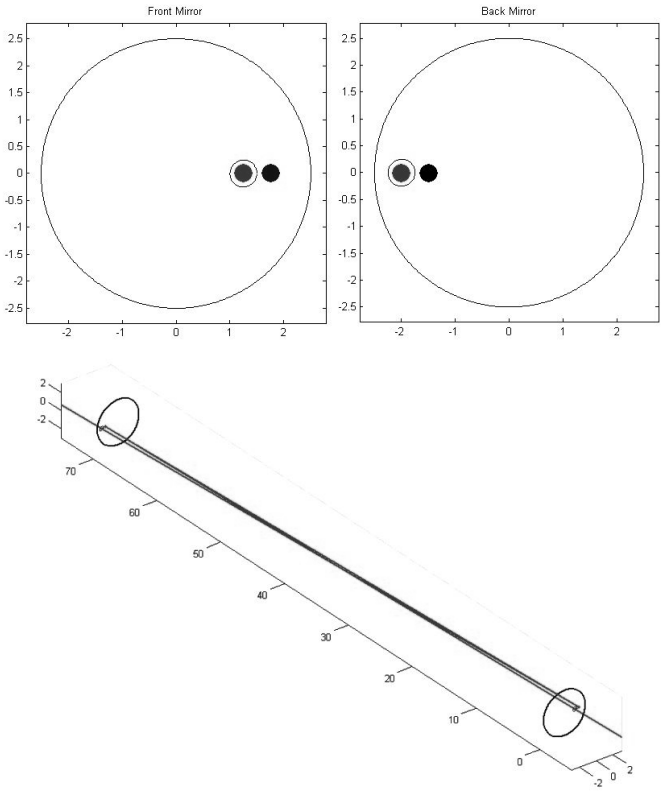

Figure 2.10: The Herriott cell used to perform the Bielefeld flame reactor measurements discussed in section 4.5. Note the addition of a second coupling hole on the far mirror to allow an odd number of passes and the in-plane cell beam path allowing high spatial measurement resolution.

Dual Coupling Hole Herriott Cell

A cell was designed and a prototype built that was intended for use as part of an *in-situ* sensor, the design was based on a standard Herriott cell with two modifications. The first was the addition of a second coupling hole on the front mirror to allow the beam to exit the cell from a different position on the mirror. This modification makes the cell easier to integrate into surrounding optics, largely due to the spatial separation of the input and output beams. A model of this cell is shown in figure 2.11.

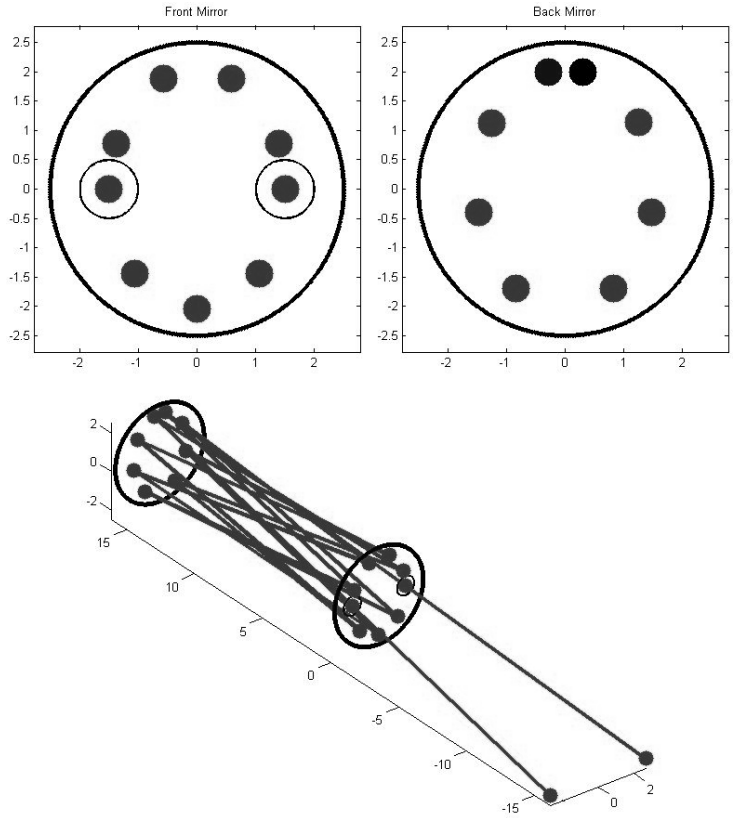

Figure 2.11: This is a Herriott cell with separate input and output coupling holes. This simplifies the optical setup outside the cell by allowing the source and detection systems to be spatially separated.The first and last spots on this design are positioned at the top of the back mirror.

The second, optional modification, was not included in the design shown. This modification was the inclusion of wedged windows on the input and output coupling holes. The wedge angles and orientation of the windows would direct the beam along the required input angle for the cell and then correct the angle at the output. This allows the input and output beams to approach the cell in parallel with each other and the optical axis of the cell and perpendicular to the back of the mirror. This beam parallelism that is enabled by the inclusion of the wedged windows allows the cell to be placed an extended distance from the surrounding optics. This would allow a multi-pass cell to be placed within an exhaust stack. It also allows different cell designs to be introduced with minimum disruption to the surrounding optics

since the input and output beams remain unchanged. While this design was never trialled as part of an *in-situ* sensor, it was included in several other extractive based sensors where the folded path allows for a compact, low-volume sensor.

2.4.2 Astigmatic Herriott Cell

Herriott cells are useful for obtaining pathlengths up to 20 metres, beyond this the mirror size requirements negates their usefulness in compact, portable sensors. To maintain a manageable cell size it becomes necessary to implement cell designs that use the mirror surface area more efficiently, this can be achieved with an astigmatic Herriott cell [7, 8, 9]. The astigmatic Herriott cell is similar to the Herriott cell with two fundamental differences. The first difference is that the individual mirrors have two different, but similar, radii of curvature across orthogonal axes. Secondly, rather than incorporating an off-axis coupling hole the coupling hole is placed at the centre of the mirror. These differences present the advantage of the beam pattern being produced on the surface of the mirrors filling the surface of the entire mirror in a Lissajous pattern. The increased spot density allows a greater number of passes to take place between the mirrors and hence a greater pathlength is obtained from an astigmatic Herriott cell. They can reach pathlengths of up to several hundred meters. The manufacturing tolerances required to create a mirror that could be used to construct an astigmatic Herriott cell are very high. This impacts directly onto the cost of such mirrors. A method of adjustment is also still required to guarantee the functionality of the cell. This adjustment comes from a rotation of one of the mirrors around the axis of the cell, this is shown in 2.12

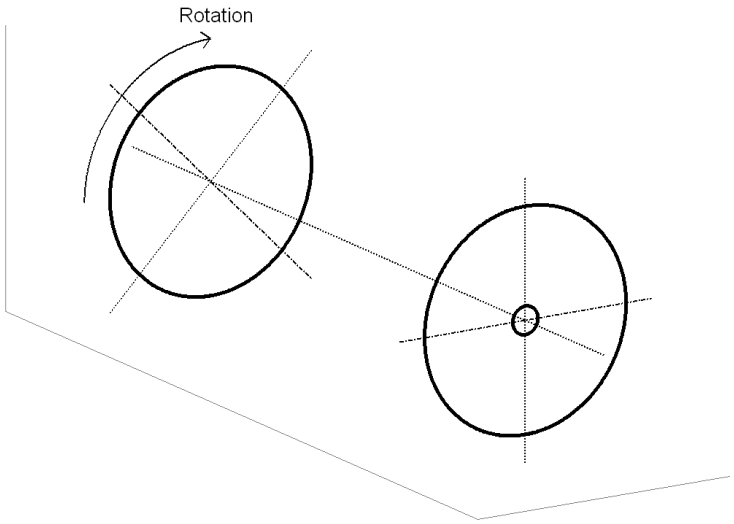

Figure 2.12: This shows the typical mirror placement in an astigmatic Herriott cell. In this cell the coupling hole is positioned at the centre of the front mirror, this together with the astigmatism of the mirrors allows cell patterns to be supported that use the mirror surface more efficiently. The adjustment to this cell is performed by adjusting the separation of the mirrors along the z-axis and by rotating the back mirror about the z-axis as shown.

The combined adjustment of separation and rotation allows manufacturing errors in the radii of curvature to be compensated for. The astigmatism leads to a spot pattern such as the one shown in figure 2.13. On the figure the input and output spots on the back mirror are highlighted. As can be seen their diagonally opposite locations mean that the cell appears as a simple reflective surface in the overall optical system. This has the advantage of simplifying the integration of such a cell into a optical system.

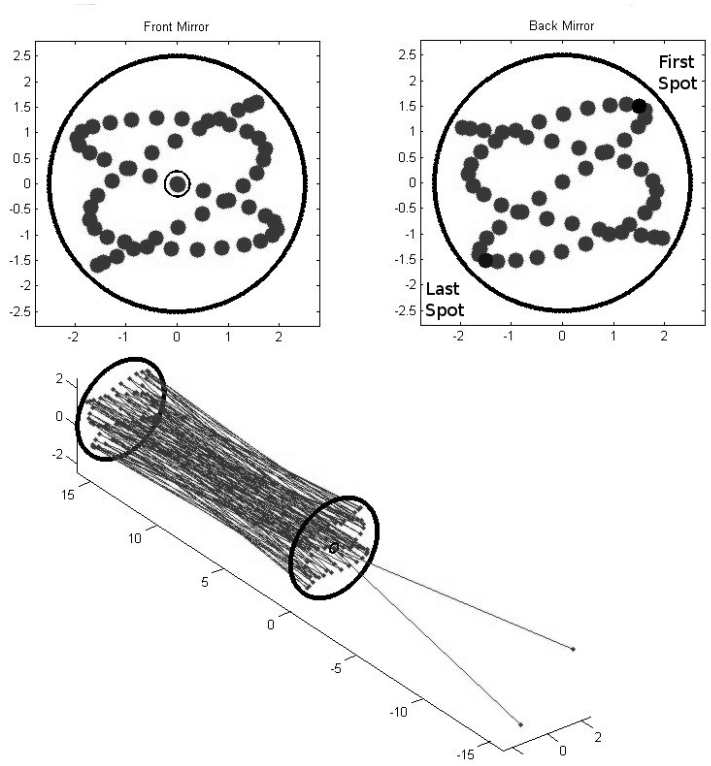

Figure 2.13: This shows an example of a mirror pattern and cell beam path in an astigmatic Herriott cell. The volume of the cell is used more efficiently allowing a greater number of passes between the mirrors to take place. Note the position of the first and last spots on the back mirror, this allows the input and output beams to remain in the same plane by rotating the entire cell through 45^o about the z-axis.

The pathlength limit of these cells is related to the mechanical tolerance as well as the reflectivity of the mirrors, 2.14 shows the expected change in beam intensity with pathlength for a cell of base pathlength $50cm$ and mirror reflectivity 99.2%. This value of reflectivity is possible with a Nickel plated protected coating on an optical grade surface.

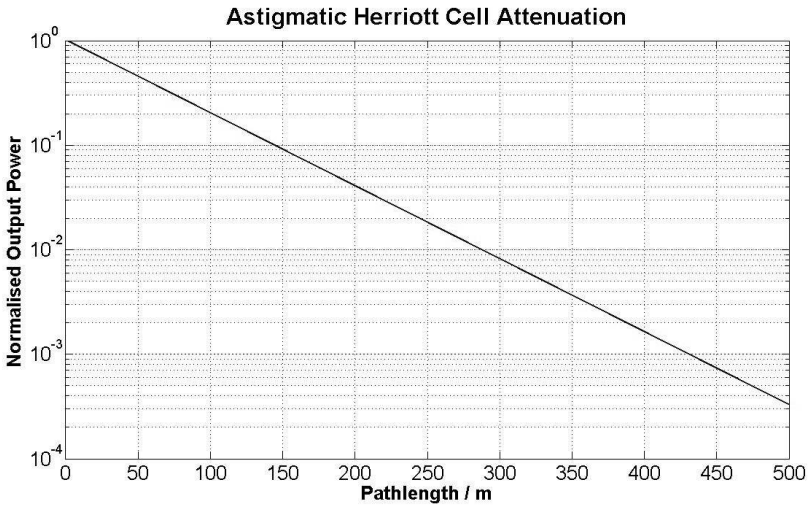

Figure 2.14: The effect of the mirror reflectivity on the power of the beam is shown for an increasing number of passes for a cell with a base pathlength of $50cm$. This attenuation assumes a mirror reflectivity of 99.2%. For a pathlength of over $300m$ using this cell the output power will be less than 1% of the input power.

Matrix Model

The ray transfer matrix model of an astigmatic Herriott cell is very similar to that of the standard Herriott cell. The astigmatism of the mirrors is represented by including separate terms for the two radii of curvature, this is shown in the mirror matrix in 2.13.

$$\mathbf{R}_0 = \begin{bmatrix} 1 & 0 & 0 & 0 \\ -2/r_x & 1 & 0 & 0 \\ 0 & 0 & -2/r_y & 0 \\ 0 & 0 & 0 & 1 \end{bmatrix} \tag{2.13}$$

The rotation of the back mirror is can be computed by equation 2.14, the $\mathbf{T}$ term is the rotation matrix as shown in 2.15, where α is the angle through which the mirror is rotated about the z-axis.

$$\mathbf{R}_{Rotated} = \mathbf{T}^{-1}\mathbf{R}_0\mathbf{T} \tag{2.14}$$

$$\mathbf{T} = \begin{bmatrix} \cos(\alpha) & 0 & \sin(\alpha) & 0 \\ 0 & \cos(\alpha) & 0 & \sin(\alpha) \\ -\sin(\alpha) & 0 & \cos(\alpha) & 0 \\ 0 & -\sin(\alpha) & 0 & \cos(\alpha) \end{bmatrix} \tag{2.15}$$

For a single round trip of the cell the ray transfer matrix equation is shown by equation 2.16. Where $\mathbf{M}$ is given by equation 2.17.

$$\mathbf{Z}_1 = \mathbf{M}\mathbf{Z}_0 \tag{2.16}$$

$$\mathbf{M} = \mathbf{R}_0\mathbf{D}\mathbf{R}_{Rotated}\mathbf{D} \tag{2.17}$$

This shows that the ray travels a distance described by $\mathbf{D}$, is reflected by the back mirror which has been rotated, $\mathbf{R}_{Rotated}$ and then returns along $\mathbf{D}$ before being reflected by the front mirror, $\mathbf{R}_0$. Therefore for n round trips of the cell the resulting beam vector is given by equation 2.18.

$$\mathbf{Z}_n = \mathbf{M}^n\mathbf{Z}_0 \tag{2.18}$$

There is substantial theory governing the design of astigmatic Herriott cells [7], the most important aspects of this theory are described in the following section. Also included are some of the significant cell designs that were produced during the work.

2.4.3 Cell Design

This section gives details of the methods used to design long-path, astigmatic Herriott cells. Some of the multi-pass cell designs that were created during the time of the research are presented as examples.

The matrix model of an astigmatic Herriott cell described in section 2.4.1 is a convenient way of modelling the behaviour of a specific cell. A different approach is required when designing a cell to meet certain pathlength specifications. It is possible to determine the coordinates of beam after n passes using the equations in 2.19 and 2.20.

$$\begin{aligned} x_n &= X_0 \sin(n\theta_x) \\ y_n &= Y_0 \sin(n\theta_y) \end{aligned} \tag{2.19}$$

$$\begin{aligned} \theta_x &= \cos^{-1}\left(1 - \tfrac{d}{R_x}\right) \\ \theta_y &= \cos^{-1}\left(1 - \tfrac{d}{R_y}\right) \end{aligned} \tag{2.20}$$

Where X_0 and Y_0 are the coordinates of the first spot on the back mirror, d is the mirror separation and R_x and R_y are the radii of curvature of the mirrors. In an astigmatic Herriott cell, where the coupling hole is located at the centre of the mirror, the beam will exit the cell when the coordinates fall within the radius of the coupling hole and the pass number, n, is an even number. This occurs when the $n\theta$ terms are equal to an integer multiple of π. This can be expressed as the independent conditions in 2.21.

$$\begin{aligned} n\theta_x &= m_x\pi \\ n\theta_y &= m_y\pi \end{aligned} \tag{2.21}$$

The pass number n must be an even integer (i.e. the spot lies on the front mirror) and there must be no common factors between m_x and m_y. The values of m_x and m_y provide useful information about the Lissajous pattern that is created on the surface of the mirrors. It is advantageous for

the last spot on the back mirror to be diagonally opposite to the first spot, this allows the cell to be easily integrated into an optical system. When the first and last spots are diagonally opposite the beam that leaves the cell is spatially separate from the input and the optical height can remain fixed. These conditions are met when the values for m_x and m_y are even. Cells with even m_x and m_y also exhibit symmetrical patterns which are easier to recognise as well as having a more even distribution of spots. When searching for suitable cell patterns, those with odd values for m_x and m_y are typically discarded.

The equations in 2.19 can be used to map a solution space. This solution space relates values of θ_x and θ_y to the number of passes in a pattern. When a mirror separation is applied to the simultaneous equations in 2.20, they can be solved for the radii of curvature that would be required to support the pattern. An example of a solution space map is shown in figure 2.15. The axes are $\phi = \theta - \frac{\pi}{2}$, this is done merely to centre the map to a (0, 0) coordinate position.

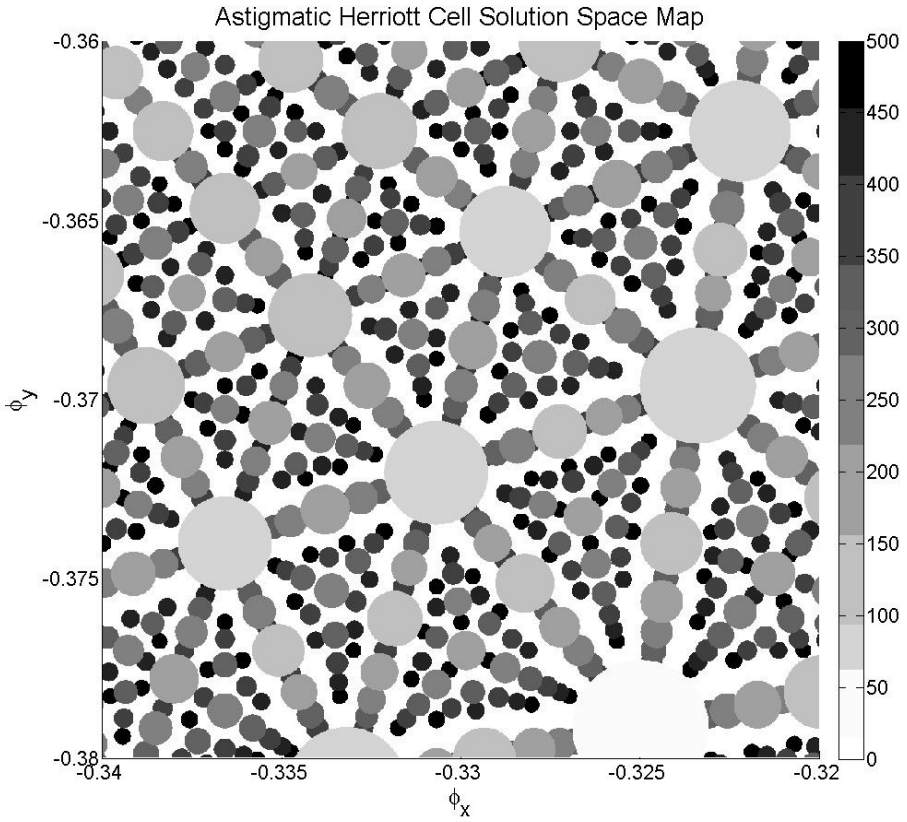

Figure 2.15: This shows a complete solution map for an astigmatic Herriott cell. Each ϕ_x, ϕ_y coordinate defines a cell spot pattern with a pass number indicated by an increasingly darker shade of gray. As the number of passes increases the range over which a pattern is stable decreases. The values of ϕ_x and ϕ_y can be used to calculate mirror radii of curvature for a given mirror separation.

The effect of adjusting the back mirror rotation and the mirror separation is to modify the effective radii of curvature of the mirrors. This allows the cell to be adjusted within a certain range of the solution map. It is convenient when selecting a solution to have a nearby short pathlength solution, this aids the initial cell alignment. A suitable solution is typically an even pattern, when the odd patterns are removed the solution space appears as shown in figure 2.16.

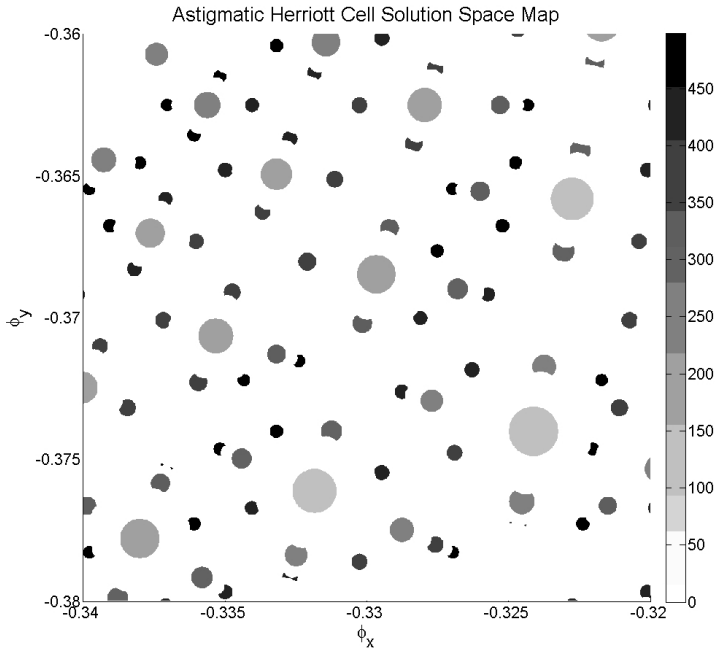

Figure 2.16: This shows a solution map for an astigmatic Herriott cell. Each ϕ_x, ϕ_y coordinate defines a cell spot pattern with a pass number indicated by an increasingly darker shade of gray. This only shows solutions that have even m_x and m_y, since these patterns are most suitable for use in cell designs.

Once a mirror separation has been determined a solution with a pass number that will satisfy a pathlength specification can chosen from the map. The $0°$ radii of curvature can be calculated by solving the simultaneous equations in 2.20. When one of the mirrors is rotated the effective radii of curvature change. The adjustment offered by the rotation of the back mirror becomes negligible as the rotation approaches 0. For this reason the cell is configured so that the radii required for the solution occur at a predetermined rotation of the back mirror, this is typically $10-20°$ to allow enough adjustment while keeping the pattern as close to square as possible. To calculate the effect of rotation on the $0°$ radii of curvature the equation in 2.22 can be used.

$$\mathbf{V} = \mathbf{A}^{-1}\mathbf{B} \tag{2.22}$$

Where **V** is defined in 2.23, **A** in 2.24 and **B** in 2.25.

$$\mathbf{V} = \begin{bmatrix} \frac{1}{R_{x,mirror}} \\ \frac{1}{R_{y,mirror}} \end{bmatrix} \tag{2.23}$$

$$\mathbf{A} = \begin{bmatrix} \cos^2(\tau) & \sin^2(\tau) \\ \sin^2(\tau) & \cos^2(\tau) \end{bmatrix} \tag{2.24}$$

$$\mathbf{B} = \begin{bmatrix} \frac{1}{R_{x,effective}} \\ \frac{1}{R_{y,effective}} \end{bmatrix} \tag{2.25}$$

Where τ is the half-angle of rotation. The required radii of curvature for a set of mirrors is calculated by placing the radii that support the pattern at a particular rotation. Some of the multi-pass absorption cells that were designed during the course of the work are presented in the following sections.

2.4.4 206, 402m Cell

An astigmatic Herriott cell was designed which was capable of supporting both 206 and 402 m pathlengths. The base path length of the cell was 1m and the large pass number is achieved by using astigmatic mirrors of 100mm diameter. The spot patterns for the two configurations are shown in figure 2.17.

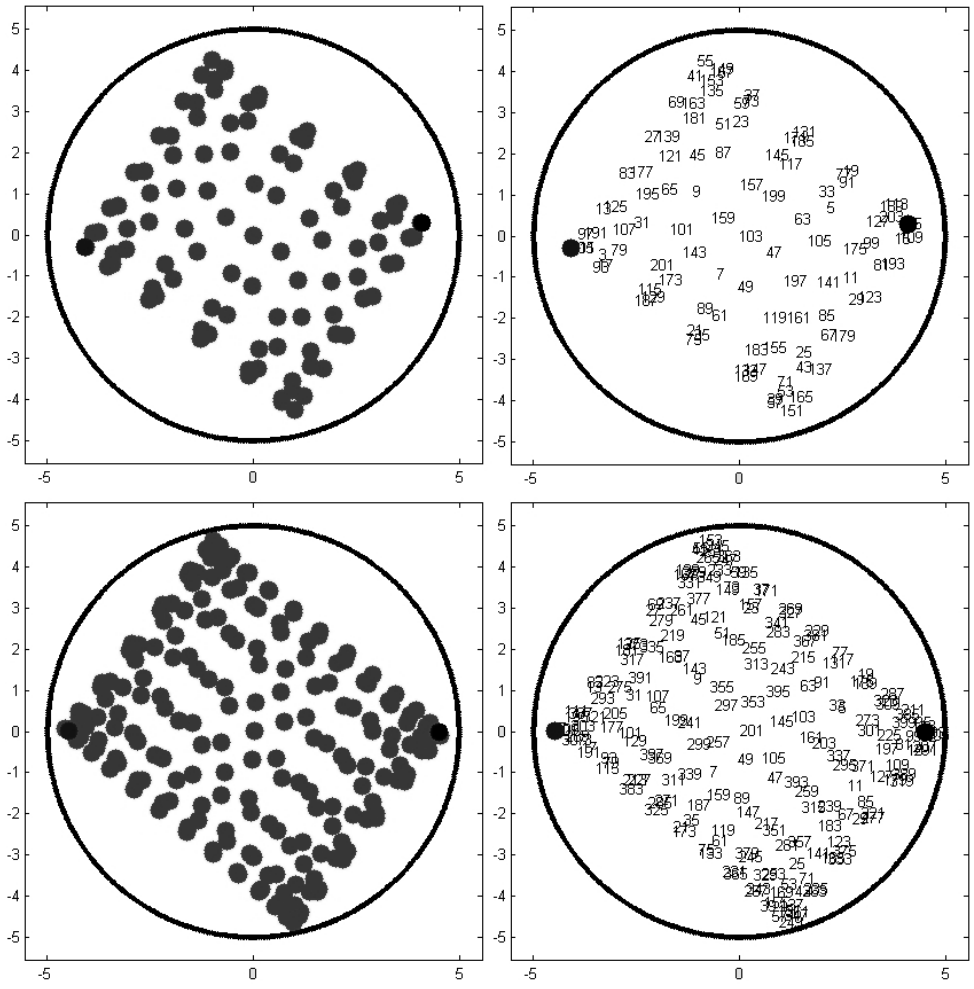

Figure 2.17: This shows the two patterns of 206 and 402 pass solutions. The pathlengths are therefore 206 and 402m for the respective patterns. The pass number diagrams are also shown.

The 206 pass solution can be found at the $\phi_x = -0.2287$ and $\phi_y = -0.1678$ coordinates, the $\{M_x, M_y, N\}$ for this pattern are $\{88, 92, 206\}$. The coordinates for the 402 pass solution are $\phi_x = -0.2266$ and $\phi_y = -0.1641$. The $\{M_x, M_y, N\}$ for the 402 pass solution are $\{172, 180, 402\}$. The ϕ_x, ϕ_y map for these patterns is shown in figure 2.18.

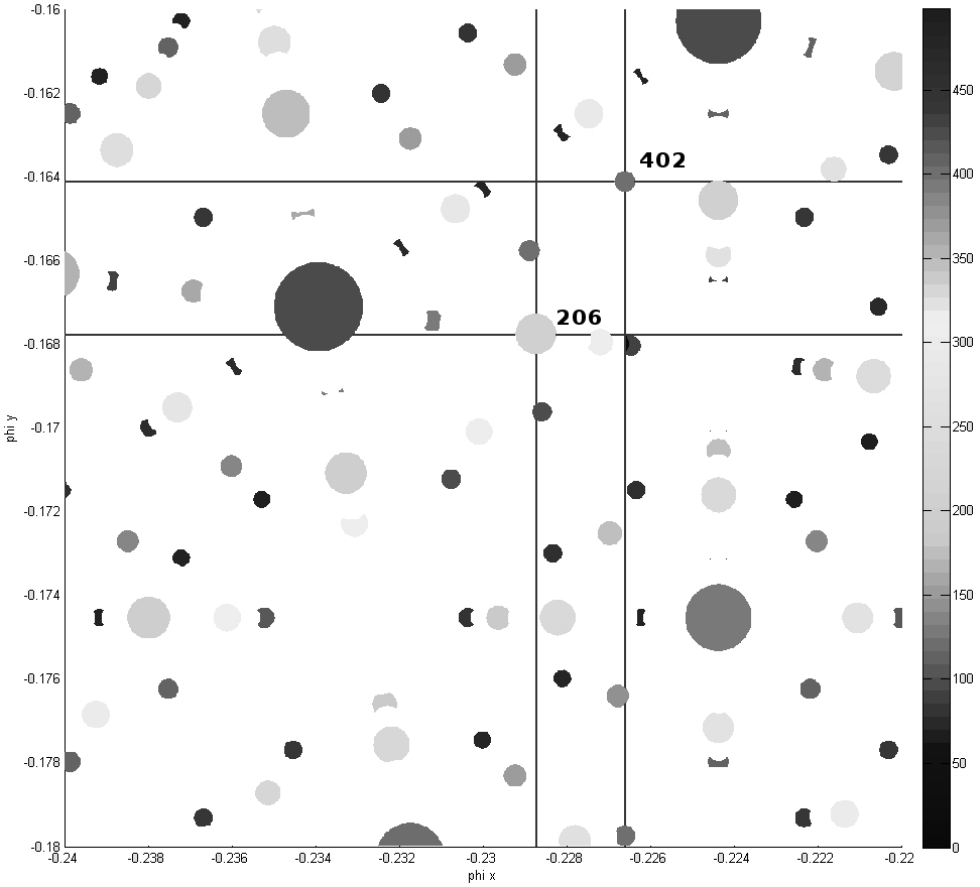

Figure 2.18: This shows the ϕ_x, ϕ_y map for the 206 and 402m cells, only the even patterns are shown.

Since the ϕ_x and ϕ_y for these patterns are so close it is possible to select a mirror specification that will be able to support both solutions. The radii of curvature for these mirrors was selected to be $R_x = 1295mm$ and $R_y = 1198mm$. A map of total pathlength as a function of mirror separation and back mirror rotation is shown in figure 2.19. This plot can be used to navigate through the observed configuration of the cell.

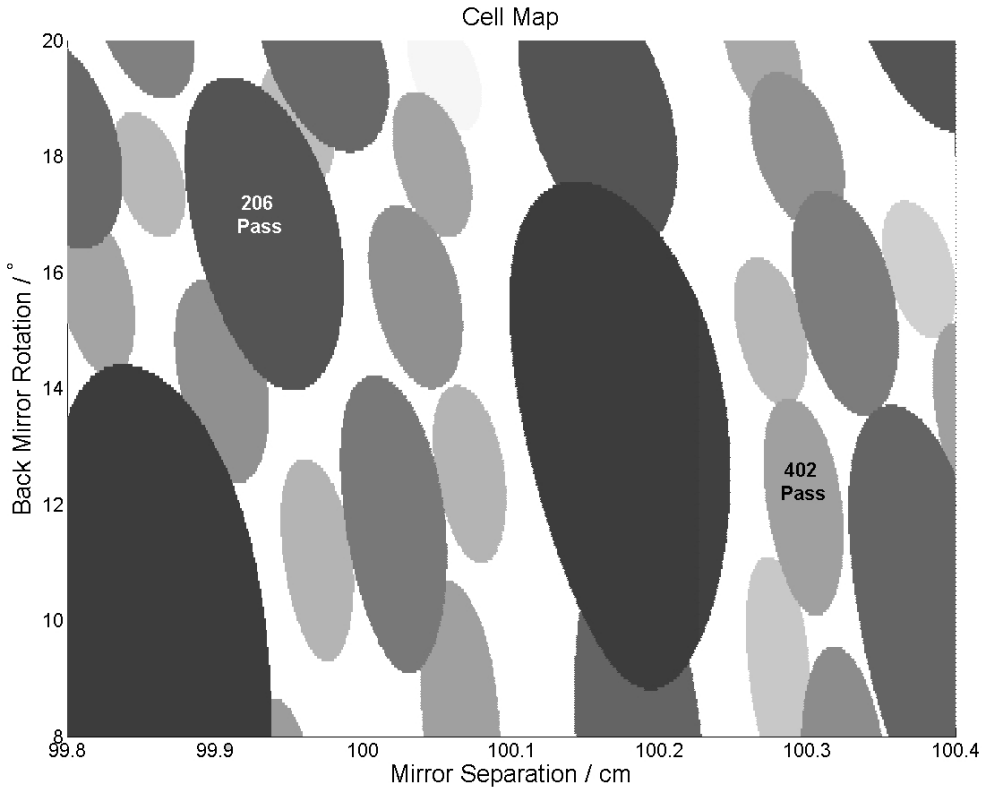

Figure 2.19: This shows the cell map for the 206 and 402 pass astigmatic mirrors. Both even and odd patterns are shown since both can be used to navigate to the correct solutions.

This cell was designed to support a very long pathlength, since the base path of the cell is approximately 1m for both solutions the pathlengths are 206 and 402m. In order to support the 402 pass solution and to allow a large enough input angle to the cell the mirror diameter was selected to be 100mm.

2.4.5 Dual Path Cell

A gas absorption cell which simultaneously supported two paths was designed to increase the range of detection for a particular application. It consisted of an astigmatic Herriott cell mirror solution with a dual input Herriott cell solution positioned at 90°. This arrangement is shown in figure 2.20.

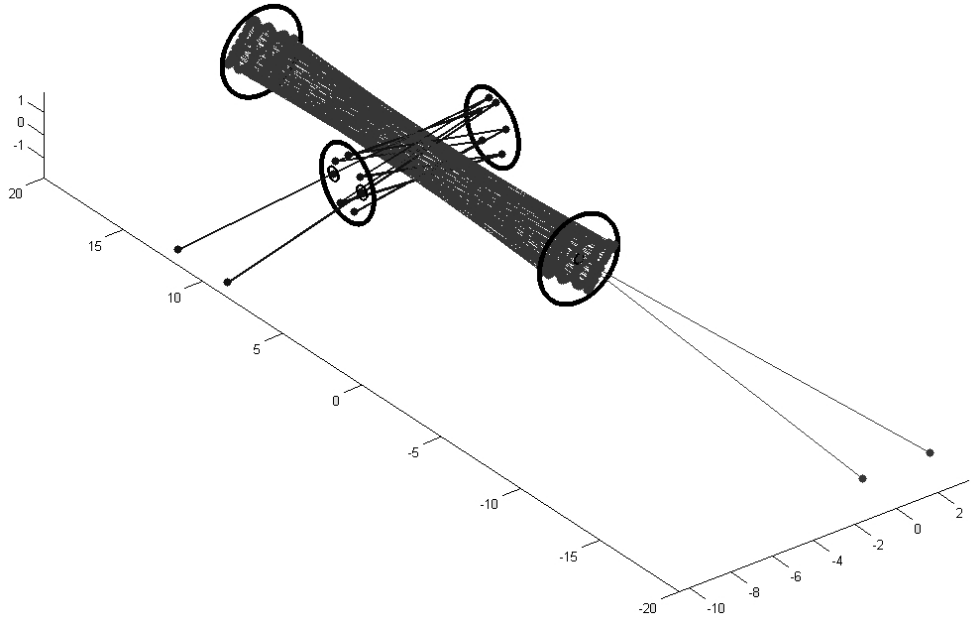

Figure 2.20: This shows the mirror arrangement of the dual path cell, which consists of an astigmatic Herriott cell together with a dual input Herriott cell.

The long path was a 210 pass, 42m solution with mirrors at a diameter of 38mm and a base pathlength of 20cm to provide a small volume (approximately 300mL). The spot pattern for this cell is shown in figure 2.21.

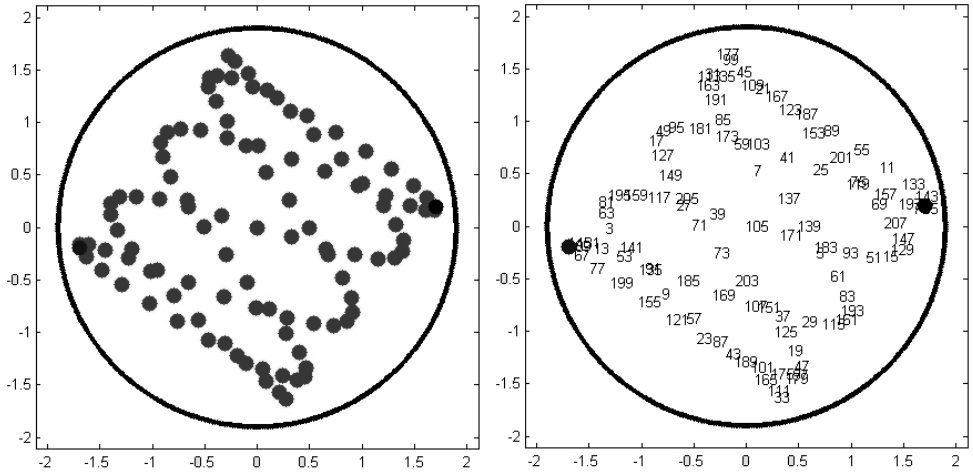

Figure 2.21: This shows the pattern of the 210 pass solution for the long path. The pathlength for this path is therefore 42m. The pass number diagram is also shown.

The 210 pass solution can be found at the $\phi_x = -0.1945$ and $\phi_y = -0.2843$ coordinates, the $\{M_x, M_y, N\}$ for this pattern are $\{92, 86, 210\}$. The ϕ_x, ϕ_y map for this solution is shown in figure 2.22.

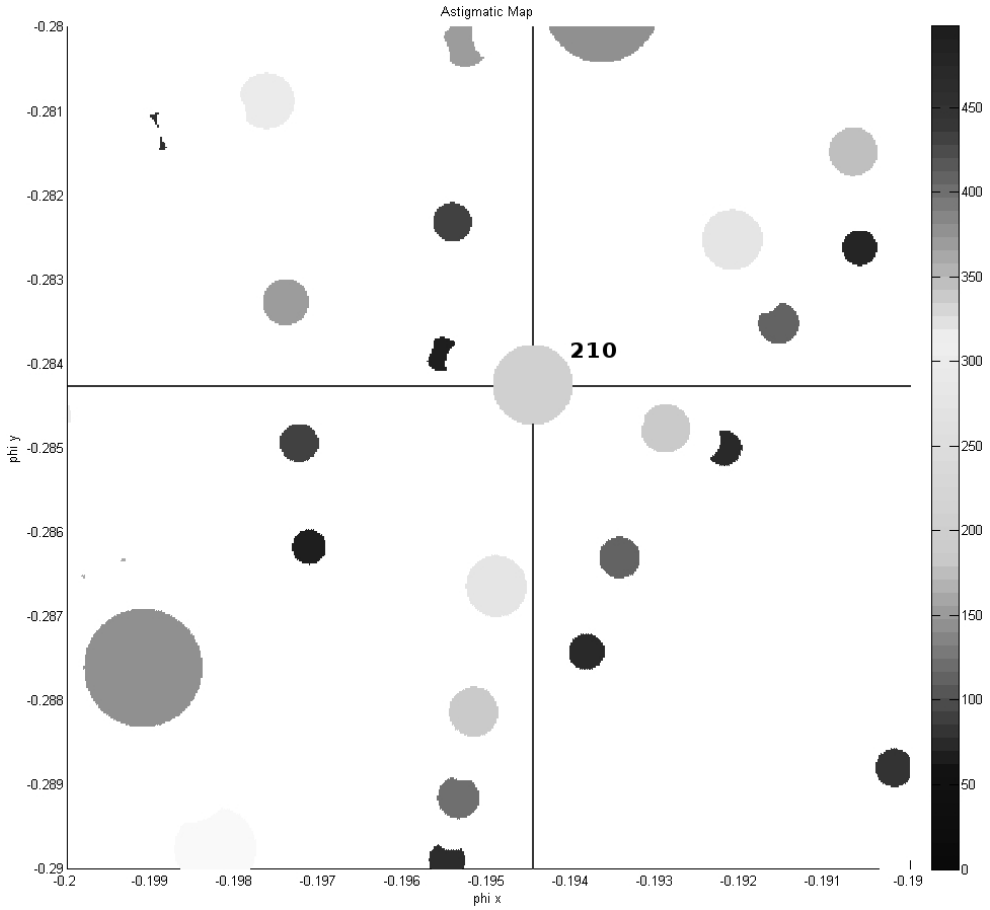

Figure 2.22: This shows the ϕ_x, ϕ_y map for the 210 pass solution, only the even solutions are shown.

The radii of curvature for these mirrors was selected to be $R_x = 247.4mm$ and $R_y = 278.85mm$. A map of total pathlength as a function of mirror separation and back mirror rotation is shown in figure 2.23. This plot can be used to navigate through the observed configurations of the cell.

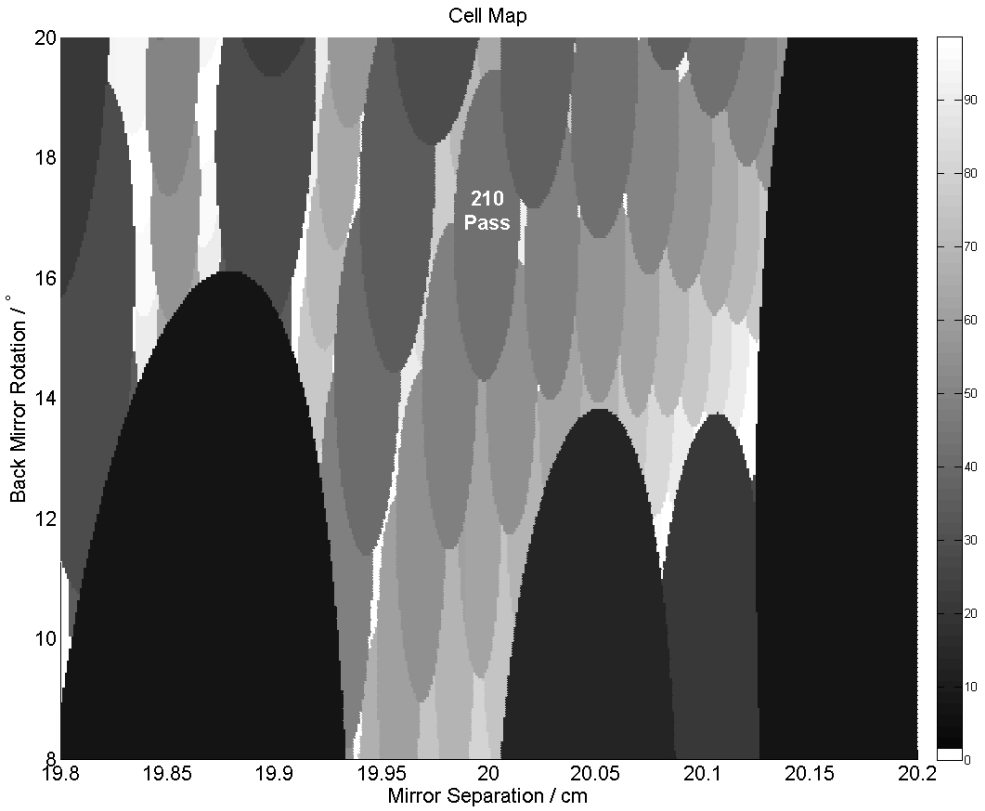

Figure 2.23: This shows the cell map for the 210 pass astigmatic mirror. Both even and odd patterns are shown since both can be used to navigate to the correct solutions.

The short path was a 12 pass, 84cm solution, the radius of the mirrors was tailored to 94.5mm to provide an optimum separation between the mirrors. This allowed the cell to be incorporated with the long path while maintaining a low volume. The spot pattern for this cell is shown in figure 2.24.

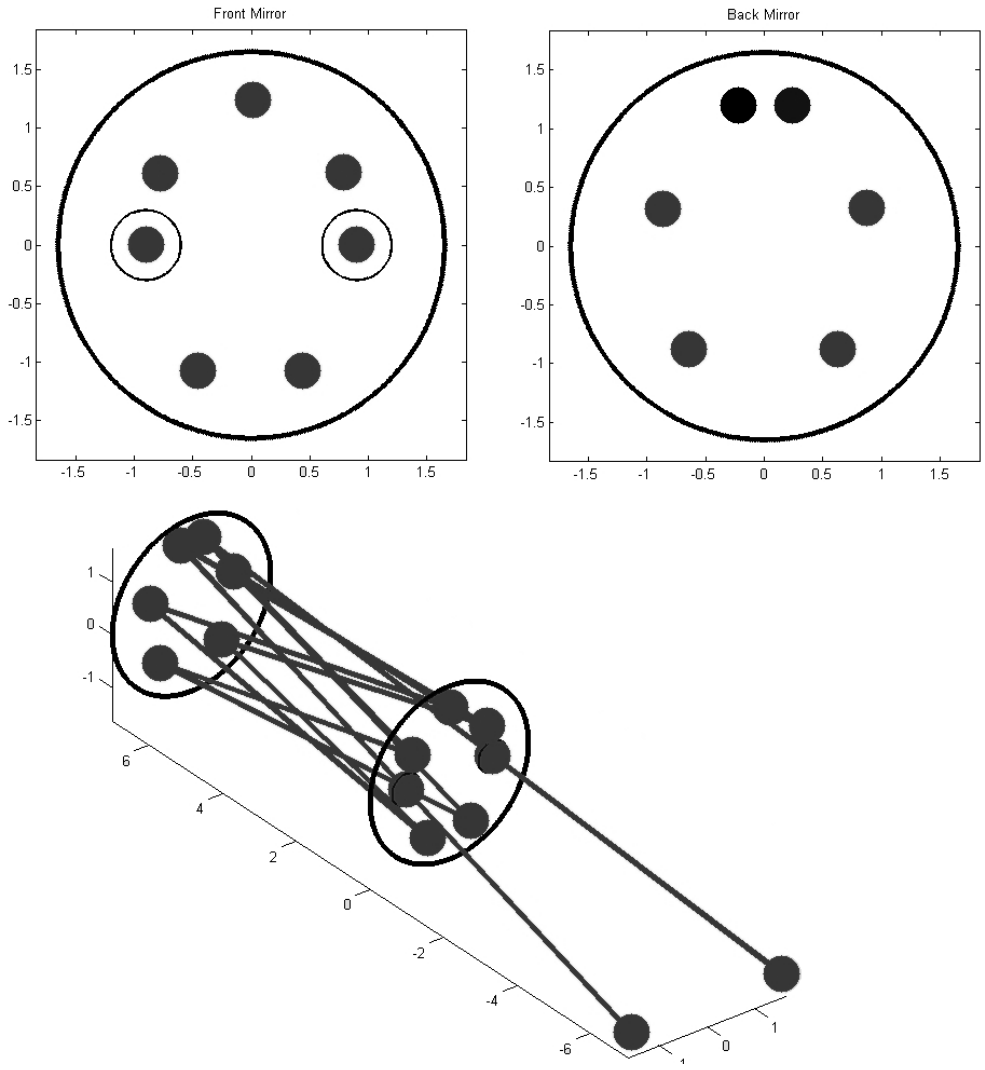

Figure 2.24: The spot pattern of the short path section of a dual path gas absorption cell. The base path is designed to be similar to the mirror diameter of the long path mirrors. The total pathlength of the short path section is designed to measure gas absorptions that would saturate the long path cell.

2.5 Conclusions

This chapter has covered the operational aspects of a laser based gas sensor from a hardware perspective. Specifically, the optical configurations that are necessary, such as extractive or *in-situ* arrangements, have been explained. The most relevant of these is the optical multi-pass cells that have been

studied and further developed to allow robust sensors to be constructed.

A few of the cell designs that were produced during this work have been presented. It is possible to increase the sensitivity of gas sensor by extending the pathlength of a multi-pass cell. This is an attractive method of increasing performance. However, there is only a linear benefit to be gained which is often found at the expense of sensor stability and increased costs.

References

[1] E Normand, M McCulloch, G Duxbury, N Langford, *"Fast, real-time spectrometer based on a pulsed quantum-cascade laser"*, Optics Lett. **28**, 1, 16-18 (2003)

[2] G Duxbury, N Langford, MT McCulloch, S Wright *"Rapid passage induced population transfer and coherences in the 8 micron spectrum of nitrous oxide"*, Mol. Phys. **105**, 5-7, 741-754 (2007)

[3] J.U. White, *"Long optical path of large aperture"*, J. Opt. Soc. Am. **32**, 285-288 (1942)

[4] D.R. Herriott, H. Kogelnik, and R. Kompfner, *"Off-axis paths in spherical mirror resonators"*, Appl. Opt. **3**, 523-526 (1964)

[5] D.R. Herriott and H.J. Schulte, *"Folded optical delay lines"* Appl. Opt. **4**, 883-889 (1965)

[6] A. Gerrard, B. Burch *Matrix methods in optics*, New York: John Wiley & Sons (1975)

[7] I. F. Howieson, *"Near infrared tunable diode laser absorption spectrometer for trace gas detection"*, PhD Thesis, Department of Physics and Applied Physics, University of Strathclyde, (1997)

[8] J.B. McManus, P.L. Kebabian and M.S. Zahniser, *"Astigmatic mirror multipass absorption cells for long-path-length spectroscopy"* Appl. Opt. **34** (18), 3336-3348 (1995)

[9] P.L. Kebabian, *"Off-axis cavity absorption cell"*, U.S. patent 5,291,265 (1994)

Chapter 3

Pulse Detection and Analysis

3.1 Overview

The QC laser and optics provide a method of probing a gas medium. The mid-infrared radiation produced contains information about the content of the gas medium. The radiation must be measured and averaged by a detection system in preparation for analysis, to extract the required information. The process of calculating an accurate concentration from a QC laser pulse is the purpose of the analysis. Fitting routine algorithms achieve this by modelling the expected results to best fit a spectrum obtained from a calibrated QC laser. The concentrations of the gases detected by the QC laser are then equivalent to those used in the model to achieve the best fit.

Before a fitting routine can be used the QC laser must have its wavelength calibrated, the concept of a calibrated QC laser is explained in section 3.3. The fitting routines determine the composition and concentrations of a gas mix by comparing the recorded data to simulations of the absorbance of various gases, the theory behind this model is explained in section 3.4. This is followed by section 3.5 which explains the link between the recorded and simulated data, this must be understood to make effective comparisons. The remaining sections discuss the two principle components of a fitting routine,

these are the minimisation routines used to reach the best fit and the objective functions which perform the comparison between the recorded data and the simulations generated by the model.

3.2 Detection and Digitisation

Due to the pulse length that is applied to QC lasers when using the intrapulse method and the temporal resolution required to properly interpret the spectra, a fast and accurate method of detecting pulsed mid-infrared radiation is required. The mid-infrared pulse must be detected and continuously converted to an analogue electrical signal. Then the electrical signal must be sampled into a digital signal, this digital signal is then sequentially averaged in preparation for analysis. An example of such a system is shown in figure 3.1.

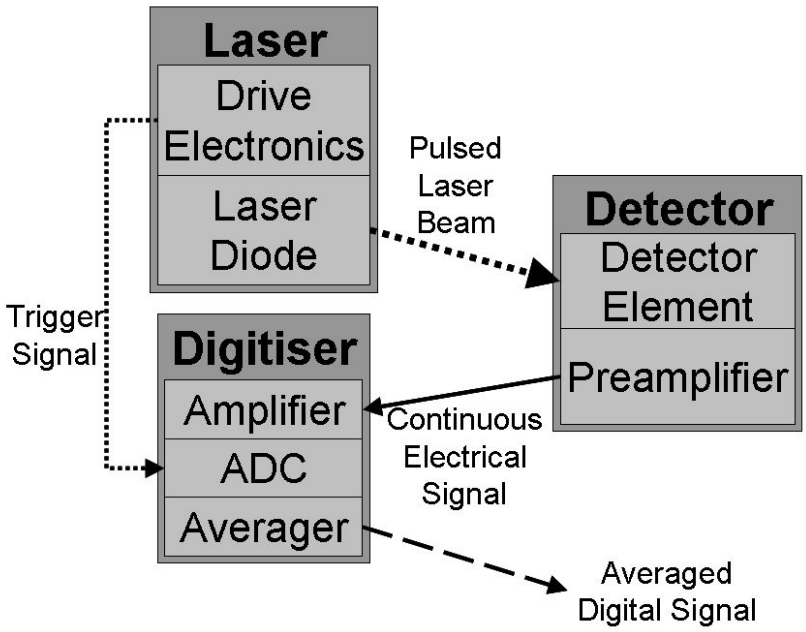

Figure 3.1: An example of a detection and digitisation system for pulsed mid infrared radiation. A pulsed beam is produced by driving a QC laser diode with current pulses. The beam is directed to a detector element where the optical signal is converted to an electrical signal, a preamplifier then prepares the signal for the digitiser. The signal is amplified, then sampled by an analogue to digital convertor (ADC). The ADC is synchronised to the pulse by a trigger signal supplied by the laser drive electronics. A sequential averager then co-adds a number of pulses together to form the averaged digital signal.

The typical peak laser power of a QC laser pulse after passing through an astigmatic Herriott cell or an environment with a high particulate matter can be as low as $5\mu W$. The signal must be sampled with enough time resolution to properly represent the absorption line features present on the laser pulse. The value of this resolution depends on the absorption line under study and the pressure of the gas mix, however a sample rate of 1 $sample/ns$ is usually sufficient for measurements at atmospheric pressure. The bandwidth of the detection system can influence the shape of the absorption lines, if the bandwidth is too low then the higher frequency components of the signal are lost. This can cause errors in the concentration values that are returned by the sensor. If a high measurement frequency is required then the repetition

rate of the QC laser can be as high as 100 kHz. The digitiser must be capable of recording and averaging the signal received from the detector at this speed.

3.2.1 Detector

The mid infrared wavelengths require a material system with a small band gap, this leads to the use of a mercury, cadmium, telluride (HgCdTe or MCT) heterostructure material system. An immersion lens or, if not available, an external lens is used to capture as much light as possible and focus it onto the active area where the light is converted to an electrical signal. The high speed requirement motivates the use of a photodiode with a small active area. An example power budget for a typical QC laser is shown in table 3.1.

Element	Attenuation	Typical Power
QC Laser		200 mW
Collimation Optics Transmission	-4.2 dB	76 mW
200 Pass Astigmatic Herriott Cell	-7 dB	15 mW
Immersion Lens Collection	-15 dB	0.45 mW
Immersion Lens Transmission	-1.5 dB	0.32 mW
Detector Active Area Collection	-9.2 dB	0.04 mW

Table 3.1: Power budget for a typical QC laser based gas sensor.

Photovoltaic detectors create a voltage and current in response to an incident photon, while photoconductive devices change their resistance. In order to measure the change in resistance a low noise bias current must be applied to the device. The majority of the data presented in this thesis was recorded using photovoltaic photodiodes because of the response and high speed offered by these devices.

The performance of a photodiode can be characterised by its responsivity and its normalised detectivity ($D^{\star}$). The responsivity is the ratio of generated photocurrent to incident light power, this is typically expressed in A/W. $D^{\star}$ is the detectivity normalised to the active area of the photodiode. Detectivity

is the inverse of the noise equivalent power (NEP), which is the minimum input optical power required to generate a photocurrent which is equal to the rms noise current in a 1 Hz bandwidth.

The small energy band gap required to detect infrared wavelengths leads to high thermal carrier generation and recombination. This means the detectors are susceptible to thermal noise and that performance can be improved by cooling. Detectors are often cryogenically cooled with liquid nitrogen, however recently more advanced detectors that are Peltier cooled have become available. The output from the detector element is normally not suitable to be immediately sent to a digitiser. The electronic signal generated by the detector is usually connected to the input of a preamplifier. This device can either be integrated with the detector or a separate device can be placed between the detector and the digitiser. To resolve the QC laser pulse into the necessary time spacing the bandwidth must be greater than 500MHz.

The data presented in chapter 4 was largely recorded using Peltier cooled detectors with internal pre-amplifiers, these detectors were purchased from Vigo Systems [1]. However, the data presented in section 4.5 was recorded using a liquid nitrogen cooled detector from Kolmar [2], this detector was used together with an external high-speed pre-amplifier. In both cases the recorded data was of a high enough quality to allow accurate measurements to be made. While different detector technology was used in gathering data the detectors themselves were never a direct subject of the research in this thesis.

3.2.2 Digitisation

The signal generated by a detector is a continuously variable analogue signal. In order to perform mathematical analysis using a computer the signal generated by the detector must be digitised. This means an analogue to digital converter (ADC) is used to periodically sample the analogue signal, each sample is represented as a binary number. This process allows a pulse to be

recorded, a sequential averager can then co-add multiple pulses to reduce the laser noise and the digitisation of the signal. The averaged QC laser pulse can then be provided to a computer based fitting routine that performs the mathematical calculations necessary to measure the composition and concentrations of the gas mix under study. All of the QC laser data in this thesis was recorded either with a Cascade Technologies Averager [3] or an Acqiris Digitiser [4] with averaging capabilities.

The precision to which the ADC will encode a sample depends on the resolution of the ADC. Both types of digitiser used to record the data in this thesis were 8-bit. This means that over the range of the analogue input $2^8 = 256$ discrete levels can be used, these levels are linearly spaced across the input range. This introduces digitisation noise, however once an average of several hundred pulses has been recorded this noise is rendered negligible. The sample rate of both digitisers had a maximum value of $1 GigaSample/s$. The input range in both cases was configurable allowing the digitiser to measure a variety of QC laser pulse powers. The bandwidth of the Acqiris digitisers used was $1 GHz$, this allowed measurements of absorption lines to be recorded at very low pressures. The bandwidth of the Cascade averager was typically $200 - 600 MHz$ with a planned bandwidth of $900 MHz$, this allowed measurements to be recorded at atmospheric pressures or below. However at pressures below $200 Torr$ the effect of digitiser bandwidth on the absorption line shapes was significant enough to make high accuracy measurements difficult.

Once a QC laser pulse has been rendered into a format that can be analysed by a computer based algorithm it is possible to retrieve concentration data. The methods that were used to achieve this are presented in sections 3.4 to 3.7.

3.3 Laser Calibration

In order to compare the spectra returned by the QC laser to the data generated by a model the absolute wavenumber progression with time of the laser must be characterised. This is achieved by recording and analysing different averaged pulses from the laser. An example of these pulses is shown below in figure 3.2.

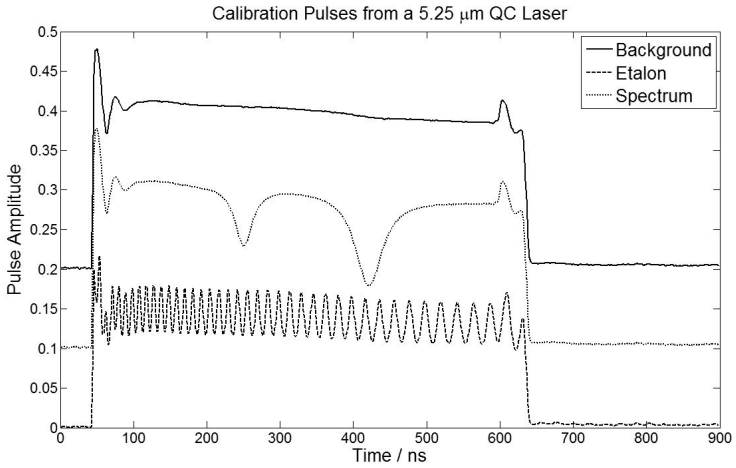

Figure 3.2: Pulses from a $5.25\mu m$ QC laser used to calibrate the absolute wavenumber tuning, the pulses have been offset for clarity. The dashed etalon pulse is used to calculate the relative tuning and the dotted spectrum pulse is used to find the absolute wavenumber progression of the pulse. The background pulse is only necessary in cases where the etalon or spectrum pulses are difficult to analyse.

The background pulse is used to calculate the transmission of the other two pulses and is not strictly necessary. The etalon pulse is used to calculate the tuning of the laser and the spectra pulse is used to determine the exact wavenumber value of a point on the pulse.

3.3.1 Etalon Pulse

The tuning or relative change in wavenumber can be accurately determined by passing the laser beam through a Fabry-Perot etalon. Germanium is a

convenient material to use in the infrared due to its high transmission as well as having the highest refractive index of any optical material in the infrared. Reflections within the etalon lead to constructive interference when the reflections are in phase and destructive interference when they are out of phase. This leads to the transmission spectrum exhibiting peaks of equidistant wavelength shift. This shift is called the free spectral range (FSR) of the etalon, this is calculated in wavenumber as shown below in equation 3.1.

$$FSR = \frac{1}{2nd} \tag{3.1}$$

Where n is the refractive index of the material and d is the optical length of the etalon. The refractive index varies with both wavelength and temperature and the material expands with increasing temperature. The FSR as a function of wavelength for different temperatures is shown below in figure 3.3, this plot is for a Germanium etalon of one inch in length.

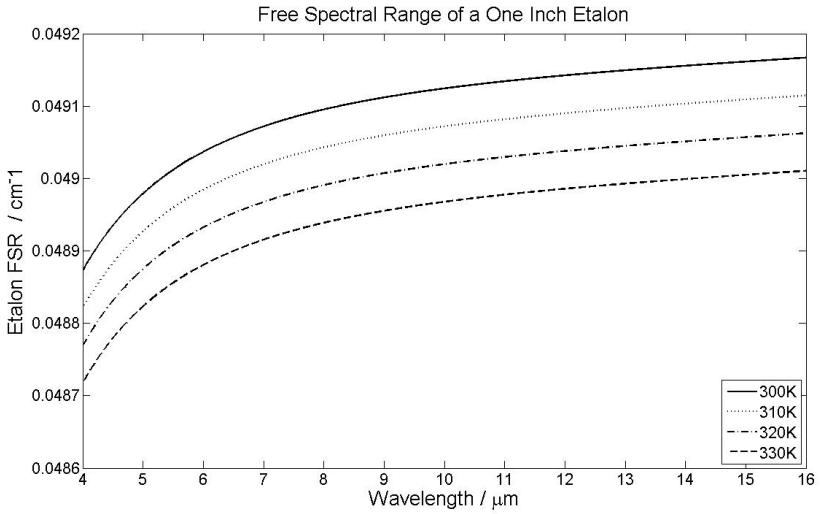

Figure 3.3: This plot shows the free spectral range (FSR) of a 1 inch Ge etalon at several temperatures as a function of wavelength. The change in FSR over the wavenumber range covered by a single QC laser pulse is insignificant for a stable temperature, however when dealing with temperature variations or multiple QC lasers it may be necessary to take the variations into account.

While the FSR does vary as shown above it is well within the resolution

of any single QC laser pulse. This means that a germanium etalon can be used to characterise the tuning of a QC laser. In the case where highly accurate tuning information is required the change in FSR with wavelength and temperature should be taken into account. An example of the fringe pattern that is produced is shown in figure 3.4.

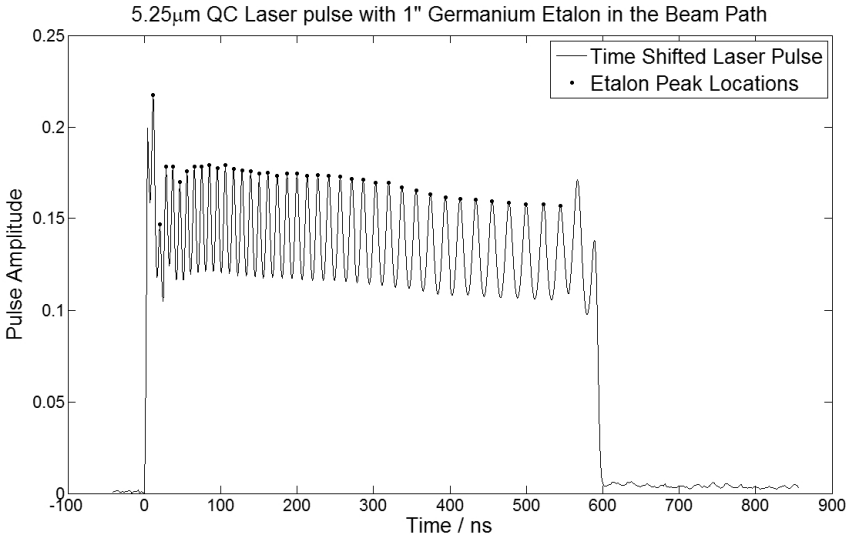

Figure 3.4: A 5.25μm QC laser pulse with a 1" Germanium etalon placed within the path of the beam. This results in interference fringes, the peaks have been highlighted. The temporal distance between peaks is used to calculate the relative tuning of the laser. The start of the laser has been set to a time of 0 seconds to provide a reference point for the tuning.

Using an etalon allows the relative tuning of the laser to be calculated since the wavenumber spacing between consecutive fringe peaks is a known value. The tuning calculated from the pulse in figure 3.4 is shown in figure 3.5.

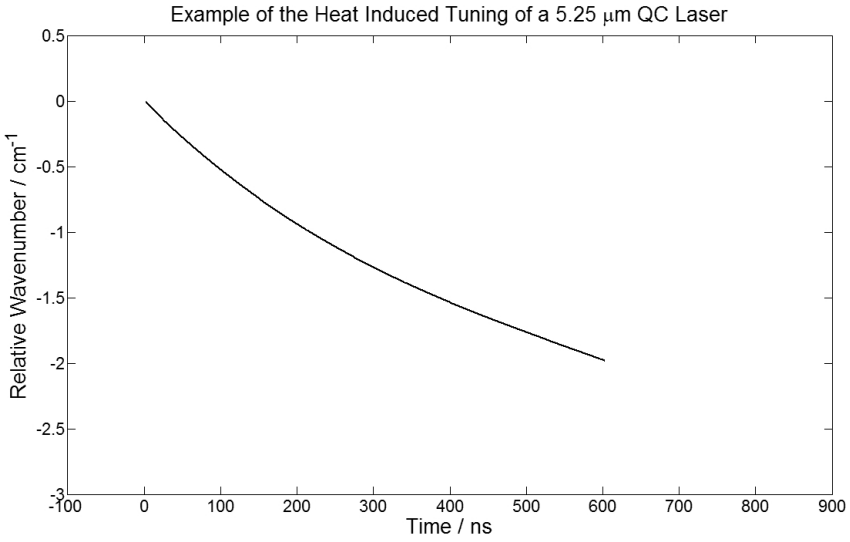

Figure 3.5: The resultant relative wavenumber tuning of the $5.25\mu m$ QC laser pulse shown in figure 3.4. The wavenumber at a time of 0ns is the starting wavenumber of the pulse.

3.3.2 Spectrum Pulse

Once the tuning of the laser is known the exact wavenumber of a particular point on the pulse must be determined to fully characterise the spectral window that is produced by the QC laser pulse. Normally the approximate wavelength of the laser is known from its specification, however this can be more accurately measured by using a high resolution Fourier Transform Spectrometer (FTS). Making FTS measurements provides other useful information regarding the spectral quality of the laser. A laser that is not single mode may produce spectra that are unusable.

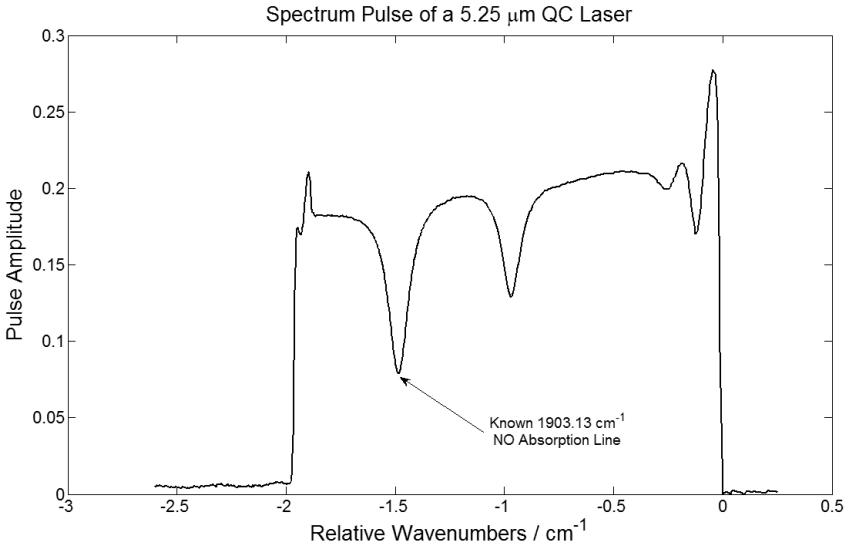

Figure 3.6: The relative tuning of the spectrum pulse of the $5.25\mu m$ QC laser can now be shown. On the spectrum are two known NO absorption lines which are used to shift the relative tuning to an absolute tuning.

Once an approximate wavelength is determined the laser can be fully characterised by introducing a gas with known absorption lines onto the laser pulse. By observing one or more of these known absorption lines on the pulse, the absolute wavelength scale is computed by anchoring the relative calibration to this known point. Once the wavenumber range covered by the laser is known it then becomes possible to simulate various spectra for comparison with real data obtained from the QC laser. The resulting calibrated QC laser pulse is shown in figure 3.7.

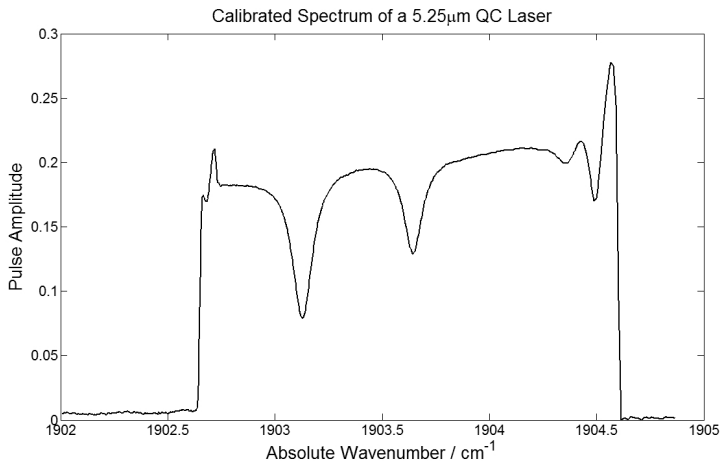

Figure 3.7: The calibrated spectrum of the $5.25\mu m$ QC laser pulse, which can now be used to analyse the presence and concentration of various gases.

3.4 Spectral Simulation

To calculate the concentration of a gas, comparisons must be made between data recorded using a QC laser and data generated by a model. Minimisation functions are used to closely match the two and hence find values for the concentrations. In order to achieve this there must be a method of calculating the spectrum of a gas based on physical values such as pressure, temperature, pathlength and concentration. The transmission of a pulse is the normalised amplitude that is observed by a detector, the absorbance describes the absorbing effect of a medium, they are related as shown in equation 3.2. The units used in equations 3.2, 3.3, 3.4, 3.5 and 3.6 can be found in table 3.2.

$$Transmission = e^{-Absorbance} \tag{3.2}$$

The absorption coefficient, α, relates the absorbance to the pathlength, l, through a medium with concentration, C, as shown below in equation 3.3.

$$Absorbance = \alpha l C \tag{3.3}$$

The absorption coefficient is a function of wavenumber and can be calculated from several known parameters that describe an absorption line. These parameters also determine how the line responds to changes in pressure, pathlength and the presence of other gases. Once the absorption coefficient is known the Beer-Lambert law can be used to calculate absorbance spectra. The absorption coefficient can be calculated using equation 3.4, [5]. This equation assumes that there is no pressure induced line shift, since this is an effect that is normally only observed at high pressures. In the cases where the effect is observed the wavelength shift observed in the spectrum can be corrected with calibration adjustment factors.

$$\alpha = S_\eta(T)\,\frac{\gamma}{\pi\left(\gamma^2 + (\nu - \nu_\eta)^2\right)} \tag{3.4}$$

There are two principal components to this equation, first is the $S_\eta(T)$ term, this describes the temperature adjusted intensity of an absorption line and it can be calculated using equation 3.5.

$$S_\eta(T) = S_\eta(T_{ref})\,\frac{Q(T_{ref})}{Q(T)}\,\frac{e^{(-c_2E_\eta/T)}}{e^{\left(-c_2E_\eta/T_{ref}\right)}}\,\frac{\left[1 - e^{(-c_2\nu_\eta/T)}\right]}{\left[1 - e^{\left(-c_2\nu_\eta/T_{ref}\right)}\right]} \tag{3.5}$$

The line intensity which is known at a reference temperature is adjusted to the measured or supplied temperature. The remainder of equation 3.4 describes a lineshape function, the γ term can be calculated using equation 3.6 below. Lineshape and QC laser linewidth is discussed in further detail in section 3.5.

$$\gamma = \left(\frac{T_{ref}}{T}\right)^n \left(\gamma_{air}\,(P - P_S) + \gamma_{self}P_S\right) \tag{3.6}$$

The γ term determines the broadening of the absorption line, it is based on contributions from the temperature, pressure and gas concentration con-

ditions of the gas. The partial pressure of the gas and the total pressure of the gas mix are related through the relative concentrations of each of the gases. The γ_{air} and γ_{self} coefficients are used to calculate the pressure component of the broadening. The effect of temperature on the broadening is calculated by using the coefficient of temperature dependence of the air-broadened halfwidth, n. The various elements of equations 3.4, 3.5 and 3.6 are defined in table 3.2.

Constant	Units	Description	Source
S_η	$cm^{-1}/molecule\,cm^{-2}$	line intensity	database
Q	-	total internal partition function	database
E_η	cm^{-1}	lower state energy of transition	database
γ_{air}	cm^{-1}/atm	air-broadened HWHM	database
γ_{self}	cm^{-1}/atm	self-broadened HWHM	database
n	-	temperature dependence of γ_{air}	database
ν_η	cm^{-1}	line position	database
c_2	$cm\,K$	second radiation constant	constant
T	K	temperature	variable
P	atm	pressure	variable
C	$molecule\,cm^{-3}$	concentration	variable
l	cm	pathlength	variable

Table 3.2: Definition of the terms used in spectral simulation equations and their respective sources. The terms with database as the source are characteristics of absorption lines that are constant for an individual absorption line. They are usually obtained from a spectral database. The units of each of the constants is also included.

In figure 3.8 a comparison is made between a transmission spectrum calculated from a $5.25\mu m$ QC laser and a transmission spectrum that was generated using a model based on the above theoretical equations.

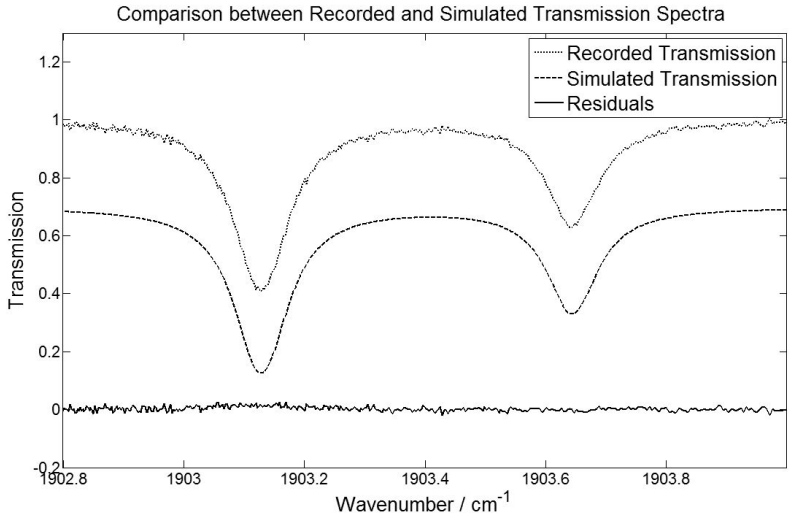

Figure 3.8: A comparison between a transmission spectrum recorded from a $5.25\mu m$ QC laser and a simulation from a spectroscopic model. The simulated spectrum has been offset for clarity, both spectra show absorptions from NO and the difference between the two transmissions is plotted as the residuals.

3.4.1 Spectral Databases

To produce accurate simulations of gas absorption there must be quantitative data on the spectral absorption lines and the environmental conditions. The data that is required is indicated in table 3.2, the variables are typically either controlled or measured, however information about the absorption lines themselves is also required. This information is often available from a number of sources, data on common atmospheric gases is often collated into an atmospheric database such as HITRAN [5, 6] or GEISA [7]. These databases contain information on individual absorption lines for a number of gases.

HITRAN is a spectral database that has been built up over several years with contributions from research groups around the world. It is accompanied the HITEMP (high-temperature spectroscopic absorption parameters) [8], HITRAN is an atmospheric database which aims to cover the most common molecules that are found in the atmosphere. The data contained within

HITRAN is referenced to 296K, the data in HITEMP provides the necessary information to adjust the HITRAN parameters to other temperatures. The data is compiled from both observations and theoretical calculations and as such the accuracy and precision of the data can be variable. Also for a given gas the database will not always offer full coverage of the absorption lines, some may be missing or the data can be incomplete. Care should be taken to appreciate the validity of any data used to analyse the results of spectroscopic measurements.

The purpose of HITRAN is to build a database of well known atmospheric gases. As such the data best describes the absorption lines of those gases at atmospheric temperature and pressure. The data available on the γ_{air} coefficient is often more accurate and precise than the data available on γ_{self}, which only provides a significant contribution when the partial pressure of the gas is high. This is because in atmospheric conditions the γ_{air} contribution dominates, this can present problems when working in conditions that are not similar to those encountered in the atmosphere. Another issue arises from absorption lines that are only significant at higher than atmospheric temperatures. The responsive of any absorption line to temperature can be poorly characterised, however in certain cases lines that are only significant at elevated temperatures are entirely absent.

The absorption line information contained in a database can be insufficient for a particular application or experiment. This can be due either to lack of coverage by a line database or because the data is not accurate enough. More accurate or missing data can sometimes be acquired through research carried out by other organisations. When this is not possible experiments must be carried out to characterise the necessary absorption lines. Institutions such as the National Physical Laboratory (NPL) or the Molecular Spectroscopy Facility (MSF) at Rutherford Appleton Laboratories (RAL) offer equipment that can be used to perform these measurements. The experiments involve making high resolution measurements on the absorption lines of interest at a variety of environmental conditions.

3.5 Lineshape, Linewidth and Resolution

The peak of an absorption line exists at a certain wavenumber and the exact location of this peak can be shifted by physical processes such as Doppler effects. An absorption line also has a non-zero linewidth meaning that it extends over a range of wavenumbers. There are a number of reasons why this happens and the following sections describe the results of this on the measured lineshapes. The shape of an absorption line can be described by a convolution of Lorentzian and Gaussian functions to form a Voigt [9] function as shown in 3.9. At times an absorption line will be dominated by either the Lorentzian or Gaussian component and this is largely determined by the pressure of the gas mix.

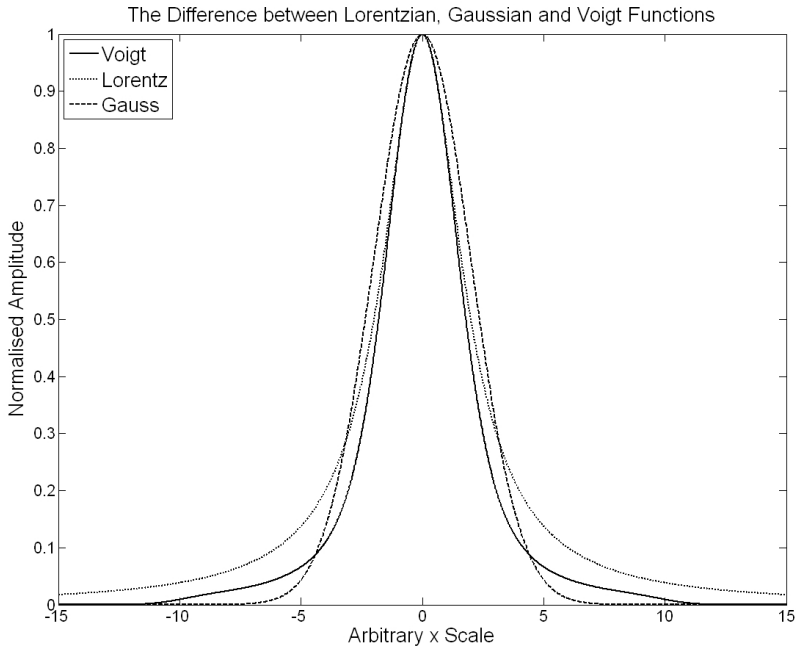

Figure 3.9: This shows the difference between a Lorentzian and Gaussian profiles. The resulting Voigt profile when the two are combined in a convolution is also shown. The area under each of the profiles is the same in this plot.

The method used to measure these absorption lines is a QC laser tuned continuously in time which is sampled periodically by a detection system as described in section 3.2. The emission from the QC laser also has a non-

zero linewidth and this also affects the resulting measurements. The most accurate measurement performance is obtained when all of these processes are accounted for during the analysis of spectra, however there are also conditions where approximations can be made or where the effects of certain processes are negligible and can therefore be discounted.

3.5.1 Gaussian Function

The shape of an absorption line is affected by the thermal motion of the atoms or molecules in the gas mix because of the Doppler effect. Since the atoms or molecules in a gas mix are in motion the frequency of light that they experience depends on their direction of travel relative to the beam. This is an example of inhomogeneous broadening, since each atom or molecule has a different response due to the spread of velocities. This results in a range of absorbed frequencies of light, this range can be characterised by a Gaussian function. The function for a Gaussian profile is shown in 3.7.

$$G(x) = \frac{1}{\sigma\sqrt{2\pi}} \exp\left(\frac{-(x-\mu)^2}{2\sigma^2}\right) \tag{3.7}$$

Where σ is the standard deviation of the distribution and μ is the centre point of the distribution. For a Doppler broadened absorption line this standard deviation is given by 3.8.

$$\sigma = \lambda_0\sqrt{\frac{kT}{mc^2}} \tag{3.8}$$

Where k is the Boltzmann constant, T is the temperature, c is the speed of light and m is the mass of the atom or molecule. When a beam of light interacts with a particle, the particle can be moving away from or towards the beam. If the particle is moving away the absorbed frequency of light is lower than the case when the particle is stationary. When the particle is moving towards the beam the opposite applies. The movement of the particle

is caused by thermal motion, when there is a group of particles the absorbed radiation is spread over a range described by the equations above.

3.5.2 Lorentzian Function

An absorption line can also be broadened through collisional processes, this is known as pressure broadening since increasing the pressure of a system will increase the number of collisions between atoms and molecules. Since all the atoms or molecules experience the pressure increase this is an example of homogeneous broadening. This can be characterised by a Lorentz function, also known as a Cauchy distribution. Equation 3.9 shows the standard form of the Lorentz function.

$$L(x) = \frac{1}{\pi}\left[\frac{\gamma}{\gamma^2 + (x - x_0)^2}\right] \tag{3.9}$$

Where γ is the half-width at half-maximum (HWHM) and x_0 is the centre point of the distribution. For a pressure broadened absorption line γ is defined by 3.10.

$$\gamma = \left(\frac{T_0}{T}\right)^n \left(\gamma_{air}\left(P - P_S\right) + \gamma_{self} P_S\right) \tag{3.10}$$

Where T and T_0 are temperatures, P and P_S are the pressure and partial pressure respectively and the γ_{air} and γ_{self} terms are physical constant of the absorption line itself.

3.5.3 Voigt Function

The Voigt function is formed from the combination of Gaussian and Lorentzian profiles. It can be calculated by convolution of the Lorentzian and Gaussian profiles as shown in 3.11.

$$V(x) = \int_{-\infty}^{\infty} G(x)L(x)dx \tag{3.11}$$

At a low pressure the shape of an absorption line is dominated by thermal motion and hence most closely resembles a Gaussian function. As the pressure increases the pressure broadening begins to become apparent and the line will most closely resemble a Voigt function. Beyond a certain pressure the Lorentzian profile will dominate the Gaussian contribution.

3.5.4 System Resolution

The previous sections describe the spectral behaviour of an absorption line. The process of sampling the line with a QC laser and then detecting and digitising the signal can alter the appearance of the line. The resolution of the system is related to the bandwidth - duration product, this is referred to as the uncertainty relation [10]. The bandwidth - duration product cannot be less than a particular value, C. The value of C is determined by the pulse shape. For a Gaussian time window, $\Delta t \Delta \nu \geq C = 0.441$. The resolution can be calculated using 3.12. As the chirp rate, $d\nu/dt$, of the laser is slowed the resolution of the instrument increases [11].

$$\Delta\nu = \sqrt{C\frac{d\nu}{dt}} \tag{3.12}$$

The 5.25 μm QC laser described in section 2.2 has a chirp rate of 100 MHz/ns. This is used to calculate a resolution of 210 MHz or 0.007 cm^{-1}, assuming a Gaussian pulse profile. If the limiting case of $C = 1$ is used then the resolution is 316 MHz or 0.01 cm^{-1}. At atmospheric pressures the effect of this resolution will be negligible, however as the pressure decreases the effect upon the recorded spectrum will become increasingly significant.

3.6 Minimisation Functions

The goal of a fitting routine is to calculate the concentration of a gas or gases by analysing the laser spectrum recorded by a gas sensor. This is typically achieved by using a minimisation function to alter the input values to an objective function in order to find a best fit to the recorded data. The inputs to the objective function define the parameters that are used to generate absorption spectra, the objective function then compares the recorded data to the simulation. Once this has been done the objective function provides a function value or score which the minimisation function uses to grade the combination of parameters that were used. Over time the minimisation function finds the parameters that result in the best fit of the simulation to the recorded data, the algorithm that is used to do this can vary. The algorithms that have been used to analyse the data within this thesis are described in the following sections. A high level flow chart of a fitting routine is shown in figure 3.10.

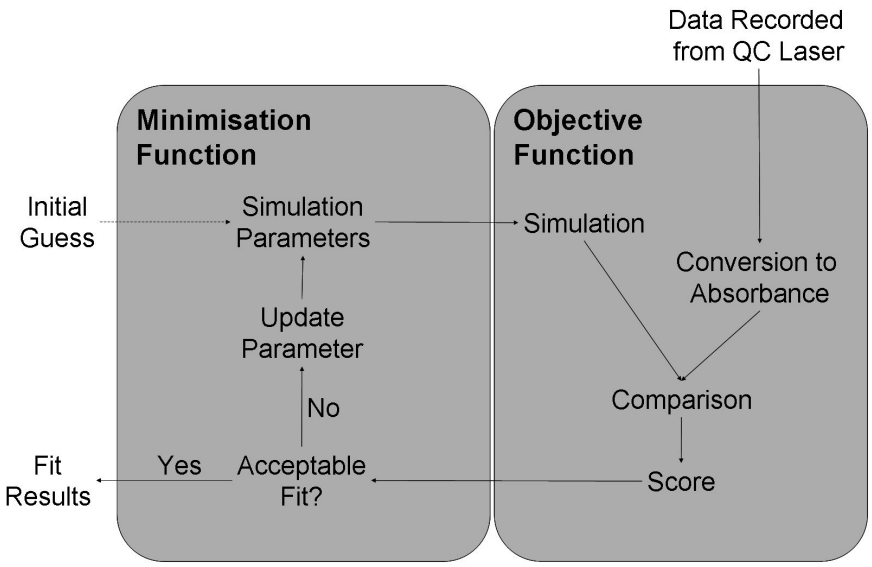

Figure 3.10: This shows a flow diagram indicating the relationship between the minimisation and objective functions in a fitting routine. The actual internal process can differ depending on the algorithms used. The process begins with data recorded from a QC laser and an inital starting point. The starting point is often the results from a previous fit. The minimisation function begins by scoring the initial guess by comparing a simulated spectrum to the QC laser spectrum. The fit parameters are changed and the minimisation function observes the effect on the score produced by the objective function. This allows the minimisation function to move towards a better solution.

The decision as to whether a simulated fit to the recorded data is acceptable depends on the algorithm used, however for a given algorithm there is usually an inverse relationship between the accuracy of the fit and the time required to reach it. An example of both good and bad fits is shown in figure 3.11. The bad fit is shown in figure 3.11(a), this is from the start of the minimisation process, after the algorithm is near to completion the fits become closer to the recorded data as shown in figure 3.11(b).

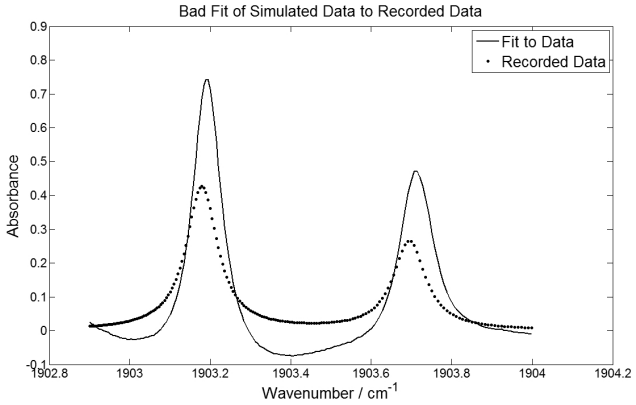

(a) Fit to recorded data at the beginning of a minimisation algorithm. In this case the fit parameters used to generate the background and simulate the spectrum are not correct.

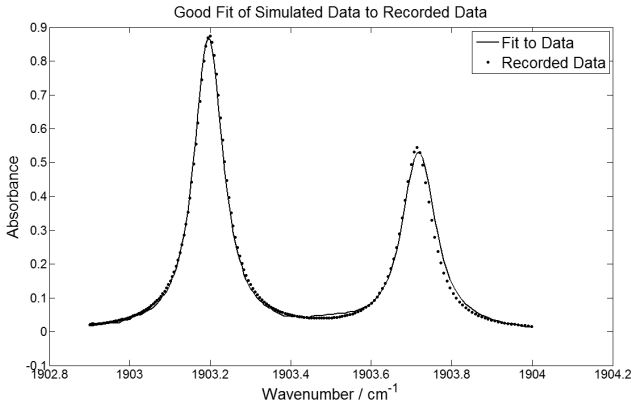

(b) Fit to recorded data towards the end of a minimisation algorithm. The fit parameters are now much closer to the correct values.

Figure 3.11: Two examples of simulated data fitted to measured data from a $5.25\mu m$ QC laser. The absorption lines are caused by the presence of NO.

Gas absorption spectra of this variety has typically been analysed using the Levenberg-Marquardt [12, 13] algorithm. This algorithm has been used to analyse QC laser spectra [14]. Both the Levenberg-Marquardt and Nelder-Mead algorithms are accepted methods of minimising nonlinear problems. The following sections describe the types of minimisation algorithms that were adapted for use in analysing the QC laser spectra and results in the following chapter. There are many other documented optimisation algorithms that would be suitable for use in analysing the data produced by QC lasers, however

3.6.1 Nelder-Mead Algorithm

The Nelder-Mead [15] algorithm is commonly used to perform nonlinear optimisation. It is a numerical method for minimising an objective function over multiple dimensions. The method uses a simplex to assess the solution space. A simplex is a polytope and for a function with N dimensions there are N + 1 vertices in the simplex, for example in two dimensional space a Nelder-Mead simplex is a triangle. The objective function of a typical fitting routine will have 3 to 7 dimensions depending on the number of gases to be detected and the simplex used will have a corresponding number of vertices. In the case of a three dimensional objective function the simplex will be made of four sets of fit parameters and their equivalent function values.

The algorithm moves towards the nearest local minimum of a function when that function varies continuously. The algorithm generates a new set of fit parameters by extrapolating the behavior of the objective function measured for each set of fit parameters. The algorithm then chooses to replace one of the original sets with the new fit parameters and the algorithm continues until it reaches a predefined exit condition. Since each simulation of an absorption spectrum takes time, it is important that the algorithm searches through the solutions efficiently. The Nelder-Mead algorithm does not perform a global search, it finds a local rather than a global minimum. As such it is possible for the algorithm to get trapped in a false local minimum,

this depends entirely on the starting position.

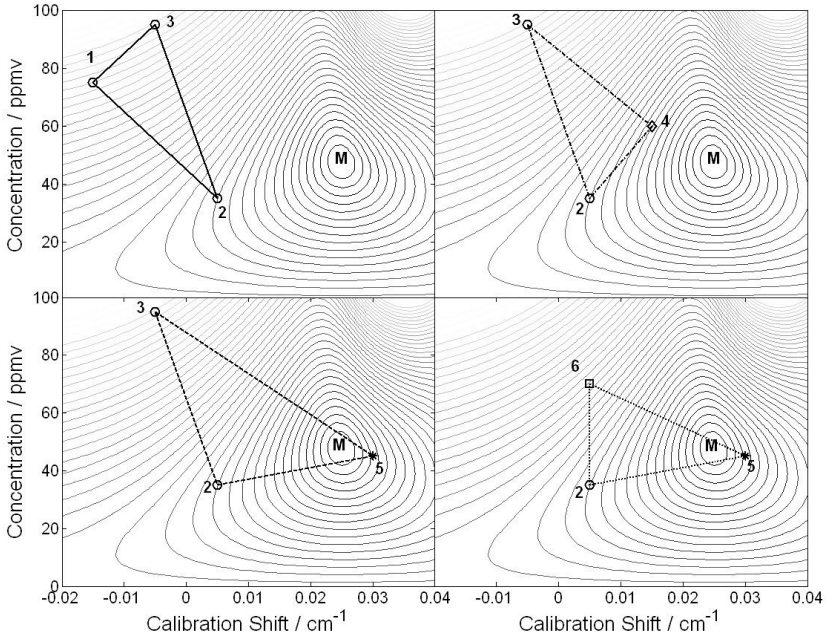

Figure 3.12: The Nelder-Mead algorithm in operation, the contour plots show the surface of an objective function against concentration and linear shift in calibration, the minimum of the function is marked with an *M* symbol. The starting simplex is shown in the top left graph and the first iteration of the algorithm is to reflect the simplex by moving one of the parameter sets from position 1 to position 4 as shown in the top right graph. This results in an improvement so position 4 is extended further to position 5 in the lower left graph. The parameter set shown at position 3 now returns the highest objective function value so the simplex is contracted by moving from position 3 to position 6. This process will continue until certain exit conditions are met. The exit conditions usually consist of a target objective function value or size of change in the parameter set.

The simplest method of updating the simplex is to replace the worst set of fit parameters with a point reflected through the centroid of the remaining N sets. If this set generates a lower function value than any of the other sets of fit parameters, then the algorithm will try stretching exponentially out along this line. However, if the new set does not have a lower value than any of the previous sets, then the function has stepped across a minimum. Now, the algorithm will contract the simplex and move closer to the minimum. This process is shown graphically in figure 3.12, the figure shows how the algorithm

can quickly move towards a local minimum of the objective function.

The algorithm ends when one or all of a predefined set of exit conditions are met. The exit conditions are typically parameters such as a maximum number of objective function evaluations, a minimum size of the simplex or a minimum change in the function value. A variation of the Nelder-Mead algorithm was used to analyse the majority of the data in the following chapters. It was developed largely during the gas sensor testing described in section 4.3 in the following chapter.

3.6.2 Simulated Annealing

Simulated annealing [16], [17] is a global optimisation algorithm, the principle behind the algorithm as well as the name are based on the process of annealing from metallurgy. Annealing is a heat treatment technique that reduces the defects in a metallic material and can therefore increase strength and hardness. Firstly, the material is heated causing the atoms to move from their initial positions. The initial position is analogous to a local minimum of the search space, after heating the atoms are free to move away from this local minimum. The material is then gradually cooled, as this happens the configuration of the atoms begins to set. If the cooling is performed correctly the crystal structure will find a configuration with a lower internal energy.

When this process is translated into a minimisation function, each iteration of the algorithm updates the previous set of fit parameters with a random set. This new set of fit parameters is evaluated and the algorithm must choose which set to use at the next iteration. The decision of which set of fit parameters to keep is based on a probability that depends on the difference between the two function values and on another global parameter. This global parameter represents the temperature of the system and is gradually decreased during the process. At the start of the algorithm, when the temperature is high the fit parameters change in a random fashion with the resultant function value able to increase as well as decrease. As

the temperature is reduced the function value becomes consistently lower because the difference between the function values begins to dominate the decision process. Due to the probabilistic nature of the algorithm increases in the function value are always permitted and so the algorithm is able to move itself out of local minima and is therefore more likely to find a global minimum.

An algorithm based on Simulated Annealing was developed and tested on QC laser data. When configured correctly the fitting routine could produce more accurate and precise results than the Nelder-Mead algorithm. When the algorithm was not configured correctly it would often fail to converge to an acceptable solution. The best configuration of the algorithm was not the same when fitting different gases. Highly blended absorption lines, produced for example by SO_2, required different configurations from more sparse absorption profiles, such as NO. Even when configured correctly the time taken for the algorithm to find a solution was significantly longer than the time taken by the Nelder-Mead algorithm. It is possible that through further development a fitting routine that is based on Simulated Annealing or on a combination of search algorithms will be implemented. However, at the time of writing the best results in terms of accuracy, precision, consistency between gases and speed was obtained through a modified Nelder-Mead algorithm.

3.6.3 Heuristics

The results of the minimisation process are highly dependent on the initial starting position, particularly when using local search algorithms such as the Nelder-Mead algorithm. The accuracy of the results and the speed at which they are found can both be improved by implementing a heuristic that evaluates and improves the initial guess. In some cases it is also possible to avoid the minimisation process entirely. Any minimisation algorithm searches the solution space of the problem in order to find the best fit to the QC laser data. However, it is possible to use a different approach to finding the solution where the QC laser data itself is analysed to obtain the best fit.

A heuristic, expert system or combination of both can be used to increase the speed and accuracy of the analysis. By making intelligent decisions regarding the possible solutions and considering experience based knowledge of the expected inputs it is possible to very quickly calculate an answer from the information that is provided. This is in contrast to continually comparing the output from a model to the information that is provided in an effort to determine the best direction in which to move the current answer.

As a simple example, when the absorption pathlength is known it is possible to mathematically determine the possible range of concentrations that can be attributed to a set of absorption features. The development of heuristics and expert systems is an area that was investigated later in the period of study and as such remains under development. However, the initial results that have been achieved are promising.

3.7 Objective Functions

In a fitting routine a recorded spectrum is compared to various generated spectra to obtain a best fit and hence the concentrations of the gases present. The purpose of the minimisation functions discussed above is to find the best fit, the purpose of an objective function is to compare the recorded data with generated data and score the resulting fit. This comparison and scoring is often complex due to lack of data or interfering factors such as optical noise. The following sections detail some noteworthy objective functions that have been used for data analysis in the remaining chapters.

3.7.1 Background Interpolation

In order to compare a generated spectra with real data obtained from a QC laser it is necessary to convert the raw data obtained from a laser pulse to a transmission or absorbance spectrum, since they have no dependence on the power of the QC laser. This requires that data on the background of the

pulse is available, the background is the pulse in the absence of the absorbing gas.

The use of a beamsplitter placed before the measurement cell allows the background pulse to monitored continuously, however the beam from the measurement and background pulses then experiences a different optical path. This could introduce an error to the calculated transmission spectrum. A background measurement can also be achieved by periodically introducing a vacuum or a zero gas to the measurement cell and then recording the background pulse. However, this method prevents continuous measurements from taking place. Objective functions that have the background data available are discussed in the following sections. When the background is not available it must be estimated either through interpolation or by directly minimising polynomial co-efficients that are used to describe the background in the same manner as the concentration parameters.

One method is to estimate the background using the simulated data, this estimation is then refined by the minimisation function. A background estimation can be calculated using equation 3.13, the $QC\,Laser\,Spectrum$ is the portion of the QC laser pulse used for fitting and $Simulated\,Transmission$ represents data simulated using theoretical models.

$$Background\,Estimation = \frac{QC\,Laser\,Spectrum}{Simulated\,Transmission} \tag{3.13}$$

A transmission spectrum is generated from the parameters provided by the minimisation function and this is then broadly sampled as shown in figure 3.13.

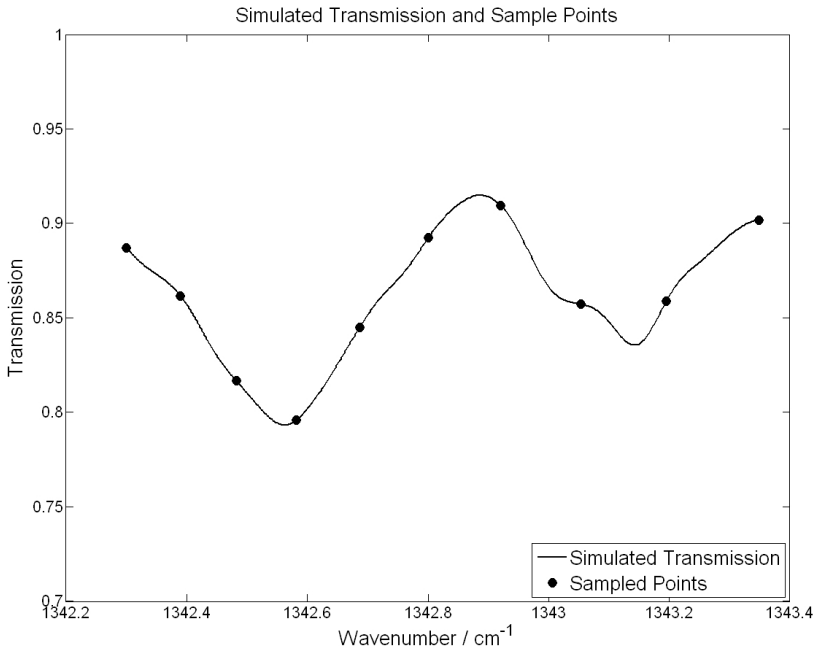

Figure 3.13: The calculation of the background begins by generating a simulated transmission spectrum using parameters that are controlled by the minimisation function. This spectrum is sampled at several points, as is the QC laser pulse data, equation 3.13 is then used to calculate a coarse background over these points. In this case the spectrum above represents an SO_2 absorption.

The sampled transmission is used to obtain a coarse approximation of the background by using equation 3.13. A polynomial fit is then made through the points defined by the coarse approximation and then the polynomial is evaluated over the full wavenumber range, this is shown in figure 3.14.

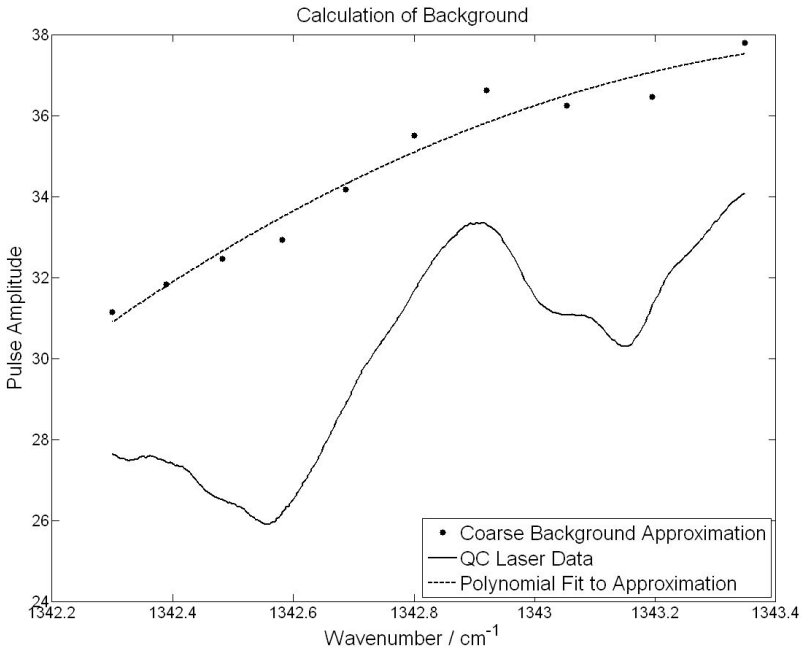

Figure 3.14: The coarse background is used to create a polynomial fit. This polynomial is then evaluated over the entire wavenumber range to create the interpolated background. The QC laser pulse data is also shown for comparison with the generated background.

Once a background has been calculated it can be used to convert the QC laser data to an absorbance spectrum. The quality of the fit is then determined by comparing the real absorbance measurement to the simulated spectrum that was used to calculate the background. This can be seen in figure 3.15, where an example of a fit that has been generated using background interpolation techniques is shown.

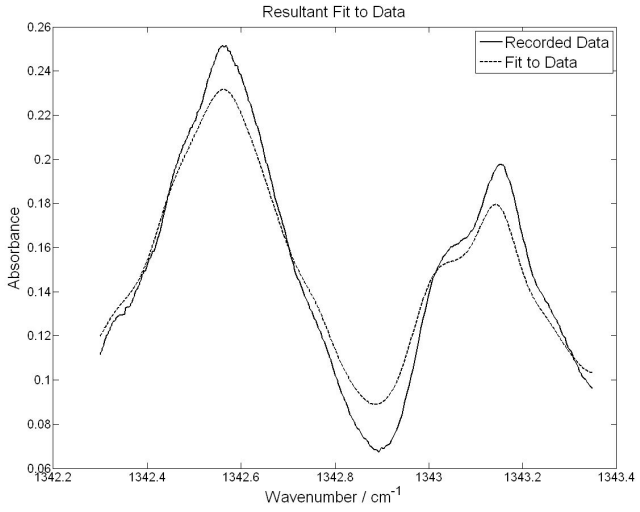

Figure 3.15: The interpolated background can now be used to calculate the absorbance spectrum, this can then be compared to the simulated data that was originally used to find the interpolated background. In this case the fit to the measured data is not optimal, the minimisation function will use this information to find a more accurate fit.

Over time the minimisation function converges towards the set of parameters that allow the objective function to generate an accurate background and the best fit to the QC laser data. This allows the fitting routine to quickly calculate the concentrations of gas present without the need for a normalised QC laser pulse.

3.7.2 Differential Fitting

One of the drawbacks of the background interpolation method described above is that they can only estimate the correct background. This limits the precision of the measurements and often makes low level features with absorptions below 1% difficult to resolve. When a representative QC laser background is available it can be used to calculate a transmission spectrum. This can then be directly compared with a simulated spectrum. Figure 3.16 shows a fit to QC laser data using the background interpolation algorithm.

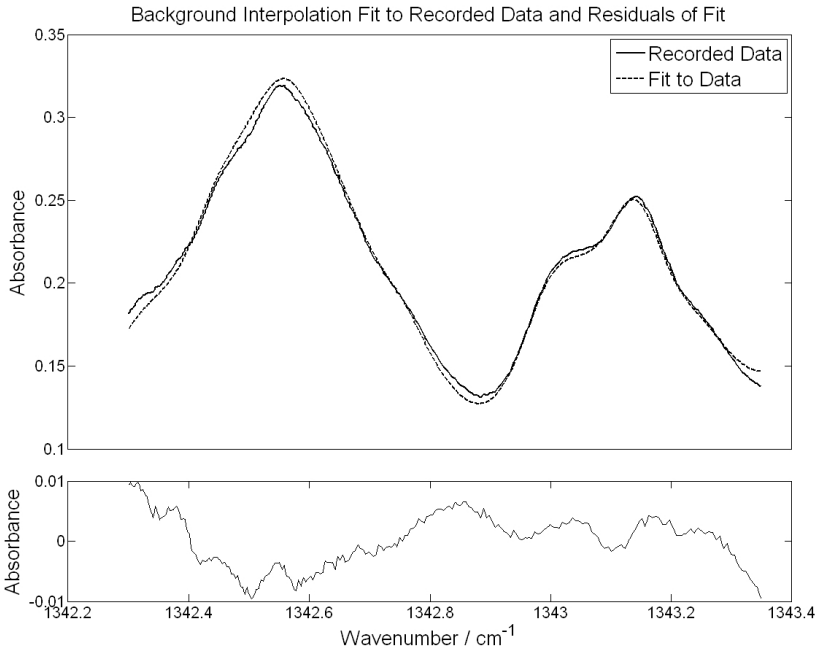

Figure 3.16: This shows a fit to an SO_2 absorption created by a 300ppm concentration and 128cm pathlength. The background used to covert the spectrum to absorbance was interpolated by the fitting routine. In this case the rms value of the residuals is $4x10^{-3}$.

This can be compared to figure 3.17, which shows a fit to the same data when the laser background is available.

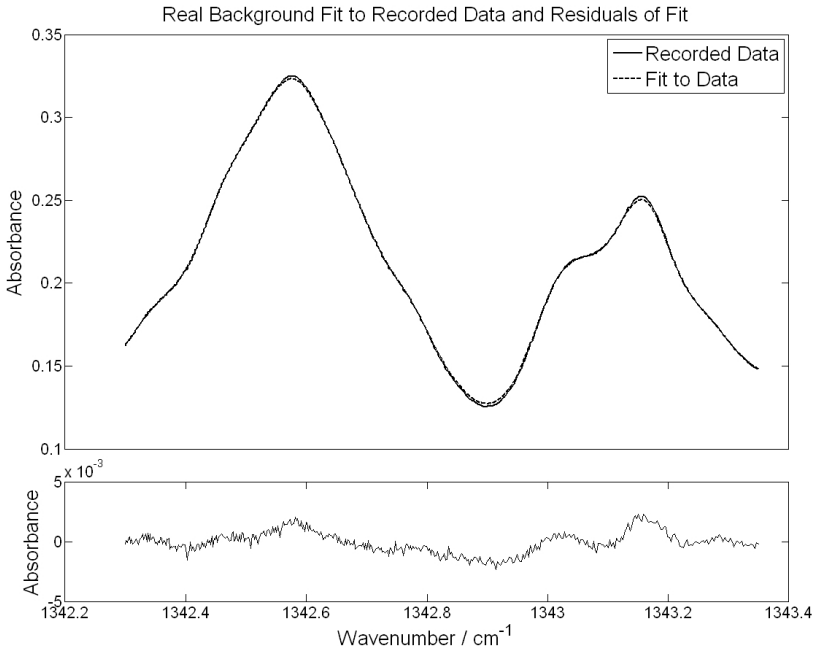

Figure 3.17: A fit to an SO_2 absorption created by a 300ppm concentration and 128cm pathlength. An actual background QC laser pulse was used to covert the spectrum to absorbance. In this case the rms value of the residuals is $8x10^{-4}$.

By taking the rms of the residuals of the fit it is possible to determine the lowest absorption that can be measured with the QC laser. The rms measurements of these fits show that when the background can be used to calculate a transmission spectrum the precision can increase by a factor of 5.

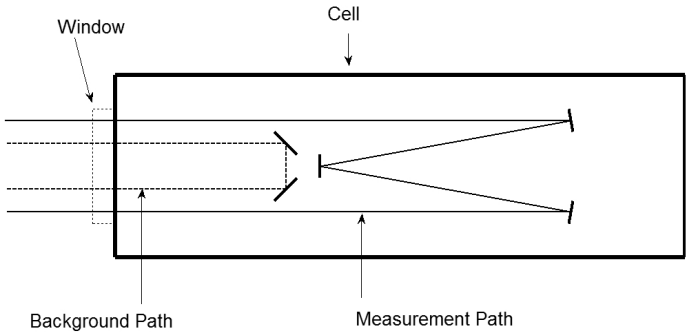

Figure 3.18: A basic layout for a sensor that uses a background measurement. The pathlength over which the absorptions are measured is the difference between the background and measurement pathlengths. In this case the transmittive optics are the same for both paths, this allows any optical fringing effects to be removed through the background division.

It is not necessary when using a real background to ensure that it is free of any absorption features, when a laser measurement that includes absorption from gas is taken and used as the background in a fitting routine the analysis is based on the difference between what is observed on the background and signal measurements. A gas cell as shown in figure 3.18 would include gas absorptions in both the measurement and background paths. Concentration measurements could be made on either of these paths using the background interpolation method. Alternatively, the QC laser pulse obtained from the shorter path could be used as a background measurement for the longer path. The pathlength used to simulate spectra in this case would be the difference between the short and long path.

3.7.3 Multiple Gas Fitting

Under laboratory conditions it is possible to conduct studies on an isolated species. However in more practical conditions such as environmental or emis-

sion measurements there is usually a variety of gases present in the medium. When other gases are present they can interfere with the principle measurements. One of the ways that this presents itself is in the overlap of absorption spectra. In some cases it is also convenient to use a single QC laser to measure multiple gases. Figure 3.19 shows a transmission spectrum with contributions from three gases.

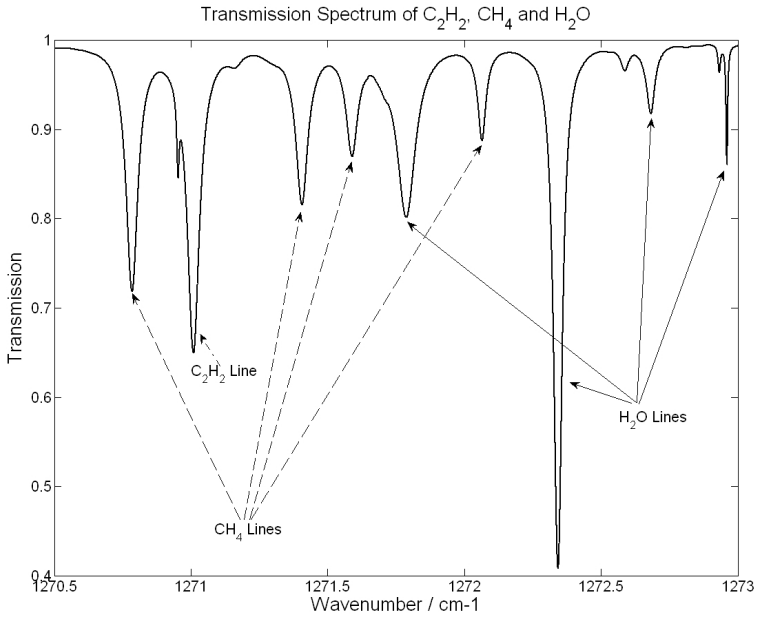

Figure 3.19: A transmission spectrum showing absorption line contributions from multiple gases. The gas mix is at a pressure of $500Torr$, a temperature of $300°C$ and has a pathlength of $1m$. The gases present are $500ppmv$ of C_2H_2, $1000ppmv$ of CH_4 and 1% of H_2O.

The interference can be overcome by recording data in a region where absorption lines from other gases is limited. This is not always possible and sometimes it is necessary to analyse more than one gas per QC laser. If a background QC laser pulse is available the three gases can be fitted separately in a step by step process. If, however, a background interpolation method is required due to the absence of a background pulse, the gases must be fitted simultaneously. Since the number of fit parameters increases with additional gases the minimisation function used must be allowed more iterations to

find a minimum. Figure 3.20 shows a background interpolation fit to the spectrum shown in figure 3.19.

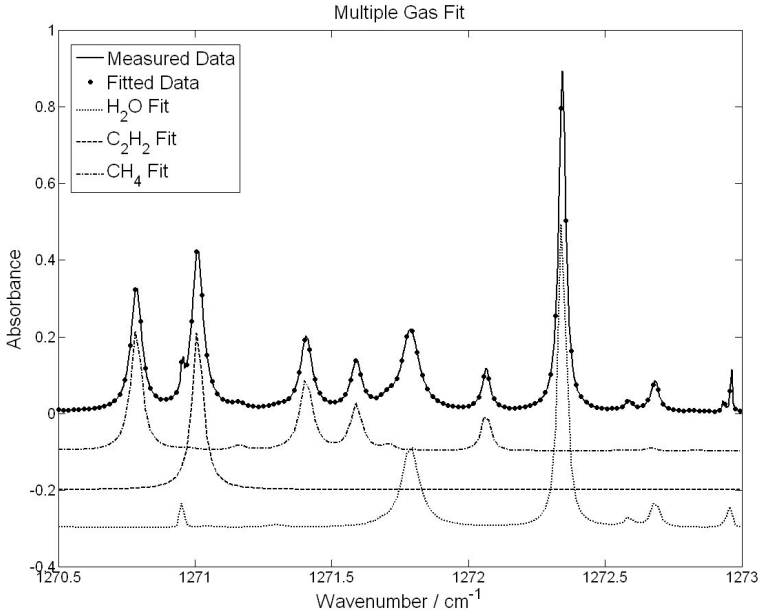

Figure 3.20: The resultant fit to the measured data has components from all three gases. The individual fits from each of the gases are also displayed but have been offset for clarity.

The time taken to reach an acceptable fit when simulating multiple gases can have an adverse effect on the response of the sensor. The inclusion of multiple gases also increases the number of local minima that are present in the search space, meaning that it is often possible for the minimisation function to become trapped in a local minimum. In these cases it is necessary to add additional analysis to the fitting routine to diagnose when this has happened and take measures to correct the fault.

Problems can also arise when one of the gases falls to a level which cannot be detected by the sensor. In this case it becomes easier for the minimisation function to become trapped in a local minimum. This occurs because the fitting routine can try to fit an absorption line from the absent gas to an absorption line from one of the gases that is still present. If the min-

imisation function used is a global search algorithm then this error should be corrected during normal operation of the algorithm, assuming that the routine is allowed to run for a long enough period of time. However if a local search algorithm is used then additional functionality must be incorporated to detect when such problems arise. When this happens the minimisation function must be restarted with a new initial guess.

When possible it is preferential to fit a single gas per QC laser. In cases where this is not possible multiple gas fitting can be used. However, further development is necessary to implement a robust solution particularly in the absence of a laser background measurement.

3.7.4 Gamma Air Fitting

When there are multiple gases present the other gases can affect the measurement of the principal gas even when there is no absorption line coincidence. One of the ways this interference takes place is by collisional broadening of absorption lines. When changes in the gas mix occur that are not directly related to the principal gas the γ_{air} component of the absorption lineshape is subject to change. The effect of changing the γ_{air} value in a simulation of CO_2 is shown in figure 3.21.

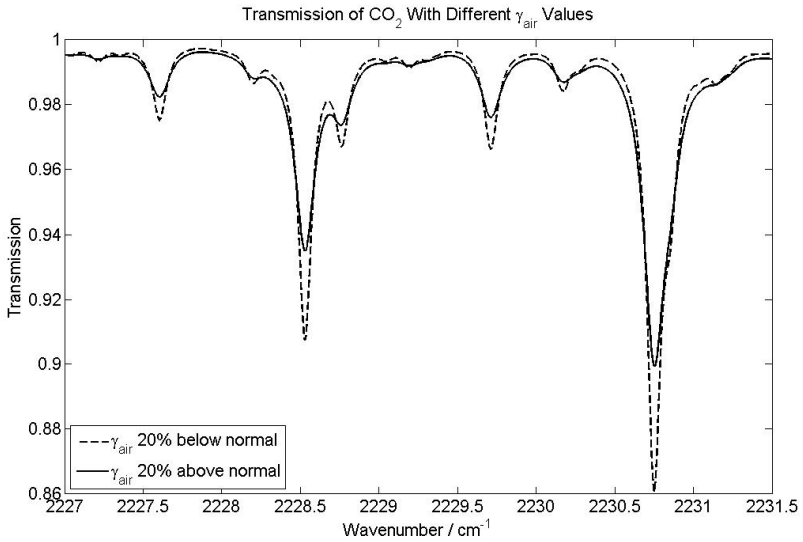

Figure 3.21: This shows a transmission spectrum of CO_2 at a concentration of 2% over a pathlength of 1m under atmospheric temperature and pressure. The difference between the two plots lies in the change of γ_{air} which can occur when the concentrations of the other gases in the mix are altered.

Even when all components of a gas mix are being monitored the necessary data required to compute a correct γ_{air} value is rarely available. During the operation of a gas sensor the components of the gas mix under study will change, this means that the γ_{air} values will change accordingly. To maintain accurate concentration retrieval it is often necessary to include a method of fitting the γ_{air} values. When the two spectra shown in figure 3.21 are analysed with a fitting routine that includes a γ_{air} adjustment method the returned concentration will be the same. The effect of increasing γ_{air} changes an absorption spectra in a similar manner to a pressure increase coupled with a concentration decrease as shown in figure 3.22, for this reason it is important that the pressure measurement be accurate and reliable.

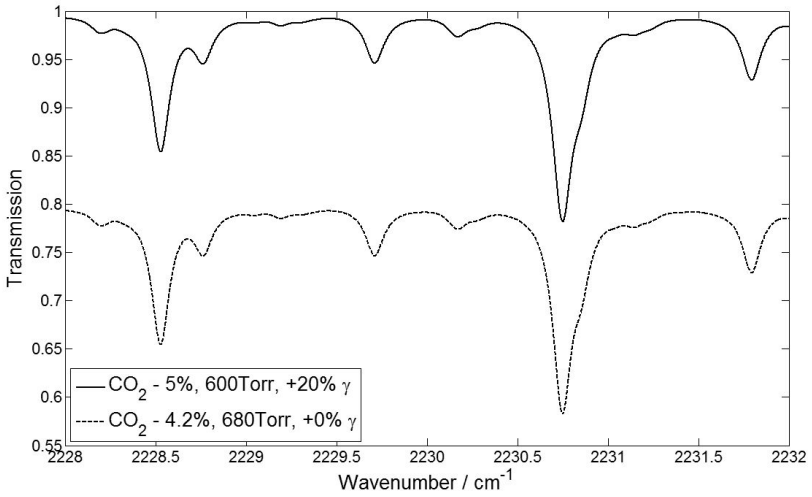

Figure 3.22: Two offset CO_2 transmission spectra with a 1m pathlength at $20°C$. One spectrum shows a concentration of 4.2% at 680Torr with no γ_{air} change, the other shows a concentration of 5% at 600Torr with a 20% increase in γ_{air}.

3.7.5 Fringe Detection and Removal

One of the major weaknesses of gas measurement using QC lasers is their susceptibility to optical fringing [18, 19]. Optical fringing is caused by constructive and destructive interference between different beam paths from typically the same laser source, however this is not a requirement. Most transmissive optics also reflect a certain proportion of light, this proportion is dependant on the optical material, the wavelength of light, any coatings on the optic, the angle of incidence, etc. This can lead to light from a single source taking different optical paths to the detector. Fringing can appear on a laser pulse and disrupt the spectra that are generated, 3.23 shows an example of an optical path that can lead to fringing.

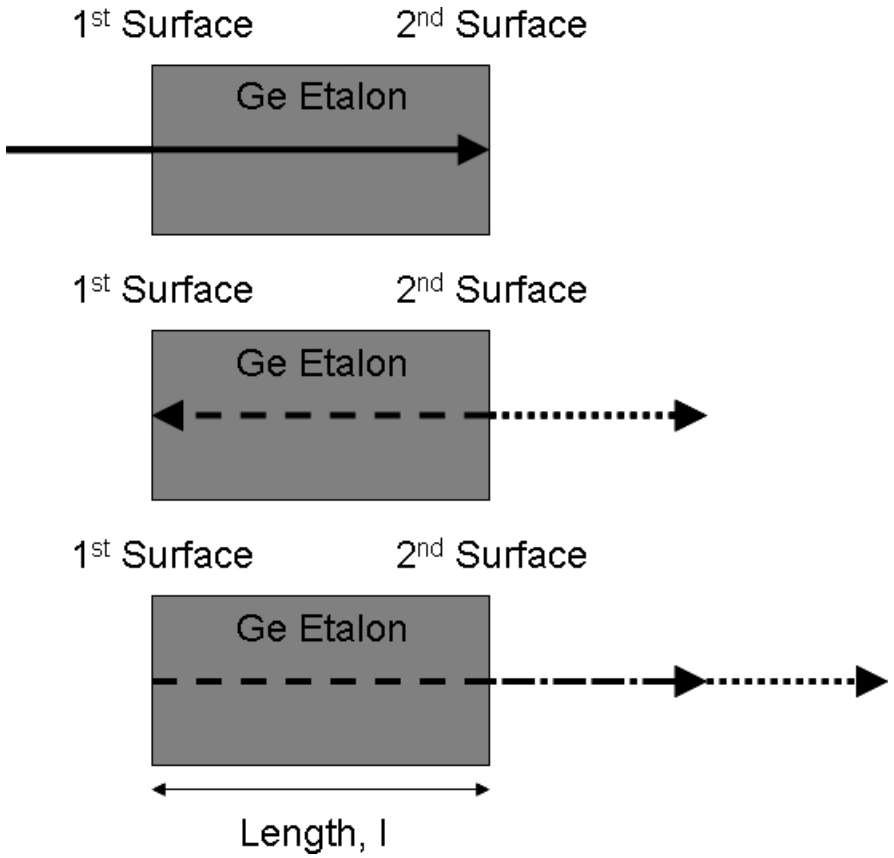

Figure 3.23: This shows an example of how optical fringing can be created. A Germanium etalon is placed in the path of a beam, when the beam reaches the second surface the beam is split into two components. One component exits the etalon and the other is reflected back into the etalon towards the first surface. Some of the component that is reflected will reflect off the first surface and again reach the second surface, at this point some of the light will exit the etalon and continue along the same path as the first component.

The effect that an optical element such as the germanium etalon shown in the diagram above has on a QC laser pulse is shown below in 3.24.

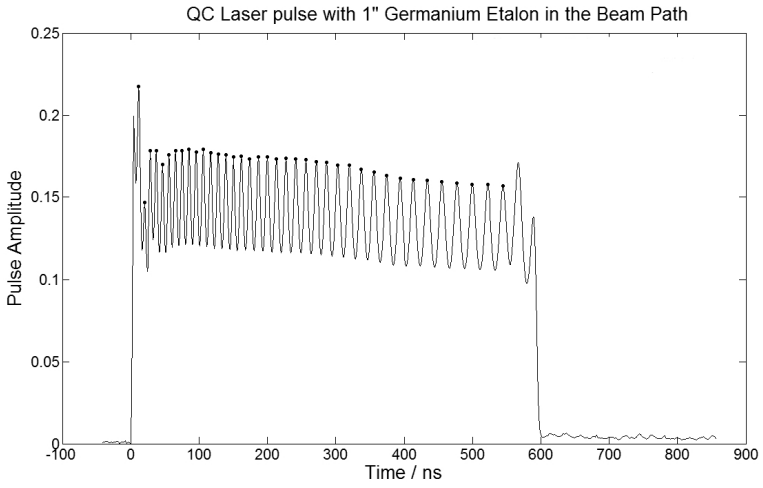

Figure 3.24: This shows an example of how optical fringing can appear on a QC laser pulse. A Germanium etalon is placed in the path of a beam, this results in a series of peaks which appear on the laser pulse.

There are optical design measures that can be taken to minimise fringing such as the use of wedged windows, this prevents optical interference from taking place. However, it is not always possible to completely remove all possible causes of interference. Also, as the sensitivity requirements of a sensor increase the quality of the measured data becomes more important. An algorithm that can interpret the presence of fringing correctly and not as an absorption created by gas is advantageous.

Spectra recorded at Rutherford Appleton Laboratory (RAL) with a high resolution Fourier Transform Spectrometer (FTS) were found to suffer from optical fringing. The fringing was caused by an air gap between two flat windows in an absorption cell. Figure 3.25 shows the fringing on a spectrum of NO.

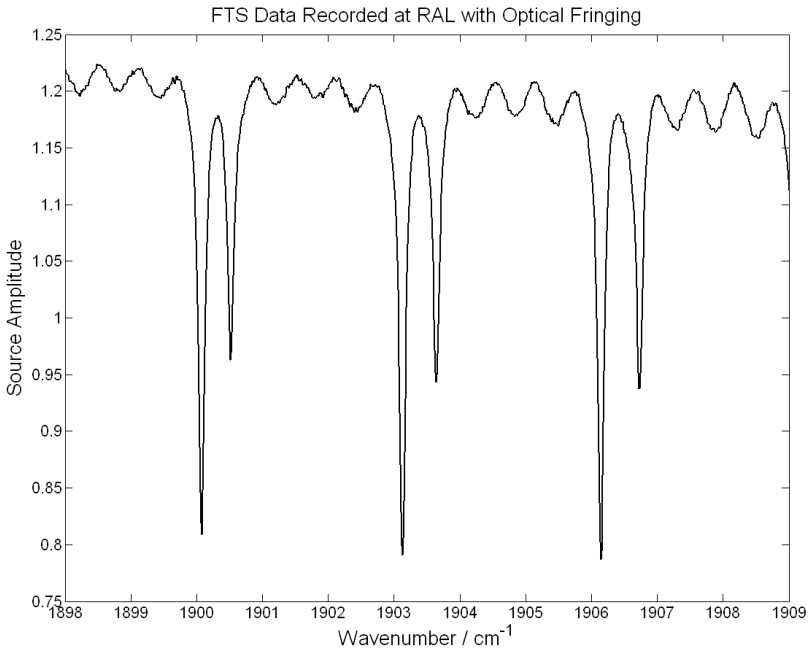

Figure 3.25: A 3000 ppmv *NO* spectrum recorded from an FTS at the Molecular Spectroscopy Facility at RAL. It shows optical fringing caused by light interference over a distance of 8mm between the inner and outer jacket windows on an absorption cell. The internal pathlength of the cell was 8cm.

This can be compared with a simulated transmission spectrum of the *NO* without the fringes, this is shown in figure 3.26.

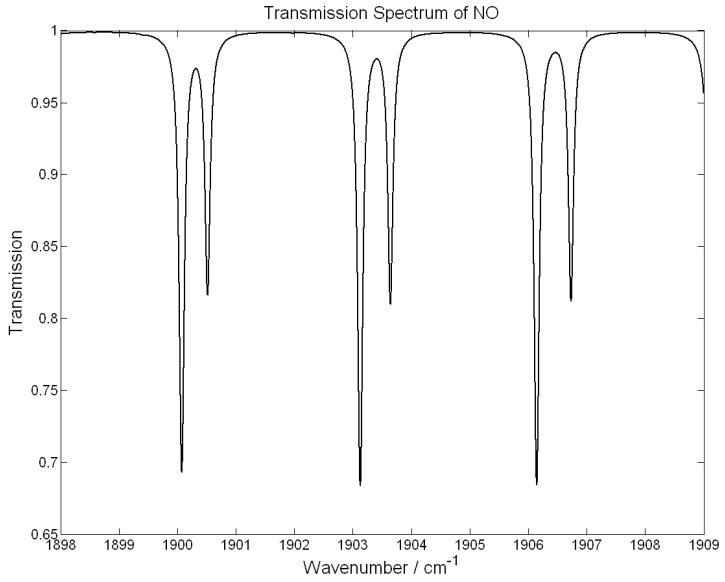

Figure 3.26: A simulated transmission spectrum of 3000 ppmv of NO over a distance of 8cm, this shows the NO spectrum with no optical fringing.

An effective method of removing fringing from spectra would increase the accuracy and robustness of a fitting routine by removing the negative effects of optical fringing. A method of detecting the presence of optical fringing and then removing it from spectra by generating simulated fringing was developed. This was then integrated into the objective function of a fitting routine. Every time the minimisation function performs an iteration and the objective function generates a fit to the absorption lines the residuals of the fit are used to determine the presence of any fringing. If there is any present a fast fourier transform (FFT) is performed to determine the free spectral range (FSR) of the fringing. This is then used to generate a second fit, one that matches a simulated fringe pattern to the residuals generated by the first fit. The function minimum is then computed from the residuals generated by the second fit. The analysis of the fringing is improved as the fit gets better, and as such the fringing becomes easier to remove and the function value is reduced further. This allows the minimisation function to search for the best fit without being disturbed by the optical fringing. Figure 3.27 shows a fit to the RAL data generated by this fitting routine. The Free

Spectral Range (FSR) of the fringing on the data recorded at RAL was shown to match the 8mm spacing of the windows through the relationship in equation 3.14, where n is the refractive index and l is the distance.

$$l = \frac{1}{2nFSR} \tag{3.14}$$

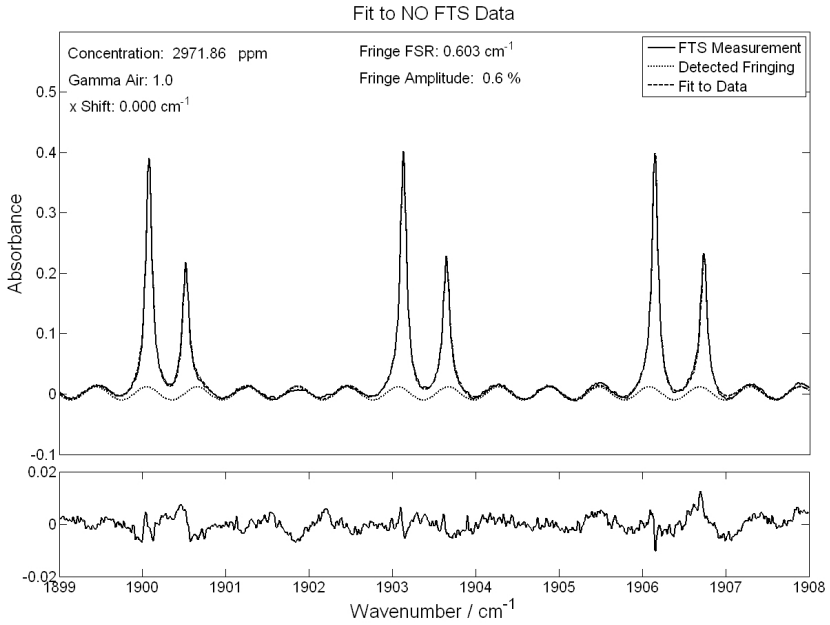

Figure 3.27: The 3000 ppmv *NO* spectrum recorded at RAL is fitted with a routine capable of fringe detection and removal. The resultant fit shows that the FSR of the fringes matches the 8mm gap between the outer and inner jacket windows of the absorption cell.

3.7.6 Temperature Measurement

Individual absorption lines respond differently to changes in temperature, because of this it is possible to measure the temperature of a gas mix that is being studied by comparing the relative strengths of multiple absorptions. Normally the temperature is measured and incorporated into the simulation of spectra, however there are cases where such measurements are not possible.

Temperature can be included as a fitting parameter that is controlled by a minimisation function which is trying to find the best fit. An example of the effect of temperature on absorbance is shown in figure 3.28.

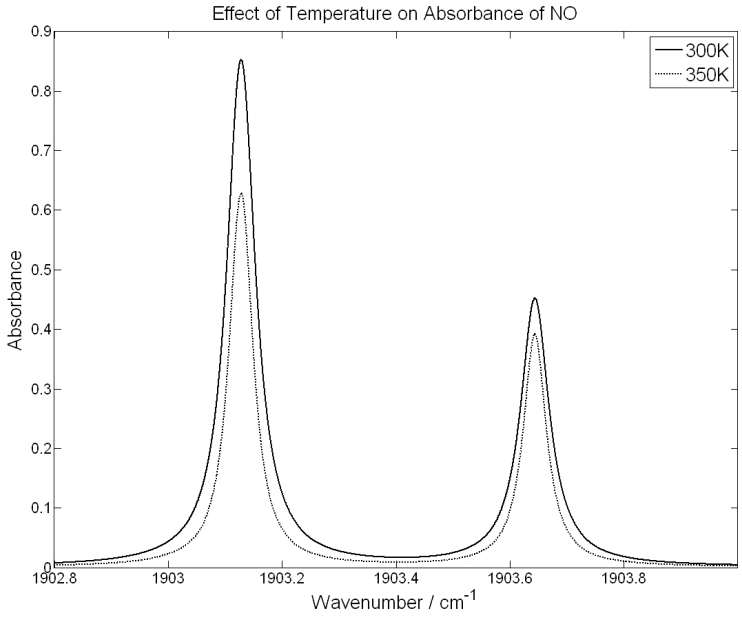

Figure 3.28: This plot shows two NO absorbance spectra, the only difference between the two is the temperature of the gas. As the ratio between the two absorption lines changes with temperature, it may be included as an independent fitting parameter. This is only possible in cases where a ratio between multiple absorption lines can be monitored.

While the temperature does contribute to the broadening of an absorption line, the dominant effect is a change in the strength of the line. This means that when a change in temperature is applied to a single absorption line the resulting effect is very similar to a change in concentration. For this reason temperature fitting is only effective in cases where the ratios between multiple absorption lines can be monitored.

This method of fitting was used to obtain both concentration and temperature measurements of low pressure flames at the University of Bielefeld, Germany. In this case measurements were made with a single $7.8\mu m$ QC laser. Due to the low pressure and composition of the chemical reactions and

exhaust produced by the flames, profiles of CH_4, H_2O and C_2H_2 could be recorded. The large number of CH_4 absorption lines provided ideal conditions for including the temperature as a fit parameter. These experiments are the basis for section 4.5 in the following chapter.

3.8 Conclusions

The electronic requirements, theory and analytical methods used to detect and monitor gases have been discussed. These methods allow data to be recorded that is suitable for analysis using the spectral simulation and fitting algorithms developed and discussed in this chapter. The algorithms were used to analyse the data presented in the following chapter and allowed the development of an exhaust gas sensor.

The analysis algorithms consist of two significant parts. Firstly, the minimisation algorithms used to find the best fit to the data provided to the fitting routine. The selected analysis algorithms included a modified Nelder-Mead algorithm and a simulated annealing algorithm.

References

[1] Vigo Systems S.A., 129/133 Poznanska Street, 05-850 Ozarow Mazowiecki, Poland, www.vigo.com.pl

[2] Kolmar Technologies 3 Henry Graf Rd. 9 Newburyport, MA 01950 USA, www.kolmartech.com

[3] Cascade Technologies Ltd. Glendevon House, Castle Business Park, FK9 4TZ, Stirling, UK, www.cascade-technologies.com

[4] Agilent Technologies Ltd. www.home.agilent.com

[5] L.S. Rothman *et al*, *"The HITRAN 2004 molecular spectroscopic database"*, Journal of Quantitative Spectroscopy & Radiative Transfer **96**, 139204 (2005)

[6] R. A. McClatchey, W. S. Benedict, S. A. Clough, D. E. Burch, R. F. Calfee, K. Fox, L. S. Rothman and J. S. Garing, *"AFCRL Atmospheric Absorption Line Parameters Compilation"*, AFCRL-TR-0096 (AFCRL, Bedford, MA, 1973).

[7] N. Jacquinet-Husson *et al*, *"The GEISA spectroscopic database: Current and future archive for Earth and planetary atmosphere studies"*, Journal of Quantitative Spectroscopy & Radiative Transfer **109**, 10431059 (2008)

[8] L.S. Rothman *et al*, *"HITEMP, the high-temperature molecular spectroscopic database"*, Journal of Quantitative Spectroscopy & Radiative Transfer **111**, 2139-2150 (2010)

[9] J. Humlicek, *"An efficient method for evaluation of the complex probability function: the Voigt function and its derivatives"*, J. Quant. Spec. Radiat. Trans., **21**, 309-314, (1979)

[10] R. Bracewell *"The Fourier Transform and Its Applications"*, McGraw-Hill, New York, (1965)

[11] M.T. McCulloch, E.L. Normand, N. Langford, and G. Duxbury *"Highly sensitive detection of trace gases using the time-resolved frequency downchirp from pulsed quantum-cascade lasers"*, JOSA B **20** (8), 1761-1768 (2003)

[12] K. Levenberg, *" Method for the Solution of Certain Non-Linear Problems in Least Squares"* The Quarterly of Applied Mathematics 2: 164168, (1944)

[13] D. Marquardt, *"An Algorithm for Least-Squares Estimation of Nonlinear Parameters"*, SIAM Journal on Applied Mathematics 11: 431441, (1963)

[14] J.B. McManus, D.D. Nelson, J.H. Shorter, R. Jimenez, S. Herndon, S. Saleska and M. Zahniser, *"A high precision pulsed quantum cascade laser spectrometer for measurements of stable isotopes of carbon dioxide"*, J. Modern Optics **52** 16, 23092321, (2005)

[15] J.A. Nelder and R. Mead, *"A Simplex Method for Function Minimization"*, The Computer Journal **7**, 308313 (1965)

[16] S. Kirkpatrick, C.D. Gelatt and M.P. Vecchi, *"Optimization by Simulated Annealing"*, Science **220** 4598, 671680 (1983)

[17] V. Cerny, *"A Thermodynamical Approach to the Travelling Salesman Problem: An Efficient Simulation Algorithm"*, Journal of Optimization Theory and Applications **45**, 4151 (1985)

[18] H. D. Young, *"University Physics"*, 8th Edition, Addison-Wesley., (1992), ISBN 0201529815

[19] Lipson, S.G.; Lipson, H.; Tannhauser, D.S., *"Optical Physics"*, 3rd Edition, London: Cambridge U.P., (1995), ISBN 0521069262

Chapter 4

High Temperature Gas Spectroscopy

4.1 Overview

The result of the sensor development described in the previous chapters has been applied to and was driven by a number of applications and spectroscopic research. Four of these are presented in detail in sections 4.2, 4.3, 4.4 and 4.5. The first of these sections describes an internal test and validation of the HITRAN database and the spectroscopic model used to simulate absorption spectra. Section 4.3 details the testing and certification of a prototype sensor, specifically the spectral fitting routines. The development of these are discussed in sections 3.6 and 3.7 of the previous chapter.

The third section describes a series of product trials based on the development described in chapters 2 and 3. This product was a marine based gas sensor designed to monitor ship emissions, a number of designs were trialled and these are discussed. Finally, many of the principles described in chapters 2 and 3 are applied to the spectroscopic study of low-pressure flames. This section demonstrates the versatility of QC lasers in spectroscopic research.

4.1.1 Gases and Cross-Interference

There are many gases that can be detected and measured using QC laser technology, however accurate detection and concentration retrieval depends on the quality of the measurements taken and upon accurate absorption line information. There are a number of spectral databases that are available containing information about absorption lines. The information contained within them is usually a collection of studies performed by independent research groups as discussed in section 3.4, the databases are composed of theoretical calculations and experimental measurements. As such the coverage and accuracy of the information stored in this database is often irregular. Some experimental data was recorded using a high resolution fourier transform spectrometer (FTS) of some common gases at typical temperatures and pressures for atmospheric and exhaust conditions. This data was compared with similar spectra generated from spectral simulations that used the HITRAN database as a source of absorption line data. The results of these experiments are presented in section 4.2.

Cross-interference exists when the presence of secondary gases alters the spectra of the gas being measured. This can occur in two ways, the first and most obvious occurs when a secondary gas has absorption lines in the region where the primary gas is being measured. An example of this effect is shown in figure 4.1 with a combined H_2O and SO_2 spectra. The H_2O completely absorbs the light in certain places while in others it significantly alters the SO_2 spectrum.

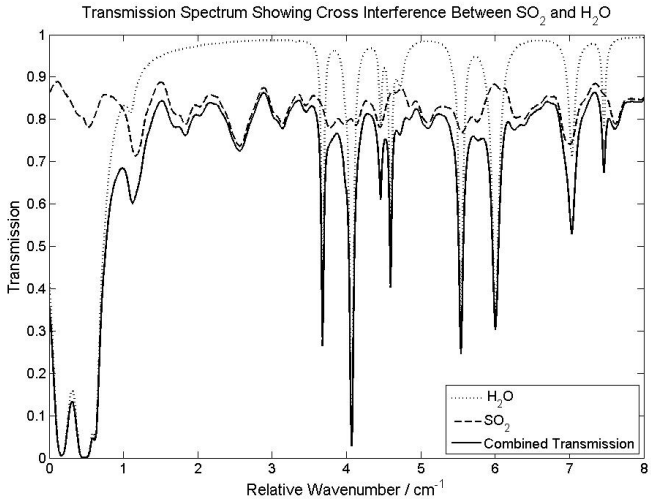

(a) Transmission spectrum of SO_2 and H_2O. The H_2O lines cause difficulty in measuring the SO_2.

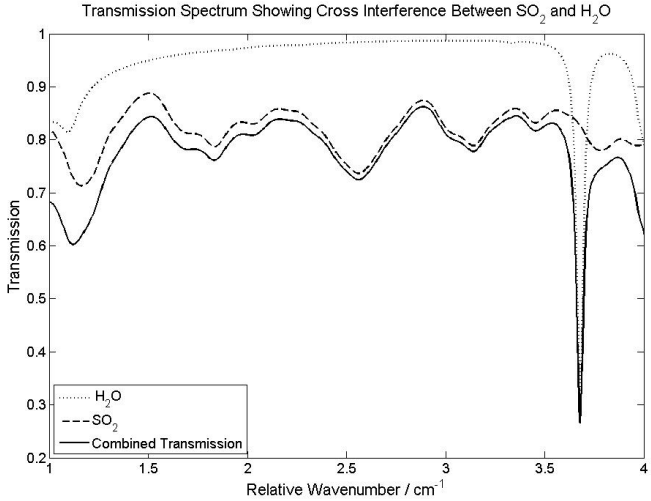

(b) Transmission spectrum of SO_2 and H_2O. In this wavenumber range there is window in the H_2O spectrum which can be used to measure the SO_2.

Figure 4.1: Transmission spectra of $400ppmv$ SO_2 and 3% H_2O over a pathlength of $1.28m$ at $300°C$. The presence of H_2O limits the wavenumber range that can be used to accurately measure SO_2.

A more subtle cross-interference effect arises from the collisional broadening of absorption lines, secondary gases can alter the line-width of other absorption lines. This effect must then be accounted for in order to accurately interpret the data. An example of this effect is shown in figure 4.2 with CO_2 spectra with different cross-interference conditions leading to different gamma air values.

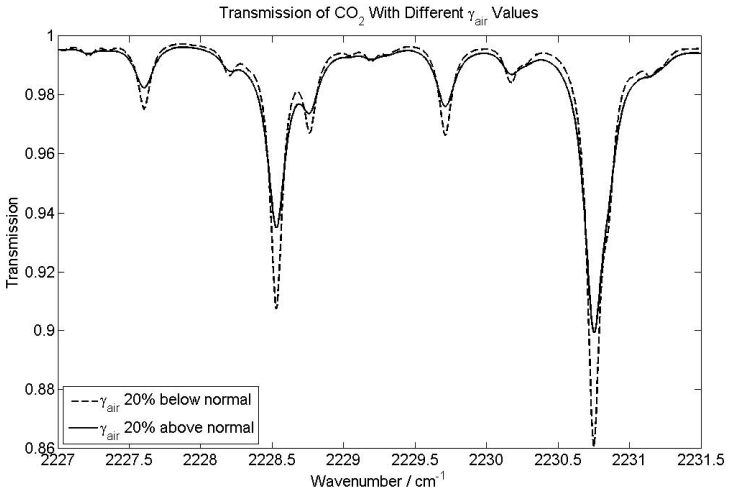

Figure 4.2: This shows a transmission spectrum of CO_2 at a concentration of 2% over a pathlength of 1m under atmospheric temperature and pressure. The difference between the two plots lies in the change of γ_{air} which can occur when the concentrations of the other gases in the mix are altered.

The effects of cross-interference can be accounted for with prior knowledge of the secondary gases that are present. Under conditions where this information is not available, the effects can be compensated for during analysis by allowing the relevant parameters to be minimised. The introduction of techniques to compensate for cross-interference effects was largely as a result of the experimental work carried out in section 4.3 where a number of tests were performed that evaluated the sensor's sensitivity to cross-interference. The methodology behind these techniques is presented in section 3.7.

4.2 RAL FTS Spectra

High resolution spectra were obtained of NO, NO_2 and SO_2 using a Bruker IFS125 fourier transform spectrometer (FTS). These experiments were conducted at the Molecular Spectroscopy Facility (MSF) [1] which is a department of Rutherford Appleton Laboratory (RAL). The purpose of these experiments was to verify the line strength and broadening data of these gases with varying temperature and pressure. The resulting FTS spectra are compared with the equivalent HITRAN [2] simulations in section 4.2.2. The aim of these particular experiments was not to improve on the data available in HITRAN, but to provide verification that the data was suitable for use in the simulation of spectra to fit to QC laser data.

4.2.1 Fourier Transform Spectrometer

This section describes the experimental setup used and some of the theory behind an FTS. Infrared light from a broadband source was passed through a cell containing the species under study and was then analysed by an FTS. The temperature and pressure of the gas within the cell was controlled, allowing high resolution spectra to be recorded at a variety of temperatures and pressures. A representation of the experimental setup is shown in figure 4.3.

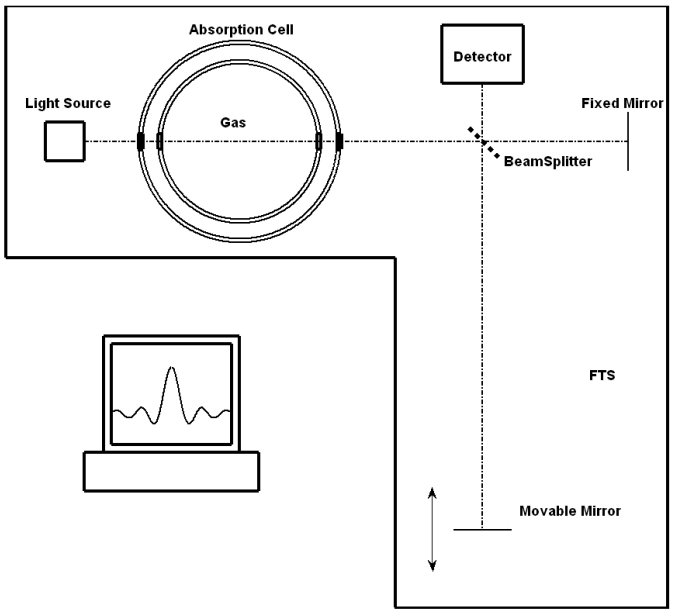

Figure 4.3: This shows the experimental setup used to perform infrared measurements of NO, NO_2 and SO_2. The FTS includes space for a heated absorption cell which includes an outer jacket to allow the cell to be removed without disturbing the rest of the instrument. The critical components of the FTS are the broadband light source, the detector, the beam splitter and the movable mirror.

The FTS is similar to the Michelson interferometer, a beam of light is split into two using a beamsplitter. One beam reflects off a fixed mirror and returns the beam to the beamsplitter. The other beam reflects off a second mirror which also returns the beam to the beamsplitter. The second mirror can be moved parallel to the direction of propagation allowing the optical path difference between the two paths to be changed. The resulting path difference leads to constructive and destructive interference allowing an interferogram to be recorded by the detector. A fourier transform of the interferogram allows a spectrum to be extracted. The FTS was configured to a resolution of 0.03 cm^{-1}.

4.2.2 Comparison of FTS and Simulated Spectra

The FTS spectra recorded at RAL were of NO, NO_2 and SO_2, they were recorded at a variety of temperatures and pressures as shown in table 4.1. Each measurement had a corresponding background measurement to allow the spectra to be converted to transmission to aid the analysis. The temperature was varied since the response of the gas to changes in temperature needed to be verified. The pressure was varied to verify the broadening data in the latest iteration of the HITRAN database.

Gas	Concentration / ppmv	Pressure / Torr	Temperature / $°C$
NO	0, 3000	710, 600, 400, 300	60, 120, 180
NO_2	0, 1000	710, 600, 500, 400, 300	60, 90, 120, 150, 180
SO_2	0, 1000	710, 600, 500, 400, 300	60, 90, 120, 150, 180

Table 4.1: A list of FTS measurements performed at the Molecular Spectroscopy Facility. The accuracy of the gas samples was ±2%

A heated, single-pass gas cell was used to control the temperature and pressure of the gas while mounted within the FTS. A schematic of the absorption cell is shown if figure 4.4. The optical system consisted of a single pass through the cell, two sets of two wedged calcium fluoride windows isolated the cell from the surrounding environment and allowed the pressure within the cell to be varied. The gas samples were introduced to the heated cell through a short heated line, the temperature of which was set to match the cell temperature of the particular measurement taking place. Background measurements were taken before and after each sample measurement and were achieved by pumping the cell down to remove any trace of the sample gases.

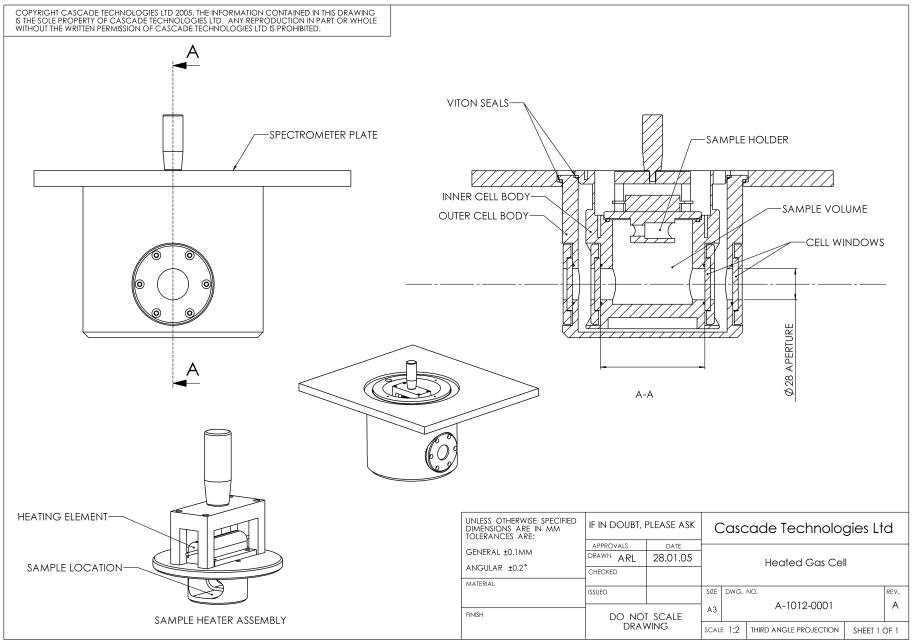

Figure 4.4: This shows the heated, single-pass gas cell. Gas can be delivered to the cell by means of compression fittings on the lid of the cell. A heating element on the lid and cartridge heaters embedded within the inner jacket allows the temperature of the cell to be controlled.

The majority of the FTS data collected included optical fringing, the free spectral range of this fringing was later matched to the distance between the heated sample cell windows. This fringing led to the development of the fringe removal technique discussed in section 3.7.5. Figure 4.5 shows a plot of a raw NO measurement and a background measurement, both spectra exhibit optical fringing.

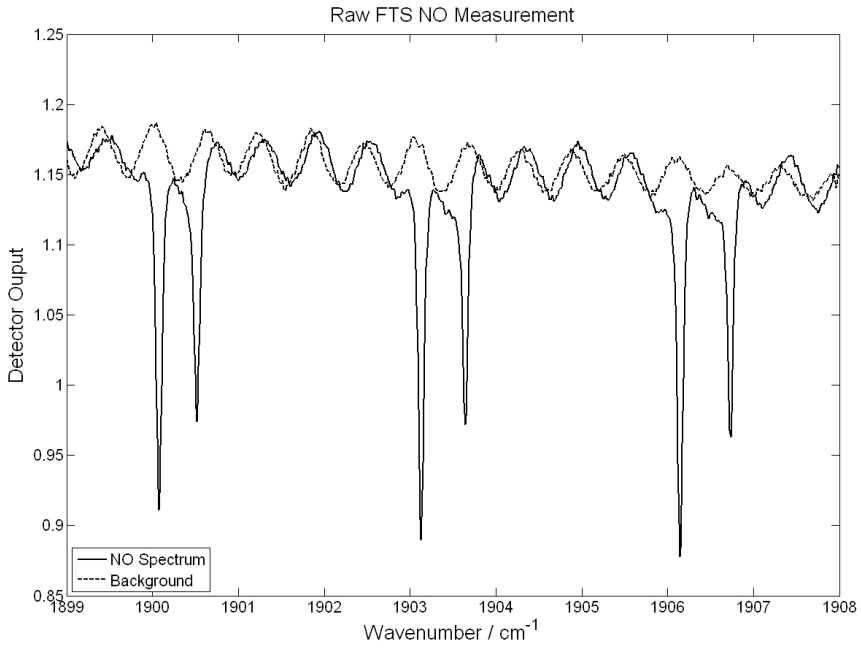

Figure 4.5: This shows a section of a FTS measurement of 3000 *ppm* NO at 180 $^{\circ}C$ and 800 $mBar$ over a pathlength of 9 cm. A background measurement is also shown, both spectra show optical fringing generated by the double window on the absorption cell.

The fringing presented a number of problems with the data analysis and meant that the fringing had to be removed from the spectra. The NO measurements had the fringing successfully removed, however, there was little useful data recovered from the NO_2 measurements and none from the SO_2 measurements. This was because the absorption of light by SO_2 was less than either NO due to the concentration of SO_2 that was used. The blended nature of the SO_2 and NO_2 absorption lines together with the short path through the gas, meant that the optical fringing had a greater interference effect. The fringe removal technique is applied to the NO measurement in figure 4.6, this results in a usable spectrum.

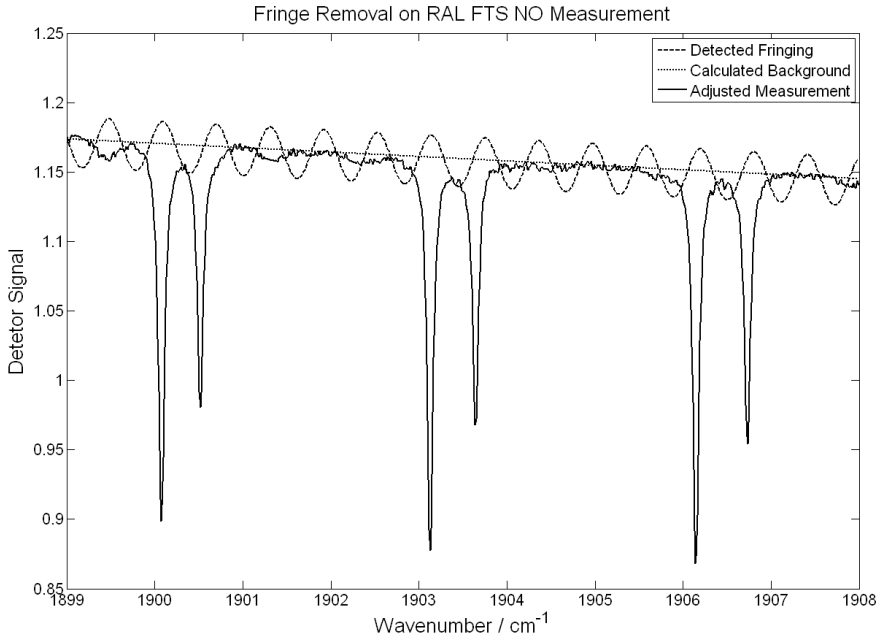

Figure 4.6: This shows a section of a FTS measurement of 3000 *ppm NO* at 180 $^{\circ}C$ and 800 *mBar* over a pathlength of 8 *cm*. This data has had optical fringing generated by the absorption cell removed by a software algorithm. The background generated by the algorithm and the calculated fringing are also shown.

Results

An example of a raw *NO* spectrum that has had a fringe detection algorithm applied to remove the optical fringing is shown in figure 4.7. This method of fringe removal was applied to the raw data before any further analysis took place.

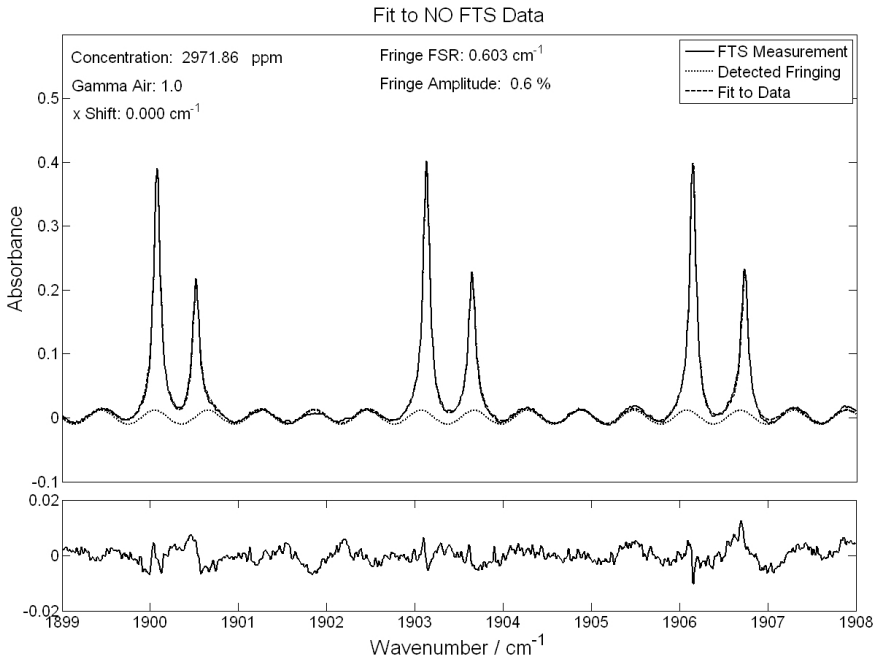

Figure 4.7: This shows a raw NO measurement displayed in absorbance with a simulation of the detected fringing and a fit to the resulting data that includes the simulated fringing. The FSR of the optical fringing is found to be 0.603 cm^{-1}, this is equivalent to the 8 mm gap between the outer and inner jacket windows of the absorption cell. The simulated fringing is subtracted from the raw data before analysis takes place.

The NO measurements recorded by the FTS are compared with spectral simulations which are based on the HITRAN absorption line database. The wavenumber resolution of the FTS was set at 0.03 cm^{-1}, for this reason the simulations were re-sampled with this resolution in order to provide a more effective comparison. Figures 4.8, 4.9 and 4.10 show an increasing gas temperature with a fixed pressure of 300 $Torr$.

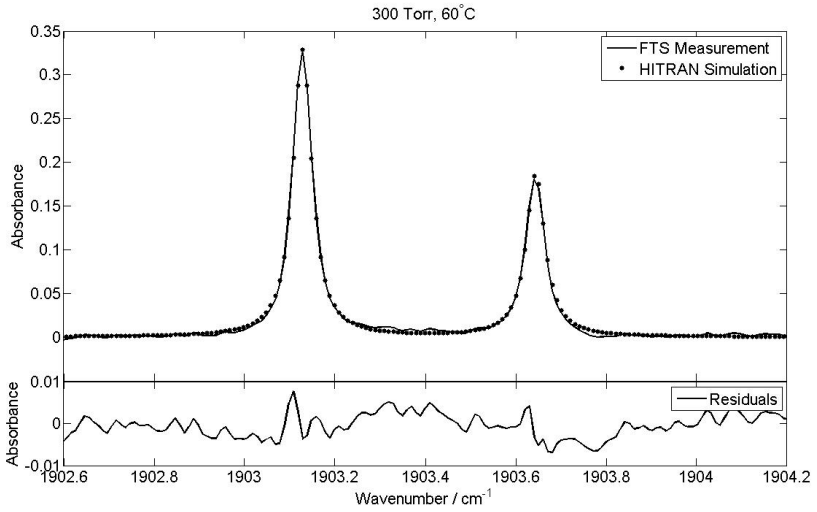

Figure 4.8: This shows a comparison of a RAL NO measurement of 3000 ppm, 300 $Torr$, 60 $°C$ and 9 cm with a HITRAN simulation under the same conditions. The measured data has had optical fringing removed and the simulation has been sampled at the same resolution as the measured data. The residuals of the fit are shown in the smaller plot.

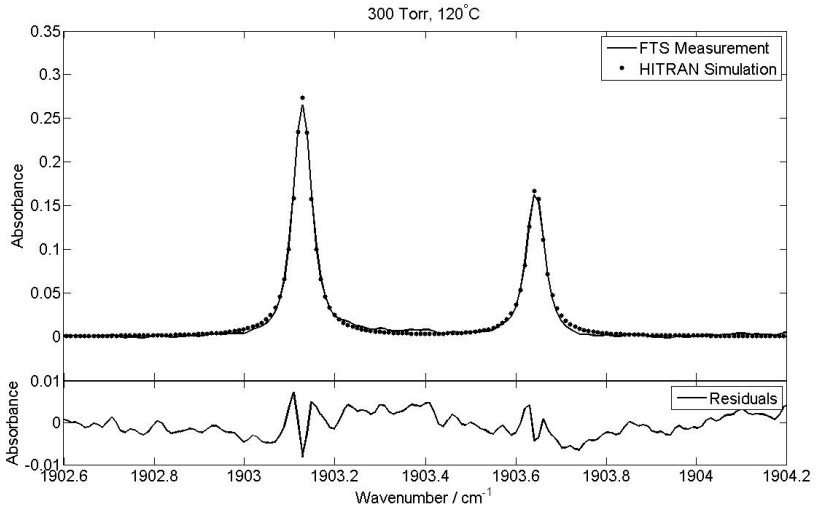

Figure 4.9: This shows a comparison of a RAL NO measurement of 3000 ppm, 300 $Torr$, 120 $°C$ and 9 cm with a HITRAN simulation under the same conditions. The measured data has had optical fringing removed and the simulation has been sampled at the same resolution as the measured data. The residuals of the fit are shown in the smaller plot.

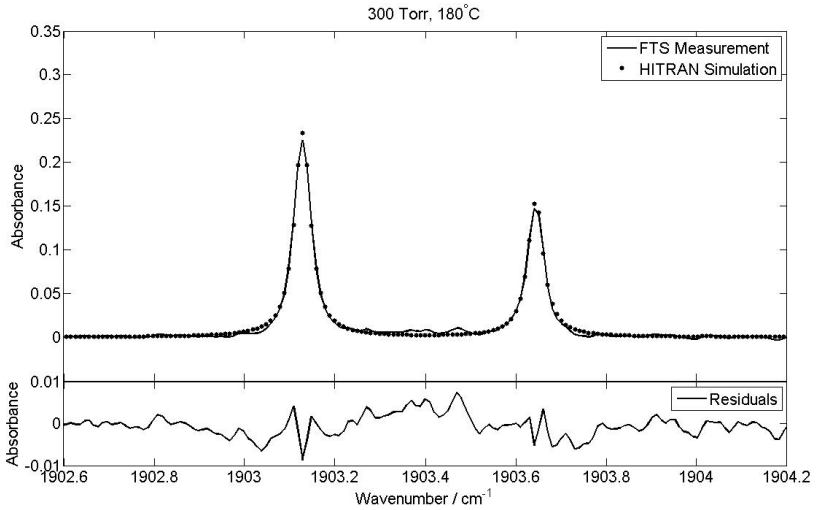

Figure 4.10: This shows a comparison of a RAL NO measurement of 3000 ppm, 300 $Torr$, 180 $°C$ and 9 cm with a HITRAN simulation under the same conditions. The measured data has had optical fringing removed and the simulation has been sampled at the same resolution as the measured data. The residuals of the fit are shown in the smaller plot.

The plots above show that the experimental data and the simulations based on the HITRAN database are in good agreement. There is some small error between the plots, the simulated data is in general 2-3 % stronger than the FTS measurements. This error is within the accuracy of the NO gas cylinder and could also be attributed to gas adsorbing while passing through the flow system. It is possible that the error is caused by an inaccuracy of the data within HITRAN, however the measurements show that the data is accurate enough to allow HITRAN to be used as a base for gas measurement. Figures 4.9, 4.11, 4.12 and 4.13 compare measurements with increasing pressures at a fixed temperature of 120 $°C$ to HITRAN simulations under the same conditions.

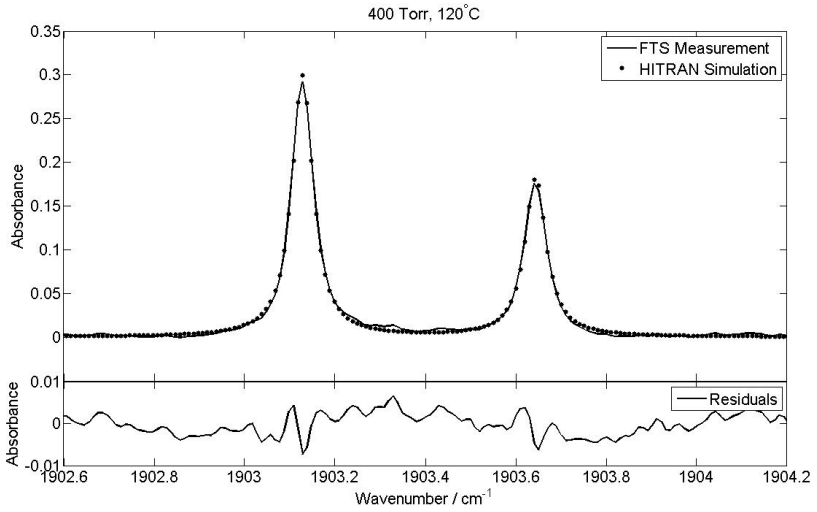

Figure 4.11: This shows a comparison of a RAL NO measurement of 3000 ppm, 400 $Torr$, 120 $°C$ and 9 cm with a HITRAN simulation under the same conditions. The measured data has had optical fringing removed and the simulation has been sampled at the same resolution as the measured data. The residuals of the fit are shown in the smaller plot.

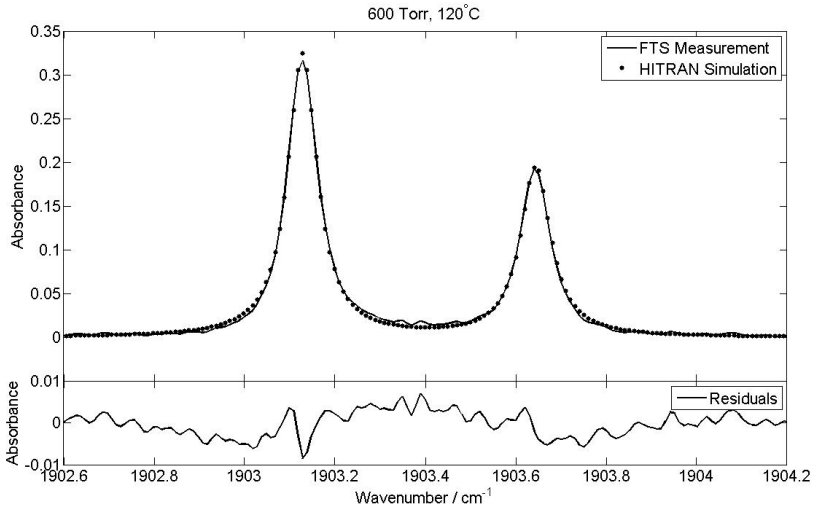

Figure 4.12: This shows a comparison of a RAL NO measurement of 3000 ppm, 600 $Torr$, 120 $°C$ and 9 cm with a HITRAN simulation under the same conditions. The measured data has had optical fringing removed and the simulation has been sampled at the same resolution as the measured data. The residuals of the fit are shown in the smaller plot.

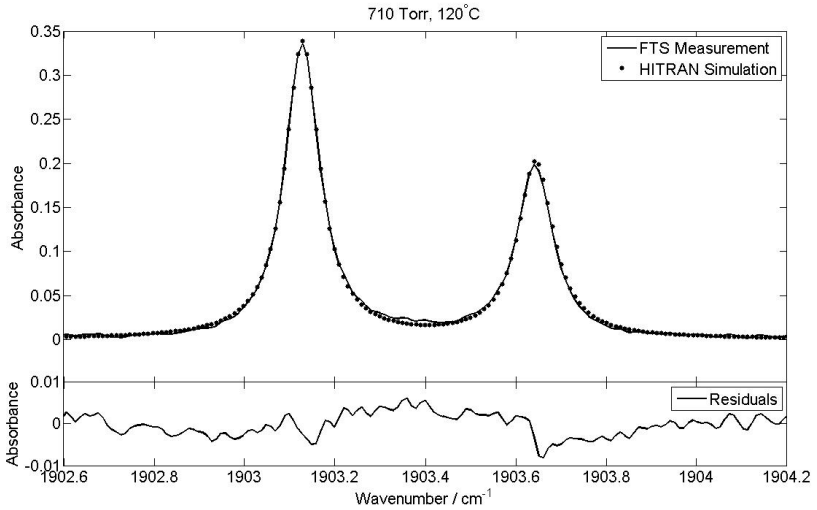

Figure 4.13: This shows a comparison of a RAL NO measurement of 3000 ppm, 710 $Torr$, 120 $°C$ and 9 cm with a HITRAN simulation under the same conditions. The measured data has had optical fringing removed and the simulation has been sampled at the same resolution as the measured data. The residuals of the fit are shown in the smaller plot.

The plots above show that the HITRAN simulations and the FTS measurements are in good agreement. The simulations and the measured data match well at each pressure. If higher resolution measurements were performed they may reveal an inaccuracy within the data, however there was no trend observed with changing pressure. The measurements performed at RAL verified that the data within HITRAN is accurate enough to perform gas measurements, however accurate gas measurements may require a correction factor.

4.3 NPL Testing and Type Approval

The verification and certification of Continuous Emission Monitoring Systems (CEMS) is necessary to allow their use as commercial sensors for continuous emissions. The Maritime and Coastguard Agency has a type approval scheme for the use CEMS in marine and offshore applications. Type Approval testing

was performed at the National Physical Laboratory (NPL) of a marine based gas sensor. There are numerous tests performed to verify the performance of the equipment being tested. The tests include drift, linearity, response time and cross interference which measure the sensors ability to accurately sense gas. Other tests such as ambient temperature, humidity and supply voltage changes measure the stability of the sensor in an industrial environment. The effect of gas pressure and temperature changes are also probed. The following sections highlight the linearity and cross interference tests which are the most significant from a spectroscopic viewpoint. An independent report was produced by NPL which confirms the results detailed in the following sections.

4.3.1 Experimental Setup

The sensor that these tests were performed on was configured to measure NO, NO_2, CO_2 and SO_2. For each gas measured a single QC laser of a suitable wavelength was used and the sensor was designed to make measurements *in-situ*. When installed on a ship, mid infrared optical fibre was used to couple light in and out of the stack using a two-pass probe with a total pathlength of 60cm. Fibre switchers were used to couple the light to multiple stacks allowing a single sensor to continuously measure several stacks simultaneously. While the testing was performed at NPL the sensor was reconfigured to couple light to a gas probe chamber where a single pass over 92cm was coupled back to the sensor for analysis. A diagram indicating the experimental setup is shown in figure 4.14.

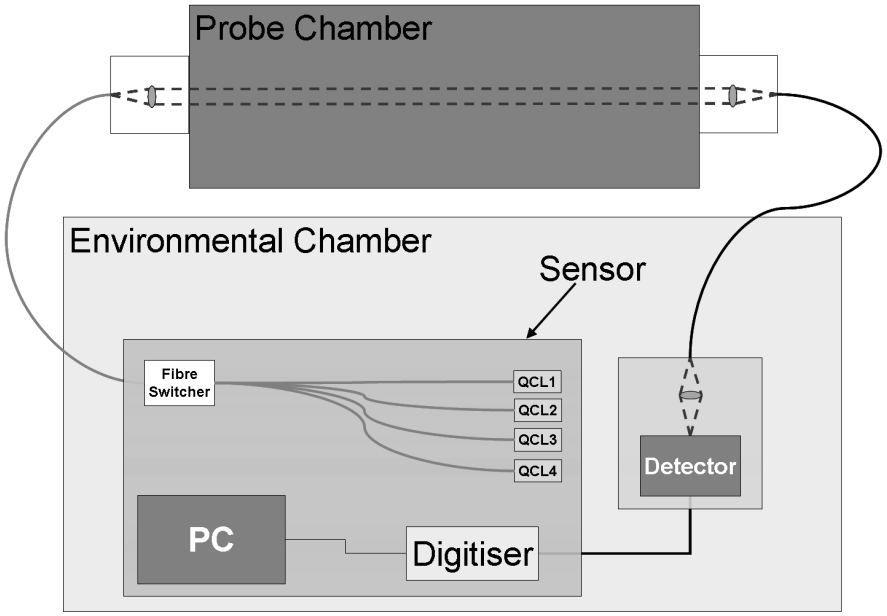

Figure 4.14: This shows an indication of the test setup used at NPL during the type approval testing. The sensor is operated within an environmental chamber to allow the ambient temperature and humidity to be controlled. The sensor operates four QC lasers which are coupled to a fibre switcher. An optical fibre is used to couple light from the sensor to a probe chamber. The light is then coupled back into a second fibre which leads to a detector. The signal from the detector is digitised then analysed by an onboard pc104. The probe chamber is a effectively a gas cell which is pressure and temperature controlled. A binary network is used to dilute various gases to precise concentrations which are then flowed through the probe chamber for measurement by the sensor.

During the testing the environmental chamber, which housed the sensor, was maintained at a temperature of 20°C with the exception of the ambient temperature tests. All four QC lasers were pulsed continuously with pulse widths and temperatures configured separately to measure the particular gas that each laser was intended for. The set voltage of each laser varied according to the characteristics of each laser. The pulse repetition frequency for each laser was fixed to a single value, this value was typically 20kHz. The fibre switcher was configured to make measurements consecutively. Each laser was be aligned to the probe chamber in turn, at which point the signal from

the detector was recorded by the digitiser. The digitiser was configured to average 500 pulses and the resulting data was transmitted to the pc104 for analysis by the spectral fitting algorithms, documented in 3.6 and 3.7. The time taken to complete each measurement was 40 to 60 seconds. This depended on the amount of data points generated by each laser and the amount of work that the fitting algorithms were required to do, as the difference between the solution and the initial guess increases, so does the time taken to complete the analysis. The resultant gas concentrations were logged by the pc104 and a Eurotherm Chessell 6000 Series datalogger (Model 6180XIO) was also used to record the gas measurements via a LAN connection. These measurements were used to complete the type approval analysis, in order to arrive at the results documented below and in the report generated by NPL.

The probe chamber was maintained at a temperature of 130°C except during the gas temperature tests. The gases supplied to the probe chamber were generated using a binary network, interferent gas blending unit, and a water vapour generator. Environmental data, including temperature, were recorded using a Hydra Fluke Data Logger. The source gases used for the tests were housed in a ventilated gas cylinder cabinet. According to NPL, the uncertainty in the absolute concentrations of the supplied gases delivered to the probe chamber during the tests was 5% relative to the value. The uncertainty of the binary network dilution of the binary gas mixtures was 0.5% of the value.

The gas measurement specifications of the sensor are listed in table 4.2. These specifications describe the gas sensing capability of the sensor while being tested at NPL, this is determined from the 92cm pathlength and the operating temperature of the probe chamber. While deployed on a ship the pathlength and temperature are both slightly different meaning that the specification is also slightly different.

The results of the testing were documented in a report [3] published by NPL. The report contains details of all the tests performed on the sensor. The following sections present the linearity and cross-interference results after

Fibre Coupled Sensor Specification		
Gas	Parameter	Value
NO	Detection Limit	11.12 ppm
	Resolution	5.38 ppm
	Full Range	2000 ppm
NO_2	Detection Limit	3.67 ppm
	Resolution	1.23 ppm
	Full Range	300 ppm
CO_2	Detection Limit	0.036 %
	Resolution	0.034 %
	Full Range	10 %
SO_2	Detection Limit	3.68 ppm
	Resolution	2.23 ppm
	Full Range	1750 ppm

Table 4.2: Gas measurement specification for the fibre coupled sensor, while installed on the 92cm NPL probe chamber. The detection limit was calculated as the concentration value that equates to 3 times the standard deviation above the sensor reading during a zero measurement. The resolution is calculated as three times the standard deviation.

analysis of the recorded data. The results shown in the following sections were compiled independently from NPL, however they were based on the same data which was collected jointly and confirm the results that can be found in the NPL report.

4.3.2 Linearity

In order to qualify for certification it is necessary to demonstrate a linearity of response to different concentrations. To calculate the linearity error, measurements were made across the full range of each gas at 0%, 10%, 30%, 50%, 70% and 90%. An average of several measurements was taken at each of these points. The process of calculating the linearity error is as follows.

1. The measurements, S_i, are zero corrected using the result from the zero measurement, Z_i, as shown in 4.1.

2. A response factor, f_i, is calculated from the known gas concentration, C_i, and the zero corrected measurements as shown in 4.2.

3. The true response, T_i is calculated using 4.3.

4. A linear regression is calculated from the true response and the known gas concentrations as in 4.4.

5. The A and B values calculated from the previous step are used to determine the predicted values of T_i for each supplied concentration.

6. The residual values, Res_i, at each point are calculated and the greatest absolute value is expressed as a percentage of the full range. This value is the linearity error and in order to pass the linearity test the error must be lower than 2%.

$$G_i = S_i - Z_i \tag{4.1}$$

$$f_i = \frac{C_i}{G_i} \tag{4.2}$$

$$T_i = G_i f_i \tag{4.3}$$

$$T_i = AC_i + B \tag{4.4}$$

The results from each linearity are shown below with the plots 4.15, 4.16, 4.17 and 4.18 displaying the results graphically. The tables 4.3, 4.4, 4.5 and 4.6 show the linearity analysis for each gas.

NO							
$T_i = AC_i + B$					$T_i = 1.000C_i + 18.367$		
C_i / ppm	S_i / ppm	G_i / ppm	f_i	T_i / ppm	Predicted T_i / ppm	Res_i / ppm	Res_{max} / ppm
0	11.828	0		0	18.367	-18.367	
215.3	238.544	226.716		232.47	233.623	-1.153	
620.2	648.8	636.972		653.138	638.438	14.699	
994.2	1018.878	1007.05		1032.608	1012.361	20.247	20.247
1423.1	1419.83	1408.002		1443.736	1441.172	2.564	
1814.7	1781.612	1769.784	1.025	1814.7	1832.69	-17.99	
Res_{max} / % FR							**1.012**

Table 4.3: Linearity analysis for NO, performed during type approval testing at NPL.

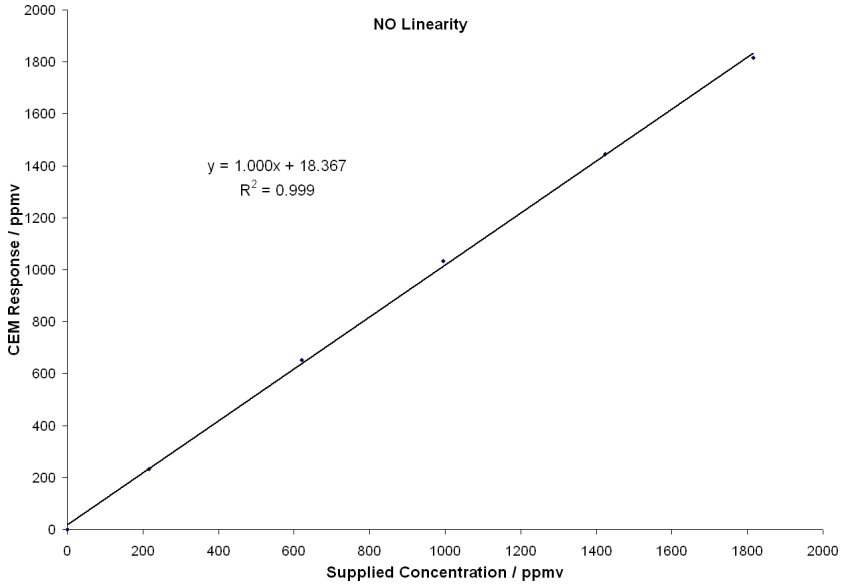

Figure 4.15: NO linearity graph showing the response of the sensor during type approval testing at NPL.

NO_2							
$T_i = AC_i + B$					$T_i = 1.011C_i - 0.835$		
C_i / ppm	S_i / ppm	G_i / ppm	f_i	T_i / ppm	Predicted T_i / ppm	Res_i / ppm	Res_{max} / ppm
0	0	0		0	-0.835	0.835	
34.2	32.343	32.343		31.183	33.725	-2.542	
90.7	94.188	94.188		90.81	90.82	-0.01	
150.6	159.693	159.693		153.966	151.35	2.616	2.616
212.7	223.215	223.215		215.211	214.104	1.106	
269.9	279.939	279.939	0.964	269.9	271.906	-2.006	
$\mathbf{Res_{max}}$ / % FR							**0.872**

Table 4.4: Linearity analysis for NO_2, performed during type approval testing at NPL.

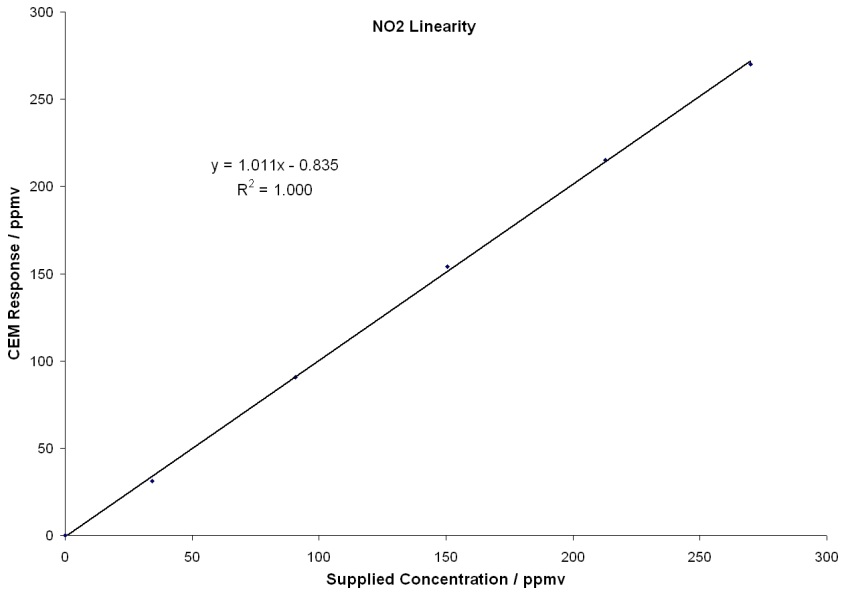

Figure 4.16: NO_2 linearity graph showing the response of the sensor during type approval testing at NPL.

CO_2							
$T_i = AC_i + B$					$T_i = 1.013C_i + 0.036$		
C_i / %	S_i / %	G_i / %	f_i	T_i / %	Predicted T_i / %	Res_i / %	Res_{max} / %
0	0	0		0	0.036	-0.036	
1	0.9	0.9		0.936	1.049	-0.113	
3.06	3.104	3.104		3.229	3.136	0.093	
5.09	5.122	5.122		5.328	5.193	0.136	
7.08	7.001	7.001		7.283	7.209	0.074	
9.01	8.661	8.661	1.04	9.01	9.164	-0.154	-0.154
Res_{max} / % FR							**-1.54**

Table 4.5: Linearity analysis for CO_2, performed during type approval testing at NPL.

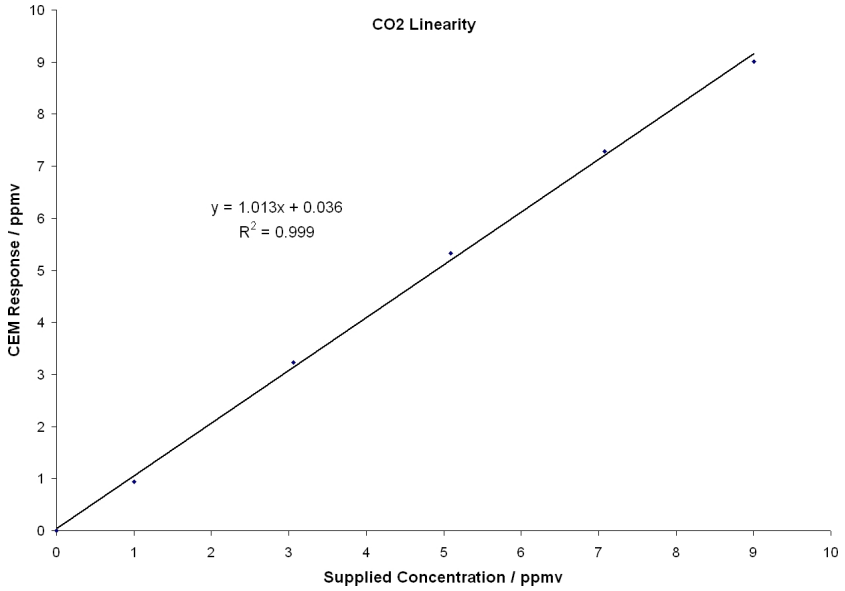

Figure 4.17: CO_2 linearity graph showing the response of the sensor during type approval testing at NPL.

SO_2							
$T_i = AC_i + B$					$T_i = 1.018C_i - 32.219$		
C_i / ppm	S_i / ppm	G_i / ppm	f_i	T_i / ppm	Predicted T_i / ppm	Res_i / ppm	Res_{max} / ppm
0	0	0		0	-32.219	32.219	32.219
174.5	124	124		127.102	143.941	-16.84	
542	484.804	484.804		496.93	514.957	-18.027	
878.2	822.936	822.936		843.52	854.374	-10.854	
1219.7	1198.086	1198.086		1228.053	1208.925	19.128	
1561.4	1523.299	1523.299	1.025	1561.4	1544.11	17.29	
Res_{max} / % FR							**1.898**

Table 4.6: Linearity analysis for SO_2, performed during type approval testing at NPL.

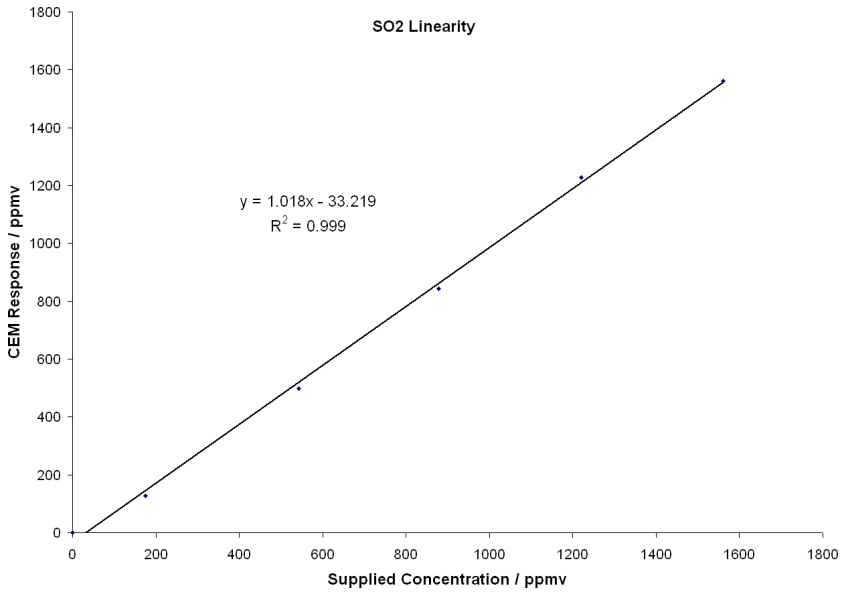

Figure 4.18: SO_2 linearity graph showing the response of the sensor during type approval testing at NPL.

4.3.3 Cross-Interference

The effects of other gases on the primary measurements are tested by measuring zero and span readings both with and without the presence of an interfering species. The interferents used were N_2O, CH_4, CO_2 and H_2O. As mention in 4.1.1 the interferents can introduce errors by more than one

method, much of the fitting routine development, discussed in 3.6 and 3.7, was driven by these tests.

In order to pass the cross interference test it is necessary to demonstrate a response of less than 2% of the full range of the measurement for each interference, both on a zero and span reading. To calculate the error, measurements were made at a zero and span concentration value of 70-80% for each gas both with and without the interfering gas. An average of several measurements was taken at each of these points. The process of calculating the cross interference errors is as follows.

1. For each cross interference test four measurements of the gas sensor reading for the test gas are required. A zero measurement with neither the test gas or the interfering gas present is recorded, Z_i. This is followed by span measurements on both the test gas and the interfering gas only, S_i and Z_i^{int} respectively. Finally, a measurement in the presence of both gases is taken, S_i^{int}.

2. The values are zero corrected, the Z_i measurement is used to correct the S_i and Z_i^{int} measurements and the Z_i^{int} measurement is used to correct the S_i^{int} measurement. This is shown in 4.5.

3. A response factor, f_i, is calculated from the known gas concentration, C_i, and the zero corrected span measurement as shown in 4.6.

4. The true responses for span and zero were obtained for each measurement, T_i^{span} and T_i^{zero}. As shown in 4.7.

5. The known concentration values are subtracted from the true responses to obtain the error for each measurement, cs_i. The response is then expressed as a percentage of the full range, these values must remain under 2% to pass the individual cross interference tests.

6. For each test gas the individual cross interference tests are then summed to obtain the overall cross sensitivity contribution, R_i. This value must remain under 4% to allow the cross interference test to be passed.

$$\begin{aligned} G_i &= S_i - Z_i \\ H_i^{int} &= Z_i^{int} - Z_i \\ G_i^{int} &= S_i^{int} - Z_i^{int} \end{aligned} \tag{4.5}$$

$$f_i = \frac{C_i}{G_i} \tag{4.6}$$

$$\begin{aligned} T_i^{span} &= G_i^{int} f_i \\ T_i^{zero} &= H_i^{int} f_i \end{aligned} \tag{4.7}$$

NO								
Gas	S, Z / ppm	G, H / ppm	C / ppm	f	T / ppm	cs / ppm	cs / % FR	
							Zero	Span
N_2	6.055	0	0		0	0		
NO	1483.513	1477.458	1510.7	1.022	1510.7	0		
CH_4	6.235	0.18	0		0.184	0.184	**0.009**	
NO/CH_4	1486.572	1480.337	1510.7		1513.644	2.944		**0.147**
NO	1489.099	1483.043	1516.3	1.022	1516.3	0		
N_2O	6.465	0.41	0		0.419	0.419	**0.021**	
NO/N_2O	1492.235	1485.77	1516.3		1519.087	2.787		**0.139**
NO	1492.895	1486.839	1522.2	1.024	1522.2	0		
CO_2	5.285	-0.771	0		-0.789	-0.789	**-0.039**	
NO/CO_2	1498.31	1493.026	1522.2		1528.534	6.334		**0.317**
NO	1474.325	1468.269	1510.9	1.029	1510.9	0		
H_2O	0	-6.055	0		-6.231	-6.231	**-0.312**	
NO/H_2O	1445.769	1445.769	1510.9		1487.746	-23.154		**-1.158**
						R	**-0.321**	**-0.554**

Table 4.7: This shows the cross interference analysis for NO, the tests were performed at NPL during type approval.

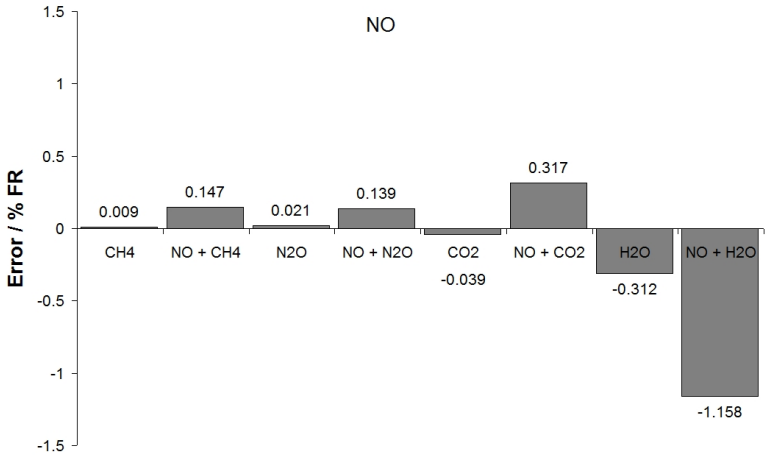

Figure 4.19: *NO* Cross Interference Results

NO_2								
Gas	*S*, *Z* / ppm	*G*, *H* / ppm	*C* / ppm	*f*	*T* / ppm	*cs* / ppm	*cs* / % FR	
							Zero	Span
Air	0	0	0		0	0		
NO_2	238.732	238.732	227.1	0.951	227.1	0		
CH_4	0	0	0		0	0	**0**	
NO_2/CH_4	238.499	238.499	227.1		226.878	-0.222		**-0.074**
NO_2	238.186	238.186	227.3	0.954	227.3	0		
N_2O	0	0	0		0	0	**0**	
NO_2/N_2O	237.181	237.181	227.3		226.34	-0.96		**-0.32**
NO_2	235.015	235.015	224.5	0.955	224.5	0		
CO_2	0	0	0		0	0	**0**	
NO_2/CO_2	234.342	234.342	224.5		223.857	-0.643		**-0.214**
NO	235.054	235.054	225.3	0.959	225.3	0		
H_2O	0.075	0.075	0		0.072	0.072	**0.024**	
NO_2/H_2O	234.593	234.518	225.3		224.786	-0.514		**-0.171**
						R	**0.024**	**-0.78**

Table 4.8: This shows the cross interference analysis for NO_2, the tests were performed at NPL during type approval.

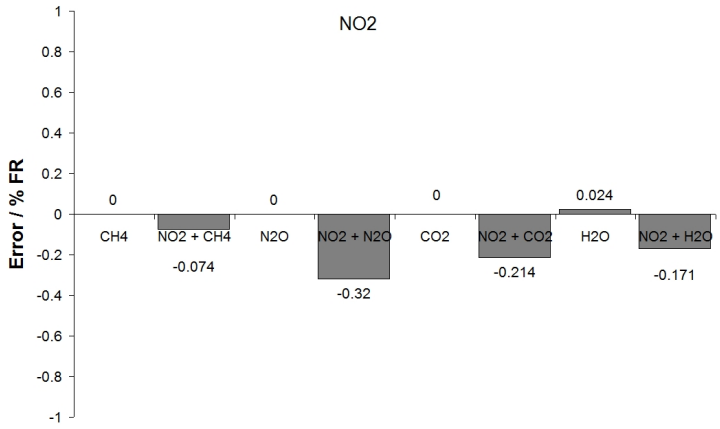

Figure 4.20: NO_2 Cross Interference Results

CO_2								
Gas	S, Z / %	G, H / %	C / %	f	T / %	cs / %	cs / % FR	
							Zero	Span
Air	0	0	0		0	0		
CO_2	7.344	7.344	7.5	1.021	7.5	0		
H_2O	0	0	0		0	0	**0**	
CO_2/H_2O	7.419	7.419	7.5		7.577	0.077		**0.767**
CO_2	7.361	7.361	7.52	1.022	7.52	0		
CH_4	0	0	0		0	0	**0**	
CO_2/CH_4	7.37	7.37	7.52		7.529	0.009		**0.085**
CO_2	7.392	7.392	7.54	1.02	7.54	0		
N_2O	0	0	0		0	0	**0**	
CO_2/N_2O	7.301	7.301	7.54		7.447	-0.093		**-0.932**
						R	**0**	**-0.08**

Table 4.9: This shows the cross interference analysis for CO_2, the tests were performed at NPL during type approval.

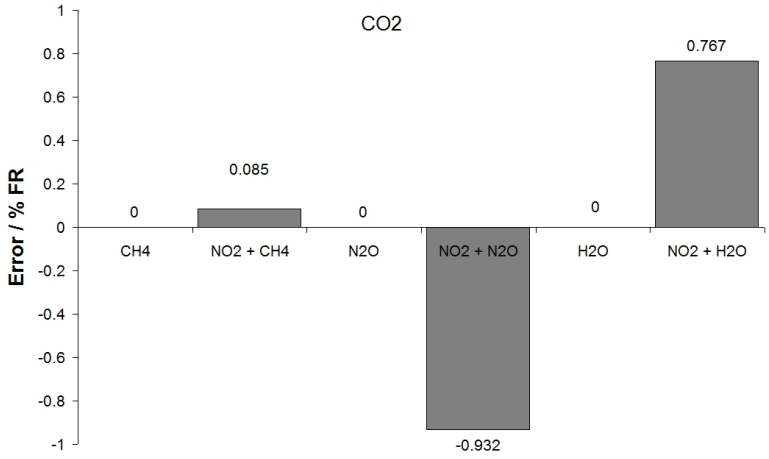

Figure 4.21: CO_2 Cross Interference Results

SO_2								
Gas	*S*, *Z* / ppm	*G*, *H* / ppm	*C* / ppm	*f*	*T* / ppm	*cs* / ppm	*cs* / % FR	
							Zero	Span
Air	0	0	0		0	0		
SO_2	1337.05	1337.05	1312.7	0.982	1312.7	0		
CH_4	0.483	0.483	0		0.475	0.475	**0.027**	
SO_2/CH_4	1315.711	1315.228	1312.7		1291.275	-21.425		**-1.224**
SO_2	1329.444	1329.444	1324.1	0.996	1324.1	0		
N_2O	0	0	0		0	0	**0**	
SO_2/N_2O	1335.529	1335.529	1324.1		1330.16	6.06		**0.346**
SO_2	1326.454	1326.454	1302.2	0.982	1302.2	0		
CO_2	0.868	0.868	0		0.852	0.852	**0.049**	
SO_2/CO_2	1313.226	1312.358	1302.2		1288.362	-13.838		**-0.791**
SO_2	1321.818	1321.818	1312.7	0.993	1312.7	0		
H_2O	0	0	0		0	0	**0**	
SO_2/H_2O	1292.354	1292.354	1312.7		1283.439	-29.261		**-1.672**
						R	**0.076**	**-3.341**

Table 4.10: This shows the cross interference analysis for SO_2, the tests were performed at NPL during type approval.

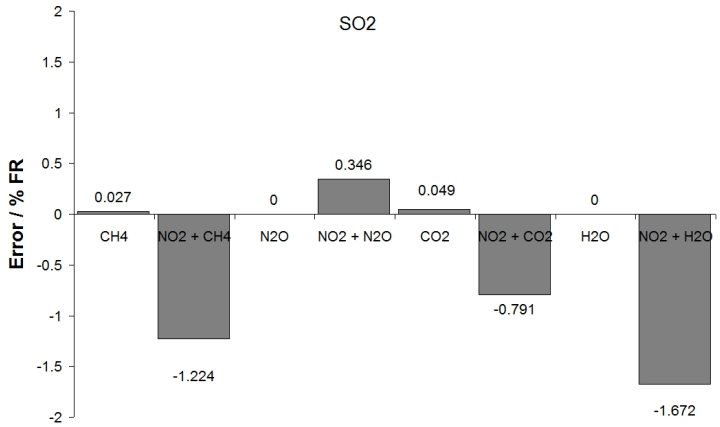

Figure 4.22: SO_2 Cross Interference Results

4.3.4 Conclusions

The successful results of the NPL testing showed that the sensor technology was sufficiently advanced to merit its inclusion in a marine based gas sensor product. However the testing also highlighted the areas where there was room for improvement. Perhaps the greatest area of difficulty is the sensors susceptibility to cross-interference, particularly from the effects of H_2O. The high occurrence of H_2O absorption lines throughout the mid-infrared spectrum together with the high concentrations found in exhausts makes the effects the most difficult to predict.

The development of the sensor technology led to improvements in this area, however the issues associated with cross-interference effects remains one of the most difficult issues.

4.4 Industrial Trials

A major aspect of the development of QC laser gas sensing has been the design, testing and industrial trials of prototype sensors in a variety of environments. The industrial trials serve several purposes, such as demonstrating the technology, collecting data to assess performance, discovering design is-

sues and testing the durability of a sensor in a harsh environment. These trials have taken place in a number of industrial environments, however the most extensive trials were conducted on the engine stacks of a cross channel passenger ferry. An overview of the legislation that has driven the need for such sensors is given in the following section, the target gases and the QC laser wavelengths used to detect and measure them is detailed. The remainder of this section describes three iterations of a marine sensor. Each of these sensors were tested at NPL and installed on ship stacks as part of a series of industrial trials.

The important aspects of the sensor were the speed, stability and maintenance requirements during continuous operation in a harsh industrial environment as well as the accuracy and precision of the measurements. However, in order to give an indication of the performance of the sensor at the different stages of development the detection limit of the sensor is given by three times the standard deviation above a zero measurement and the resolution is defined as three times the standard deviation. This definition is shown graphically in figure 4.23.

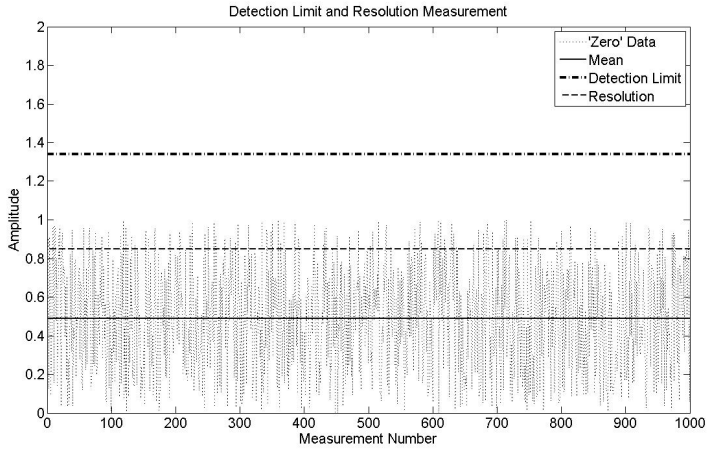

Figure 4.23: This figure shows method used to calculate the detection limit and resolution. The sensor reading produced in the absence of any absorbing gases is analysed to obtain the standard deviation, this value is multiplied by a factor of three to give the measurement resolution. The detection limit is obtained by adding the resolution to the average value of the zero measurement.

4.4.1 Legislation

There has been increasing public and academic concern for the impact of man-made emissions on the environment. Climate change has the potential to have profound effects on our current way of life. Damage to agriculture, water shortages, impact on the world economy and public health are all major concerns that can be linked to changes in the environment. As a consequence legislation governing the environment and industrial emissions has become a large branch of national and international law. There has been much media attention upon the subject of reducing emissions to meet various targets over time. In order for industrial emissions to be reduced the relevant industries must have methods of continuously monitoring their emissions. The convention that governs marine pollution is MARPOL 73/78 which is the IMO International Convention for the Prevention of Pollution from Ships [4].

4.4.2 Target Gases

Target gases that are commonly measured include NO, NO_2, CO_2 and SO_2. Due to the nature of the typical output from a ship stack there were a number of cross-interfering gases present in addition to substantial particulate matter. The expected gas content and concentrations of the scrubbed and unscrubbed stacks were established through work completed during a series of preliminary trials that were not part of the research covered by this thesis. One QC laser was used to measure each gas and the wavelengths were selected to avoid cross-interference effects and balance the concentration ranges with pathlength. Figures 4.24, 4.25, 4.26 and 4.27 show simulations of the regions selected to perform concentration measurements on each of the gases. The wavenumber scale on the following graphs is displayed as relative wavenumber, this is due to commercial reasons.

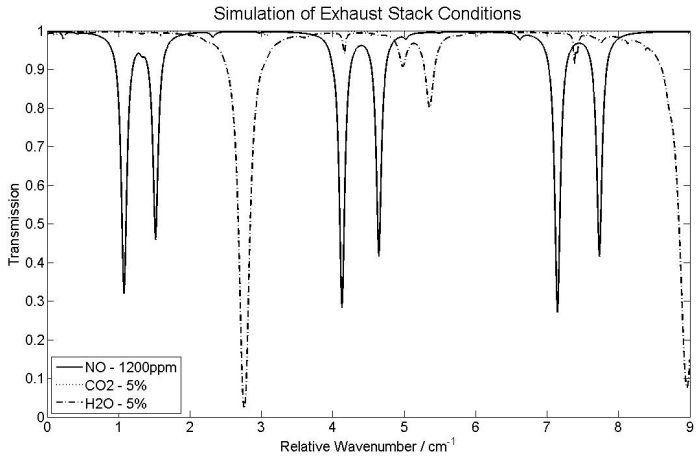

Figure 4.24: This figure shows the wavelength region used to measure NO concentrations within a stack. The temperature is $300°C$ and the pressure is atmospheric. This region also contains absorption lines from H_2O and CO_2. NO measurements are possible and have been performed on each of the three wavelengths where NO lines are dominant. The first position offers the best window in absorption lines from other gases, however QC laser availability often limits the measurement to one of the other two options.

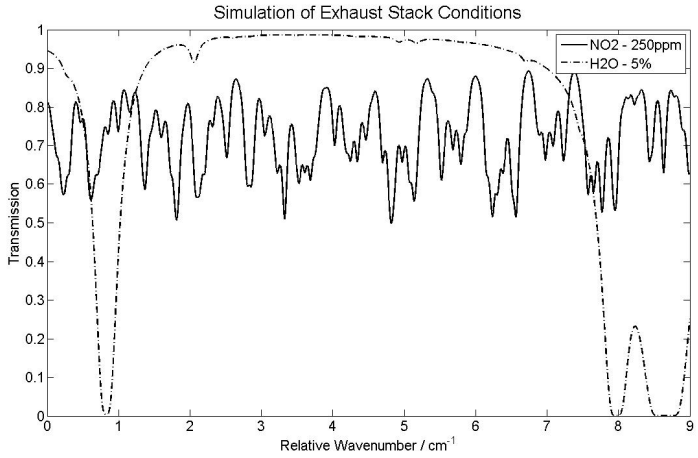

Figure 4.25: This shows the wavelength region used to measures NO_2 concentrations. The stack conditions are $300°C$ and atmospheric pressure. Due to the large window in H_2O lines there are a number of potential measurement points. The QC lasers used can be configured to operate at an optimal temperature since there is an abundance of suitable measurement locations.

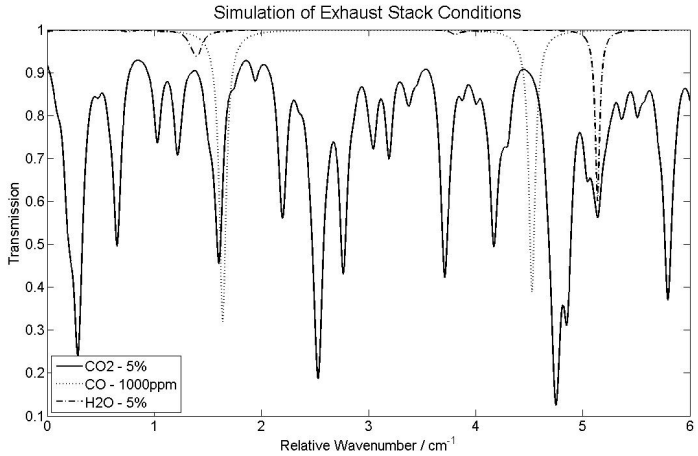

Figure 4.26: This shows the region used to measure CO_2 concentrations. The stack conditions are $300°C$ and atmospheric pressure. The QC lasers used were usually configured to cover the highly characteristic group of three CO_2 lines.

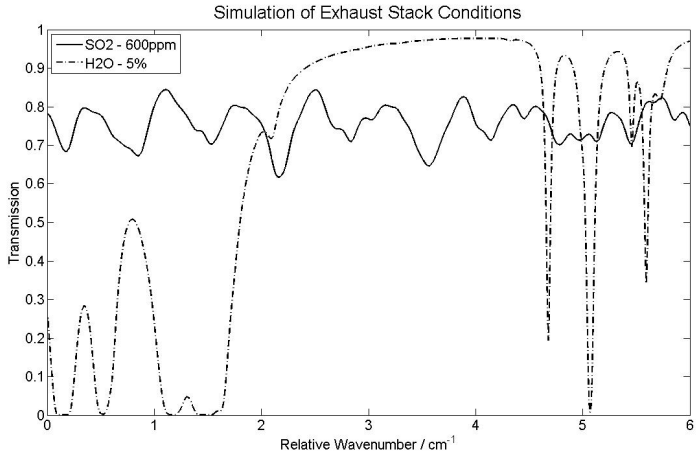

Figure 4.27: The region used to measure SO_2 concentrations. The stack conditions are $300°C$ and atmospheric pressure. There is a high coincidence between SO_2 and H_2O absorption lines, therefore there are a limited number of points where SO_2 measurements are possible. This window is one of the few positions that can be used for SO_2 measurement.

As can be seen in the plots, the largest contribution to cross-interference is as a result of the high water content. The typical water content observed was 5-10%, The interference presents itself as a change in the broadening behaviour of the target gases as well as limiting the wavelength regions were measurements are possible.

4.4.3 CT1000 - Fibre Coupled Probe Sensor

The fibre-coupled probe sensor described in this section was the same type of CEMS sensor evaluated during the type approval testing discussed in 4.3. This testing was used to develop the majority of the analysis algorithms used to pass type approval. The testing also allowed a certain amount of refinement to take place on the mechanical hardware, electronics systems and software. The diagram in figure 4.28 shows the sensor and a single probe.

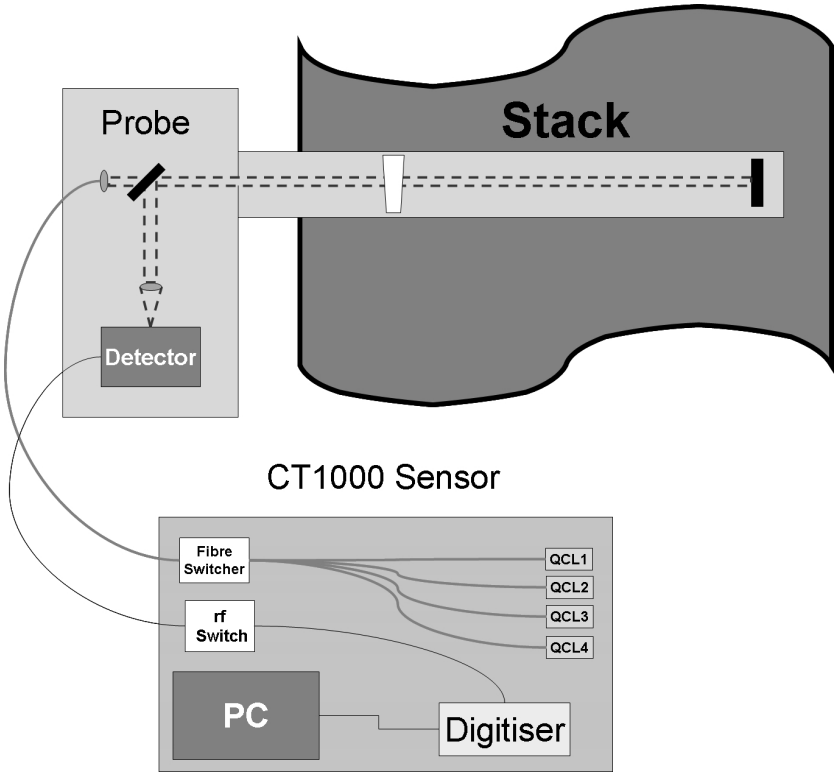

Figure 4.28: This shows the CT1000 and a single probe used during an industrial trial. The four QC lasers can be individually coupled to multiple probes via a fibre switcher. The probe consists of a mechanical assembly which is connected to a stack. The probe is split into two sections, the first contains the fibre coupling optics and detector while the second section is positioned within the stack and sealed from the first section by a wedged CaF_2 window. The far side holds a mirror to allow a double pass through the length of the probe. The top and bottom of the second section is perforated and holds filter assemblies to allow gas to enter the beam path while preventing any particulate matter from attenuating the signal. The detector records the laser pulse and returns the signal to the sensor where an rf switch allows multiple probes to be connected. The sensor houses a pc104 which controls the various components of the sensor and analyses the measured data.

This sensor used multimode optical fibre to couple light in and out of a probe which directed the mid infrared beams into an exhaust stack. The measurement pathlength was simply a double pass along the length of the probe. The optical fibre allowed a centrally located sensor to measure the exhaust from several stacks by using a combination of fibre switchers and rf switches to direct the light and detector signal to and from different stack probes. In this sensor the gas temperature inside the stack was measured, however the pressure was not, tests from earlier trials indicated that the pressure within the stack was stable and that the error introduced by pressure variations would be negligible. The internal section of the probe was heated to avoid corrosive deposits forming o the probe and to prevent the filter assemblies from clogging with water or particulate matter. The electronics systems included drive electronics for four QC lasers and a detection system which used a digitiser to record the QC laser pulses. The sensor was controlled by an on-board PC104 and the recorded pulses were analysed using the algorithms discussed in sections 3.6 and 3.7. The results were logged to a hard drive as well as published to a data logger.

The specification of the sensor is shown in table 4.11. One of the major ways in which this sensor differed from the sensor used for the NPL tests is pathlength. The pathlength of this sensor was 60cm, this leads to a reduction in performance for resolution and detection limit, however the full range of detection is increased.

Test Results

This sensor was extensively tested at NPL, some of the results of this testing are documented in section 4.3. The tests performed at NPL verified the accuracy of the sensor and the performance of the spectral fitting algorithms. Other tests that were performed consisted of ambient temperature tests, variations in supply voltage, repeatability and response tests to name a few. These were intended to demonstrate the robustness and stability of the sensor.

Fibre Coupled Sensor Specification		
Gas	Parameter	Value
NO	Detection Limit	16.65 ppm
	Resolution	8.07 ppm
	Full Range	3000 ppm
NO_2	Detection Limit	5.52 ppm
	Resolution	1.83 ppm
	Full Range	450 ppm
CO_2	Detection Limit	0.054 %
	Resolution	0.05 %
	Full Range	15 %
SO_2	Detection Limit	5.52 ppm
	Resolution	3.35 ppm
	Full Range	2600 ppm

Table 4.11: Gas measurement specification for the fibre coupled sensor used during the exhaust stack trials, in this case the pathlength is 60cm. The detection limit was calculated as the concentration value that equates to 3 times the standard deviation above the sensor reading during a zero measurement. The resolution is calculated as three times the standard deviation.

Trial Results

This sensor was used in a number of ship trials and was often set up to simultaneously measure scrubbed and ordinary stacks. On stacks that were scrubbed a prototype SO_2 scrubber was install to remove the SO_2 from the exhaust gas. Figures 4.29, 4.30, 4.31 and 4.32 show a single days worth of data from scrubbed and ordinary stacks.

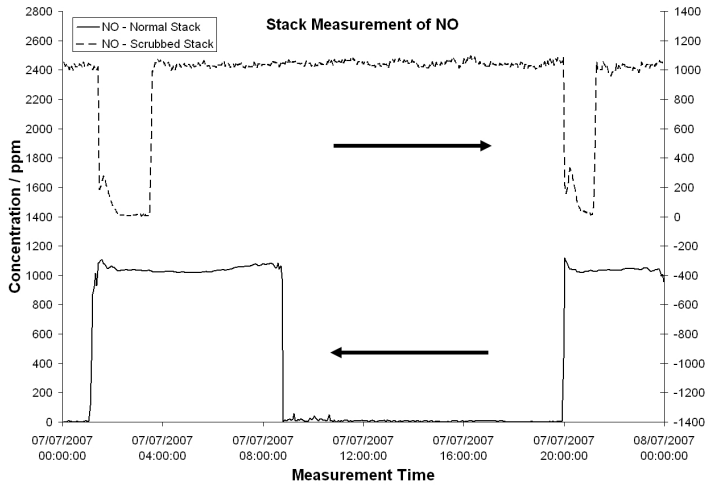

Figure 4.29: This shows a day of NO concentrations analysed by a CT1000 which was coupled to a scrubbed and an ordinary stack. The stacks were connected to auxiliary engines that were used to provide electrical power to a cross-channel ferry. The NO concentrations between the two stacks are similar since the same type of fuel was being used to run the engines. When the individual engines are switched off the NO falls to a zero level.

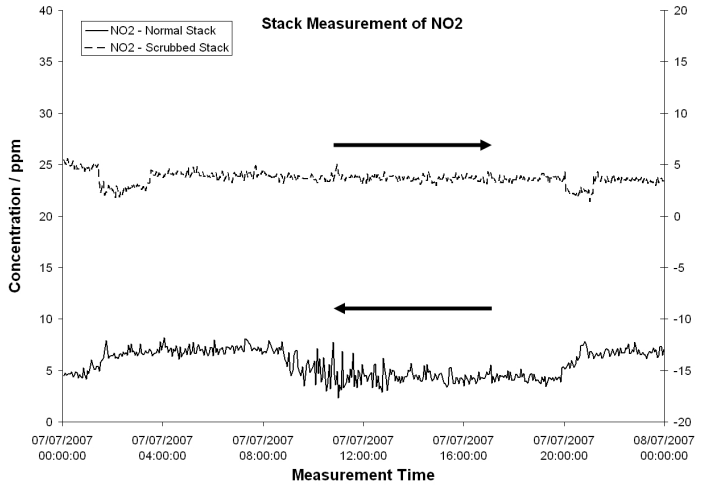

Figure 4.30: This shows a day of NO_2 concentrations analysed by a CT1000 which was coupled to a scrubbed and an ordinary stack. The stacks were connected to auxiliary engines that were used to provide electrical power to a cross-channel ferry. The low levels of NO_2 are produced by NO reacting with oxygen to form NO_2. When the engines are switched off it appears as though some of the gas does not dissipate, however the NO_2 concentration level falls below the detection limit of 5.52ppm.

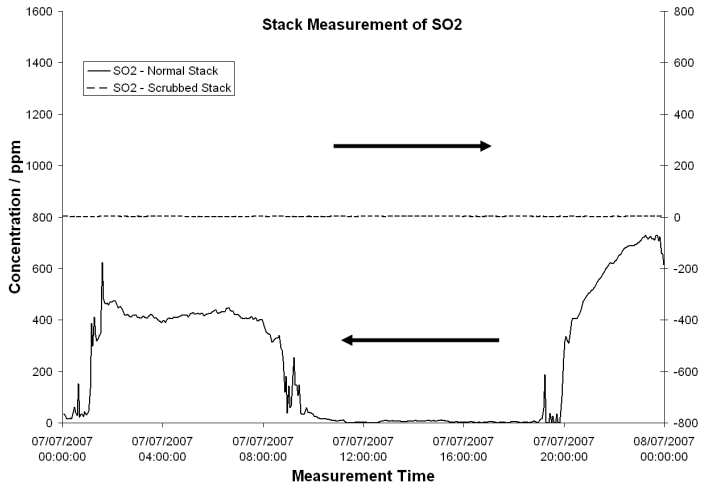

Figure 4.31: This shows a day of SO_2 concentrations analysed by a CT1000 which was coupled to a scrubbed and an ordinary stack. The stacks were connected to auxiliary engines that were used to provide electrical power to a cross-channel ferry. The SO_2 concentrations between the two stacks are different because the SO_2 on the scrubbed stack is removed by the SO_2 scrubber. When the individual engines are switched off the SO_2 falls to a zero level.

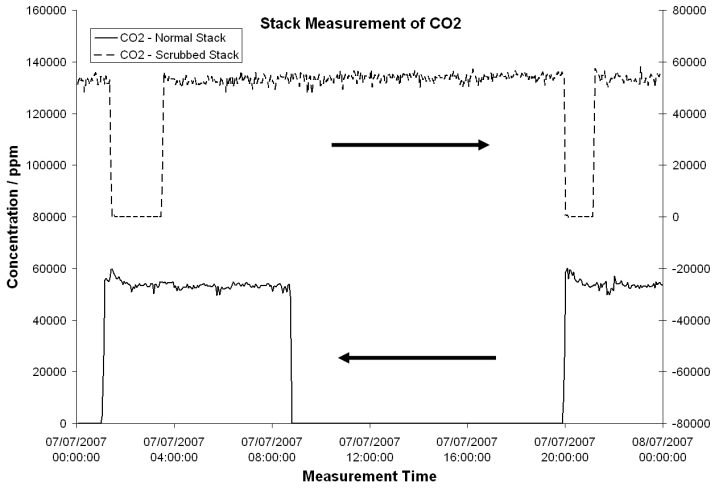

Figure 4.32: This shows a day of CO_2 concentrations analysed by a CT1000 which was coupled to a scrubbed and an ordinary stack. The stacks were connected to auxiliary engines that were used to provide electrical power to a cross-channel ferry. The CO_2 concentrations between the two stacks are similar since the same type of fuel was being used to run the engines. When the individual engines are switched off the CO_2 falls to a zero level.

The data shown in the previous graphs proved that measurements of stack gases were possible. However the sensor required significant maintenance to provide continual concentration measurements. The continual switching of the four lasers through multiple stack probes which were subject to fluctuating gas flow rates and temperatures led to alignment problems. The speed of the analysis was limited by the use of an onboard PC104.

Conclusions

This trial further demonstrated the suitability of QC Lasers for use in sensors that must be robust enough to operate in harsh environments. Ultimately the sensor was not considered suitable for the intended application. The reasons for this were as follows, the high cost and various problems associated with the mid infrared optical fibres made the long term use of optical fibres undesirable. The on-board PC104 lacked the computing power to quickly analyse the recorded data, measurement speeds greater than 0.1Hz could

not be reliably met. The concept of a central sensor measuring several stacks was decided to be impractical. The design of the sensor was reviewed and an *in-situ* sensor that was based entirely on free-space laser beams was produced. The results of the trials of this sensor are presented in the following section.

4.4.4 CT2000 - Free Space Probe Sensor

The free space probe sensor was based around a more modular design, the QC laser drive electronics and the detection system were contained within an enclosure referred to as the CT2000. This enclosure also contained collimation and alignment optics which were used to direct the four beams onto a single, central prism which allowed the beams to exit the enclosure in a tightly confined group. Once the beams had been passed through the gas mix under study they could be redirected to the enclosure where they where focused onto a detector. An on-board digitiser would record the laser signal, which would then be transmitted to a separate pc for analysis. The analysis routines used in this sensor were the same as those used for the previous sensor. A diagram of the Free Space Probe sensor can be found in figure 4.33.

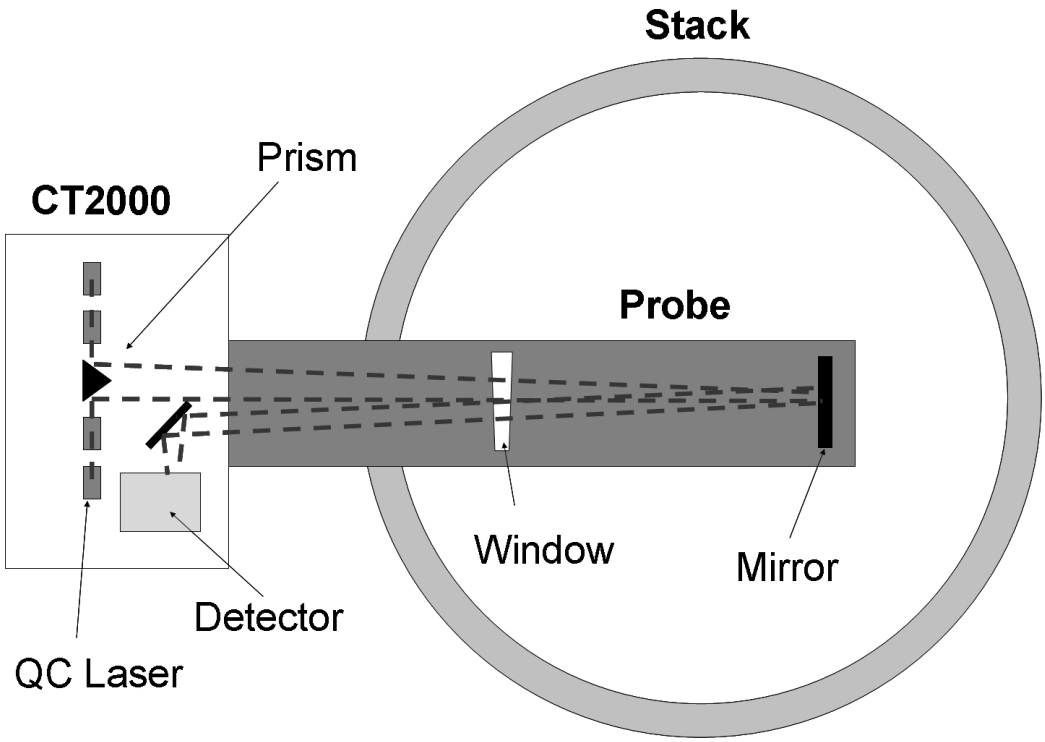

Figure 4.33: This shows a diagram of a CT2000 and probe attached to an exhaust stack. As with the CT1000 four QC lasers are present in the sensor, however all mid-infrared fibre has been removed. The radiation is directed through free space from each individual laser to a central reflective prism which directs the combined beams along a probe positioned within an exhaust stack. The probe contains a window to isolate the stack from the ambient environment and a mirror to return the beams to the CT2000 enclosure and onto a detector. The signal from the detector is measured by an on board digitiser. The system is controlled by a separate computer which also performs the data analysis.

The enclosure was designed to be used in a number of applications, in the case of stack measurements the enclosure was connected directly to a probe. The probe allowed a double pass through the stack gas along the length of the probe. A window part way along the probe was used to isolate the stack from the sensor and surrounding atmosphere. This boundary defined the beginning and end of the absorption pathlength.

The performance of this sensor is shown in table 4.12. There was only a slight improvement in detection limit performance, however the purpose of

the design change concerned the stability and maintainability. The improvement in these factors led to a more robust sensor.

Fibre Coupled Sensor Specification		
Gas	Parameter	Value
NO	Detection Limit	13.18 ppm
	Resolution	8.47 ppm
	Full Range	3000 ppm
NO_2	Detection Limit	2.54 ppm
	Resolution	1.84 ppm
	Full Range	450 ppm
CO_2	Detection Limit	0.022 %
	Resolution	0.011 %
	Full Range	15 %
SO_2	Detection Limit	1.52 ppm
	Resolution	0.73 ppm
	Full Range	2600 ppm

Table 4.12: Gas measurement specification for the CT2000 sensor used during the exhaust stack trials, in this case the pathlength is 60cm. The detection limit was calculated as the concentration value that equates to 3 times the standard deviation above the sensor reading during a zero measurement. The resolution is calculated as three times the standard deviation.

Trial Results

There were extensive trials performed with this sensor design. An example of the results that were produced is given in figure 4.34.

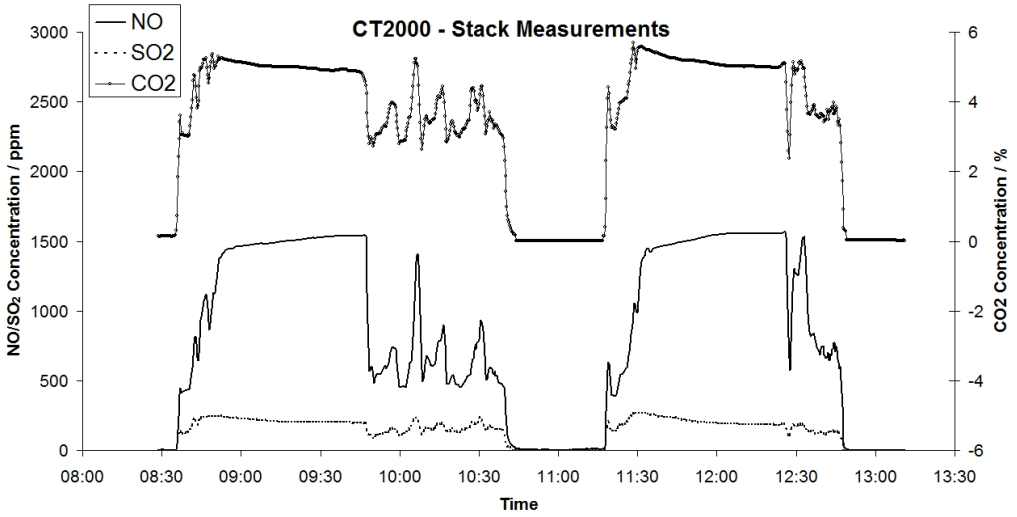

Figure 4.34: This shows concentration measurements on a main engine stack of NO, SO_2 and CO_2. The measurements were performed on a cross channel ferry, two crossings are shown. The gas output is low when the ship is docked and high when the ship is in motion. The erratic measurements are due to varying engine load when the ship is manoeuvring in preparation for docking.

The concentration output shown above was a typical output from the sensor. The purpose of these trials was to develop and then prove the industrial robustness and stability of the sensor in preparation for its release as a marine based gas sensing product.

Conclusions

The results of the tests performed at NPL, which are presented in section 4.3, showed that this sensor was capable of producing accurate results and the use of a separate pc allowed the analysis rate to reach speeds of approximately 1Hz. During industrial trials it was found that there were issues with the probe used to interface the sensor to the stack. In order to avoid rapid deterioration of the probe through corrosion it was heated, however a heater or thermistor failure could rapidly lead to large errors in the retrieved concentration values. There were other issues surrounding the window, the quality of the seal between the stack and the ambient environment was diffi-

cult to maintain due to the high temperatures involved and the requirement of a wedged window to avoid optical fringing. The use of a probe to make an *in-situ* sensor also placed limits on the pathlength that could be achieved with the sensor. This in effect limited the maximum sensitivity that could be achieved by the sensor.

While the probe was not considered reliable enough to produce robust and stable gas sensing products the CT2000 enclosure marked a significant step forward in terms of the electronic, software and optical systems. For these reasons it was determined that the CT2000 enclosure should be used to produce a rapid prototype of an extractive based sensor. This sensor was trialled and produced both accurate and reliable results. This led to the development of the local extractive sensor described in the following section.

4.4.5 CT2100 - Local Extractive Sensor

Due to the varying sizes of exhaust stacks, it was determined that an *in-situ* sensor would be unable to achieve the pathlengths required to provide sufficient sensitivity for all applications. Maintaining the physical condition of an optical probe over long time periods was difficult. For these reasons an extractive sensor was prototyped and tested. Although extractive, this sensor was designed to be mounted directly on the stack to minimise the distance travelled by the gas from the stack to the measurement cell and therefore minimise some of the negative effects associated with extractive sensors. A modified version of the CT2000 enclosure was used to drive the QC lasers and detect and digitise the mid infrared light. A diagram of the sensor is shown in figure 4.35.

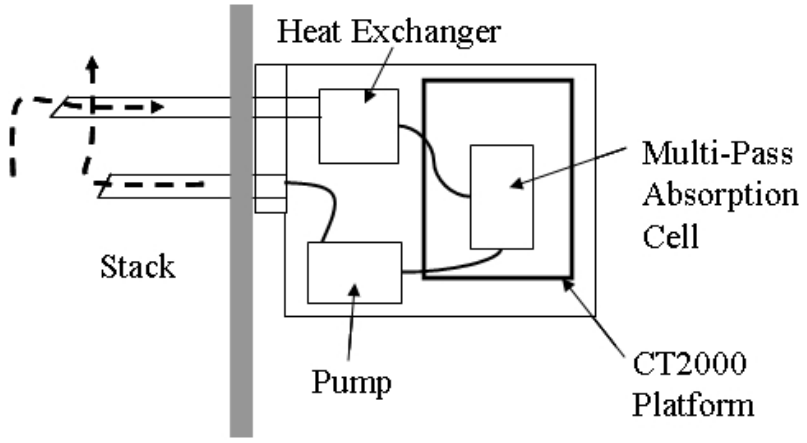

Figure 4.35: This diagram shows the local extractive, CT2100 sensor attached to an exhaust stack. A pump is used to draw the exhaust gas through a heat exchanger and into a multipass gas absorption cell. The absorption cell is mounted to a CT2000 platform, the cell is heated and is equipped with pressure and temperature sensors. The analysed exhaust gas is then returned to the stack.

A multi-pass cell was mounted to the front of the enclosure, this cell provided two configurable pathlengths by adjusting the input to the cell. One configuration provided a pathlength of 124cm, while the other was 49 cm, this allowed the concentration ranges of the sensor to be adjusted. The optical design of the cell is shown in figures 4.36 and 4.37, this type of multi-pass cell is described in further detail in section 2.4.1.

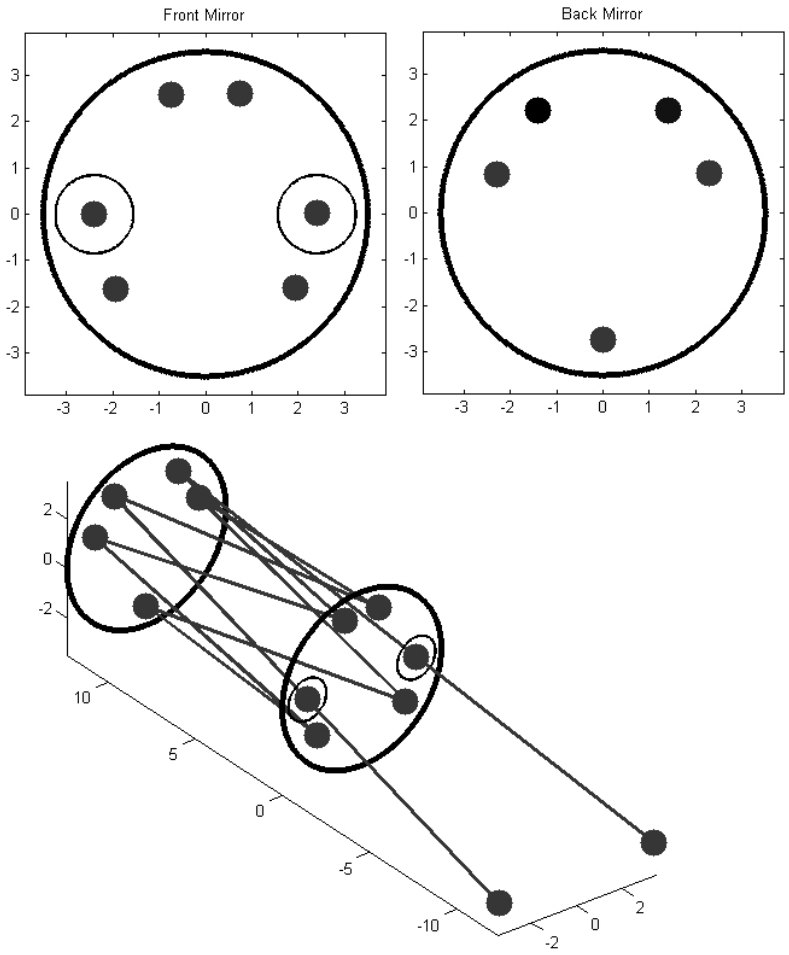

Figure 4.36: This is the 124cm configuration of the local extractive cell. The beam enters the cell at an angle to the normal allowing the beam to make 10 passes between the mirrors. This configuration allows a higher sensitivity, however the upper limits of the measurements are lower than in the short cell.

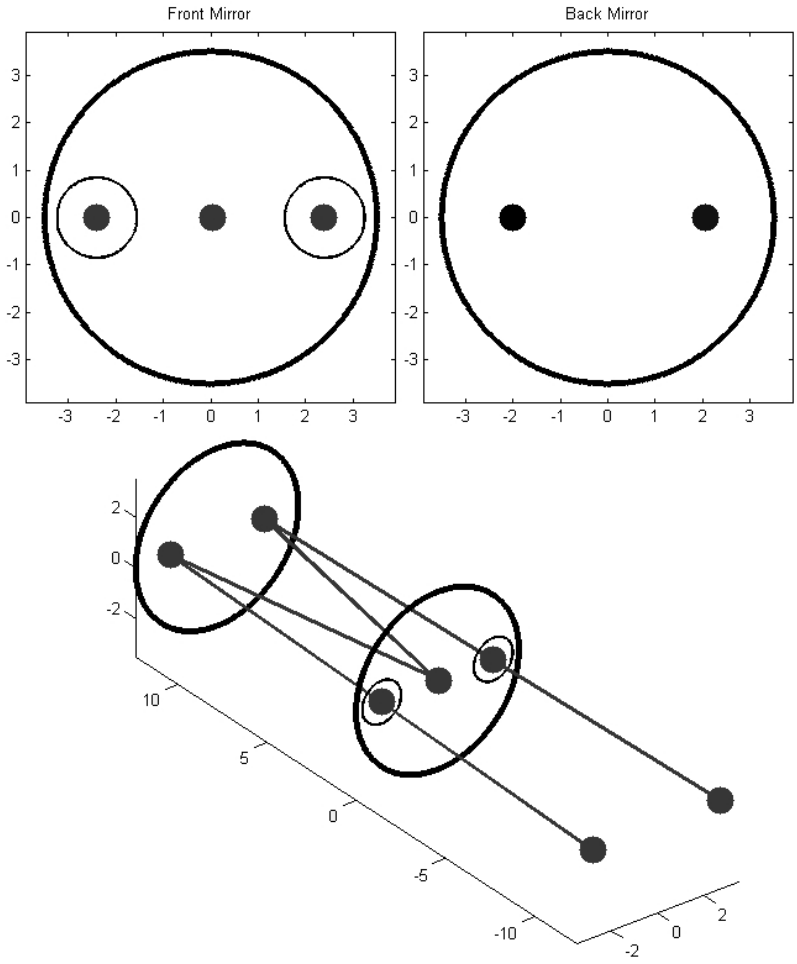

Figure 4.37: This is the 49cm configuration of the local extractive cell. The beam enters the cell normal to the back of the mirror allowing the beam to make 4 passes between the mirrors. In this configuration upper limits of the measurements are higher, however the measurements are not as sensitive as could be achieved with the long cell.

During operation the cell was maintained at a temperature greater than $165°C$ to avoid condensation on the cell surfaces. A filter was used to isolate particulate matter from the cell. Due to the often unknown and fluctuating stack temperatures a heat exchanger was included in the flow system. An external pump was used to draw stack gas through the heat exchanger and the cell. Once the gas had passed through the cell it was returned to the stack. The pressure of the cell was not controlled, however a sensor was

used to monitor the pressure, which typically stabilised at 680 Torr. The specifications of the sensor are listed in table 4.13.

Local Extractive Sensor Specification			
		Configuration	
Item	Parameter	1	2
Cell	Design	10 passes	4 passes
	Pathlength	124 cm	49 cm
NO	Detection Limit	8.98 ppm	22.72 ppm
	Resolution	6.71 ppm	16.98 ppm
	Full Range	1000 ppm	2400 ppm
NO_2	Detection Limit	3.51 ppm	8.88 ppm
	Resolution	1.02 ppm	2.58 ppm
	Full Range	350 ppm	800 ppm
CO_2	Detection Limit	0.004 %	0.003 %
	Resolution	0.003 %	0.008 %
	Full Range	5 %	12 %
SO_2	Detection Limit	2.73 ppm	6.91 ppm
	Resolution	2.19 ppm	5.54 ppm
	Full Range	1200 ppm	3000 ppm
CO	Detection Limit	12.14 ppm	30.71 ppm
	Resolution	7.19 ppm	18.19 ppm
	Full Range	2500 ppm	6000 ppm

Table 4.13: Gas measurement specification for the local extractive sensor. The CO and CO_2 measurements are performed by the same laser. Both pathlength configurations are listed.

This specification allows for the two pathlength configurations of the sensor. There are both improvements and deteriorations in the performance, the greatest contributing factor to this effect is the reduction in the temperature of the gas which effects the line strengths of the gases. The extractive sensor utilised a heat exchanger to prepare the gas sample as it is flowed into the heated gas absorption cell. The previous sensors specification was dependent upon the temperature of the gas within the stack which can vary from room temperature to over $400°C$ with different applications. The heat exchanger was designed to bring the temperature of the gas to the same temperature as the absorption cell. This allowed the sensor to be easily applied to a variety

of applications. The sensor was tested at NPL in preparation for industrial trials. The results of these tests are discussed in the following sections.

Test Results

A range of tests were performed on this sensor at NPL on all the target gases. In addition CO measurements were performed using the QC laser that would normally be used solely to measure CO_2, the near overlap of CO and CO_2 absorption lines allowed a single laser to measure the two gases. A set of linearities and a modified set of cross interference tests were used to assess the performance of the sensor.

The results of the NO_2 tests are shown in figures 4.38 and 4.39. The maximum error on the NO_2 linearity was -1.38 %. A cross interference with 5% CO_2 showed virtually no cross interference effects. Although the NO_2 test results were positive they revealed an underlying issue with the response of the sensor. This problem was caused by a combination of flow rate and presence of cold spots in the flow system. These problems were corrected before industrial trials began.

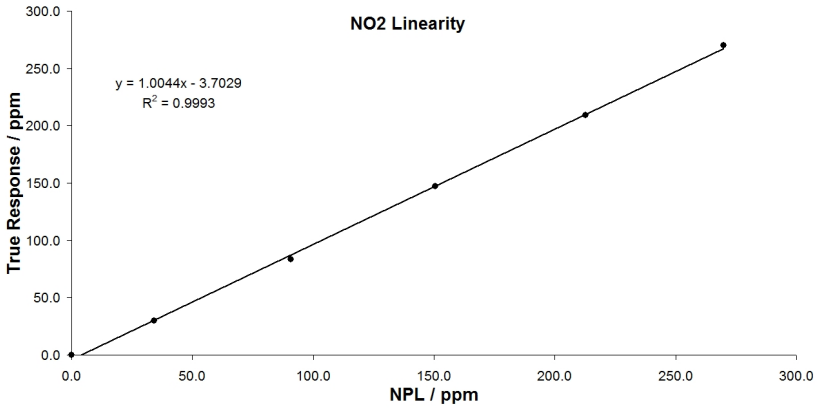

Figure 4.38: This shows the results from the NO_2 linearity. The maximum error recorded during the linearity as -1.38 %.

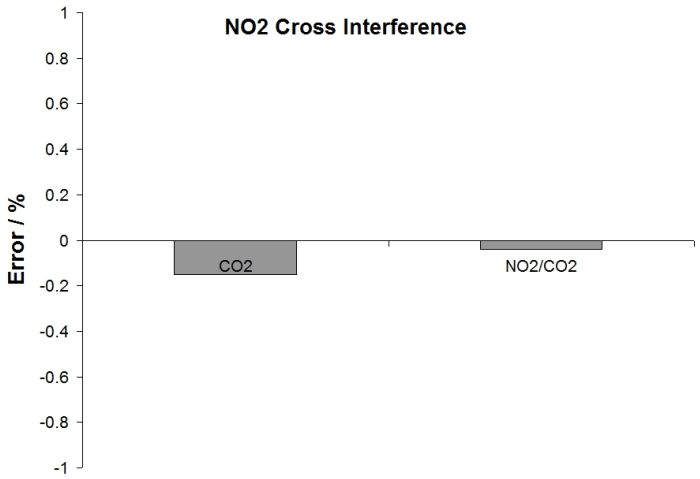

Figure 4.39: This shows the results from the NO_2 cross interference. The error from both the zero and span measurements was minimal.

The results of the NO tests are shown in figures 4.40 and 4.41. The maximum error on the linearity was 0.33 %. A cross interference with 5% CO_2 showed a -0.82 % error on the span measurement, this is significant but well within the pass range for type approval.

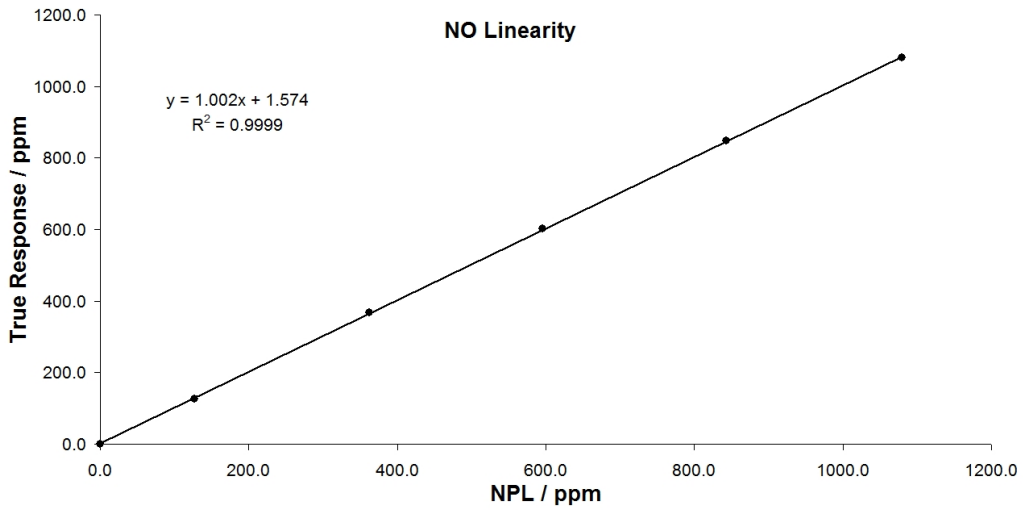

Figure 4.40: The *NO* linearity results. The maximum error is found to be 0.33 %.

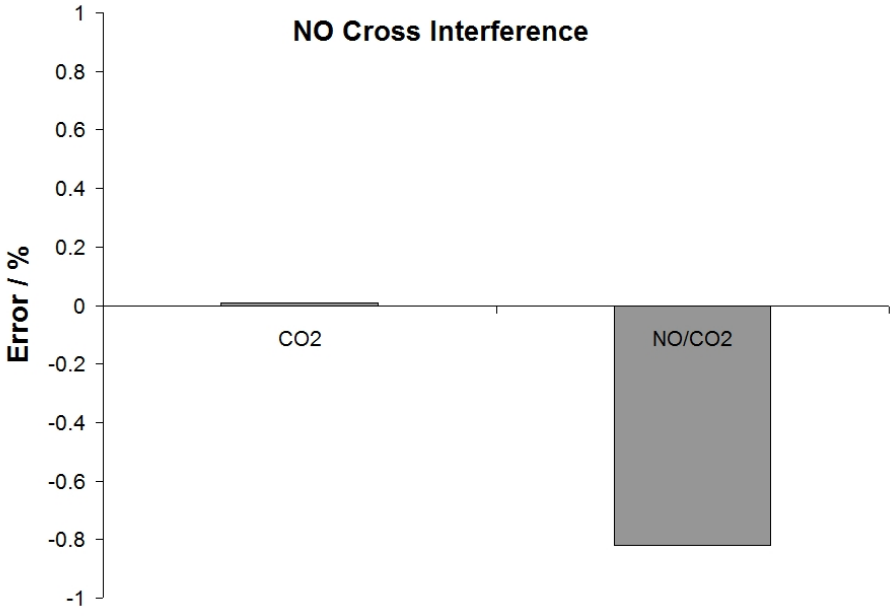

Figure 4.41: The cross interference result for *NO*. The test is passed with a span error of -0.82 %

The results of the SO_2 tests are shown in figures 4.42 and 4.43. The maximum error on the linearity was 0.94 %. An extended set of cross interference tests were performed on the SO_2 measurement. Tests on 5 % CO_2, 70 ppm CH_4 and 10 % H_2O were conducted. The CO_2 tests were passed, however the CH_4 zero test and the H_2O span test were failed. The presence of CH_4 lines in the wavelength region and the increased pathlength of the cell meant that the error was increased. This problem is unlikely to be encountered in many stacks due to the low CH_4 concentrations, however it can be solved by including CH_4 in the fitting routine. The H_2O test failure was not due to H_2O absorption lines since the zero measurement was passed, the reason for the span measurement failure is most likely due to the condensation of H_2O and SO_2 on cold spots in the flow system.

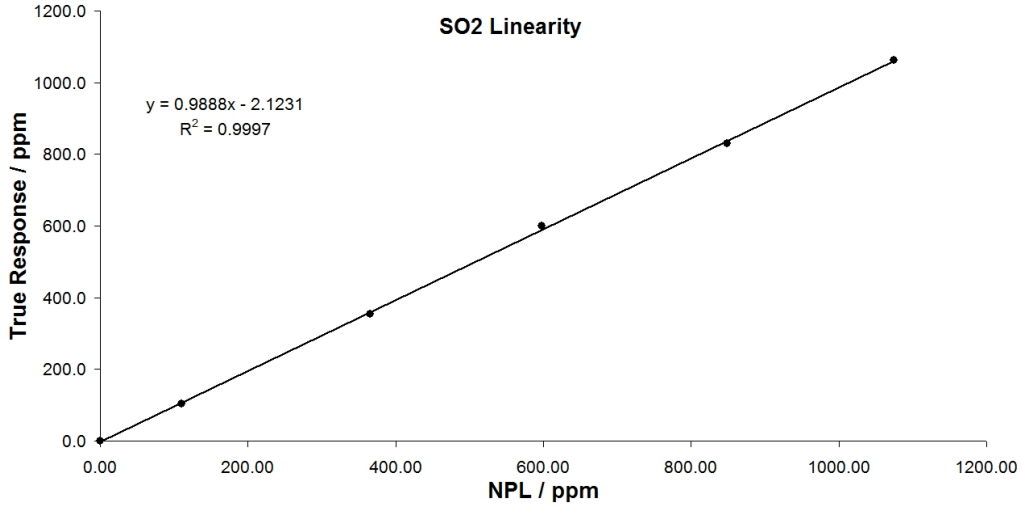

Figure 4.42: The results from the SO_2 linearity, a maximum error of 0.94 % is recorded.

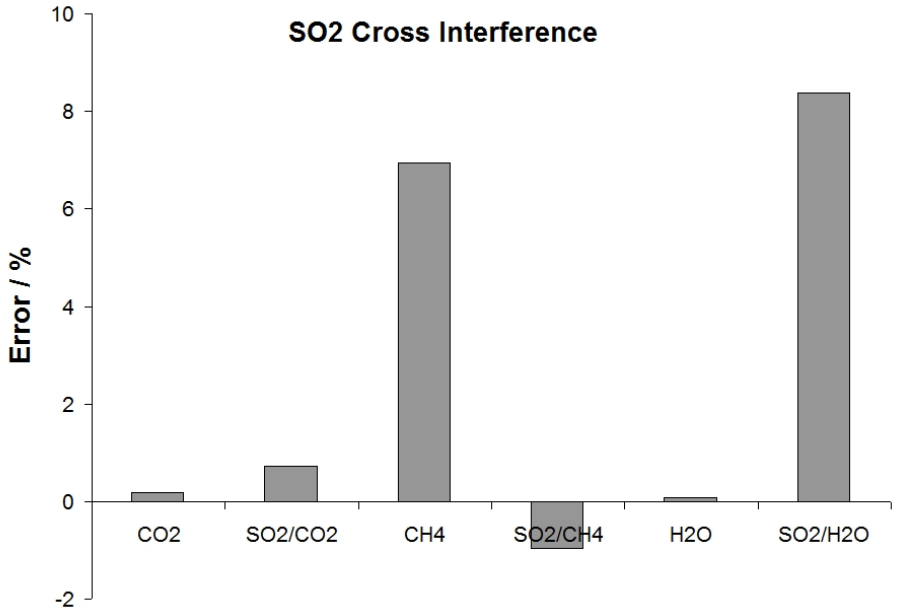

Figure 4.43: An extended set of cross interference tests on the SO_2 measurement. The test is passed successfully for CO_2, however the errors on the CH_4 zero measurement and the H_2O span measurement are both large enough to cause a failure.

The CO and CO_2 tests were performed using the same laser. The results of the CO_2 tests are shown in figures 4.44 and 4.45. The CO_2 linearity was passed with a maximum error of 1.27 %. The cross interference with CO was completed with almost no error. The cross interference results were compiled from the same data set, CO was used as a cross interferent with CO_2 and vice-versa.

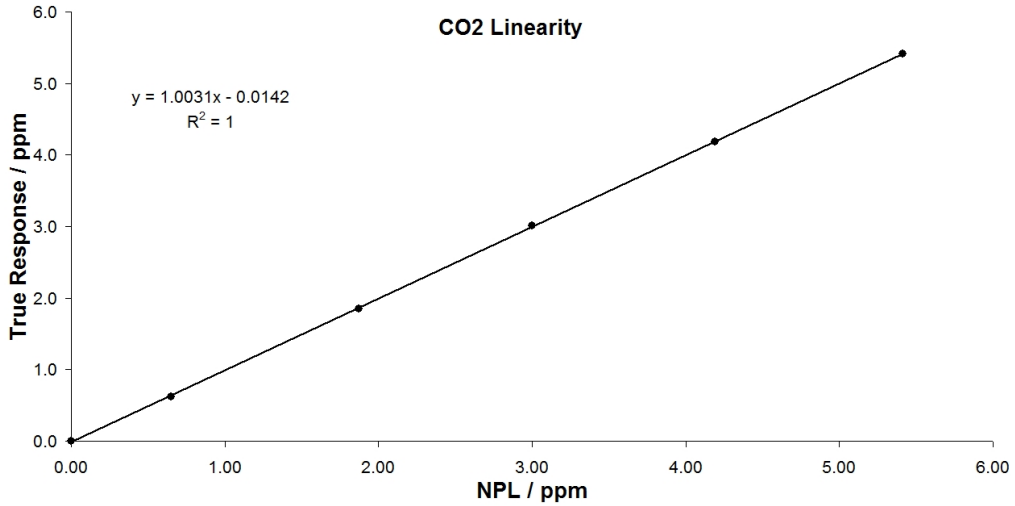

Figure 4.44: The results of a CO_2 linearity, the maximum error was found to be 1.27 %.

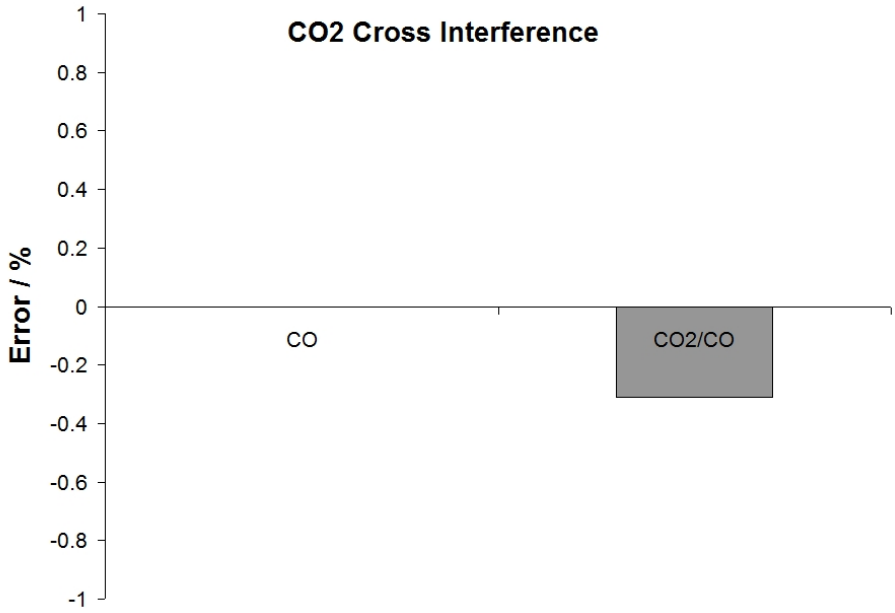

Figure 4.45: The results from a CO_2 cross interference with CO. The error is small for both the zero and span measurements even though the CO_2 and CO absorption lines overlap.

The results of the CO tests are shown in figures 4.46 and 4.47. The CO linearity was passed with a maximum error of -0.29 %. The results from the cross interference with CO_2 were not as good as the results when CO was the cross interferent with CO_2, however a pass was achieved. The fact that the CO_2 and CO absorption lines have an equal dominance in the wavelength region used and that the CO_2 had a significantly greater effect on the CO measurement than CO did on CO_2 suggests that line broadening is the most important consideration in the cross interference.

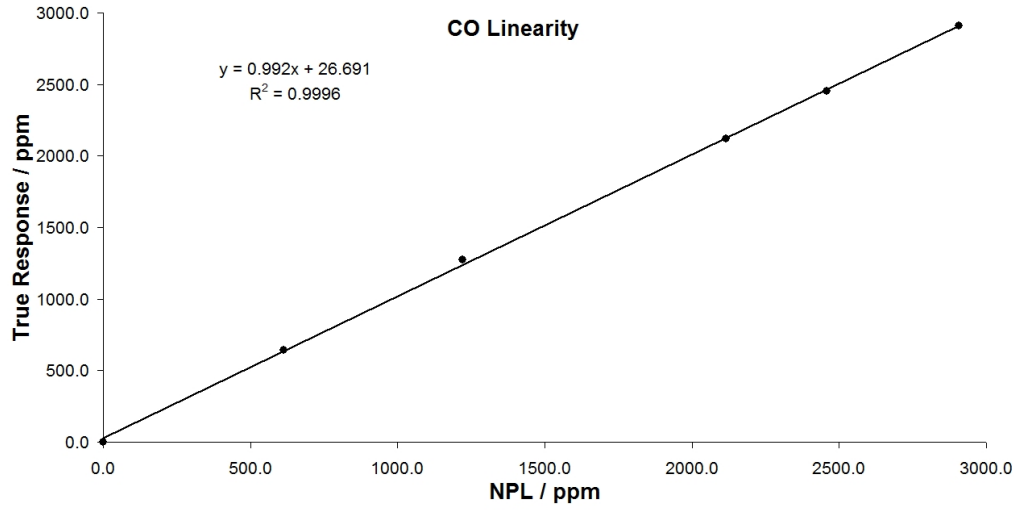

Figure 4.46: The results from the CO linearity. The maximum error was found to be -0.29 %.

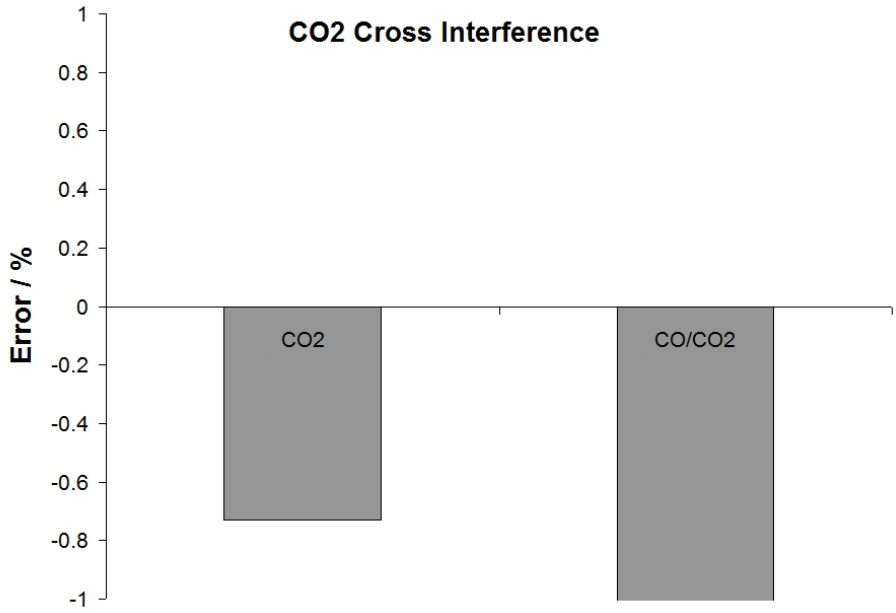

Figure 4.47: The CO_2 - CO cross interference is re-analysed to determine the effect of CO_2 on a CO measurement.

Conclusions

The test and trial results of this sensor demonstrated that it met the requirements of being both accurate and robust. The ability to reconfigure the pathlength of the absorption cell meant that the upper range of detection was not limited and the measurement range could be adjusted to meet a greater variety of applications. The extractive based design required that new components be introduced such as electrically controlled solenoid valves and robust pumps to flow the gas from the stack and back again. However, the extractive design also allowed a greater control over the condition of the gas. The pressure and temperature were both controlled through the flow system and the heat exchanger.

This design was a prototype and was not intended to be a final product. A production type sensor based on the design of the CT2100 will be developed by Cascade Technologies.

4.5 Bielefeld Measurements

These experiments were conducted at the University of Bielefeld in Germany [5]. A low-pressure flame reactor which is used for the study of the chemical processes within flames was adapted to allow QC laser measurements to be collected. Absorption spectra of methane, water and acetylene were made simultaneously for a variety of source fuels using a QC laser [6]. The simultaneous measurements of multiple lines from three gases also allowed a series of temperature measurements to made, based on the different response to temperature that each of the absorption lines under study.

The purpose of the experiments was to determine how suitable a QC laser based measurement system would be for performing low-pressure flame measurements. To the best knowledge of the author this was the first time a QC laser based measurements system was used to probe the content of flames.

4.5.1 Experimental Setup

The spectra were collected from a low pressure (50mbar) flame reactor as shown in figure 4.48.

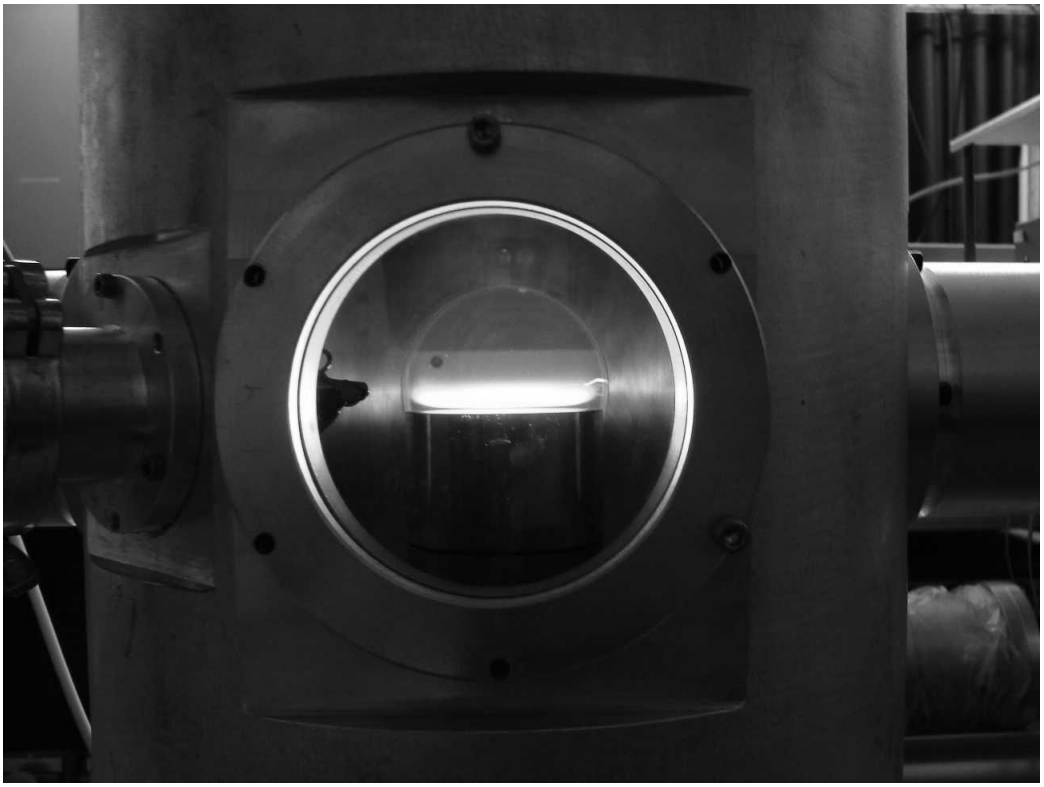

Figure 4.48: This shows the low pressure flame reactor at the University of Bielefeld. A methane fuelled flame is supported by a burner platform. The burner can be repositioned allowing different areas of the flame to be probed.

In order to increase the sensitivity of the experiments a modified version of a standard Herriott Cell was incorporated into the flame reactor, this design is described in detail in section 2.4.1. Separate entry and exit holes were drilled on opposing mirrors rather than the usual dual entry/exit hole and a 3-pass cell design was selected to limit the reflections to a plane with the reflected beams crossing at the centre of the reactor. These modifications, together with the focusing effect inherent to the mirrors maximised the spatial resolution of the measurements and allowed the detection system to be separated from the laser system which minimised the pick-up noise observed on the detector. The experimental setup is shown in figure 4.49, the burner through which the fuel was supplied could be repositioned horizontally and vertically.

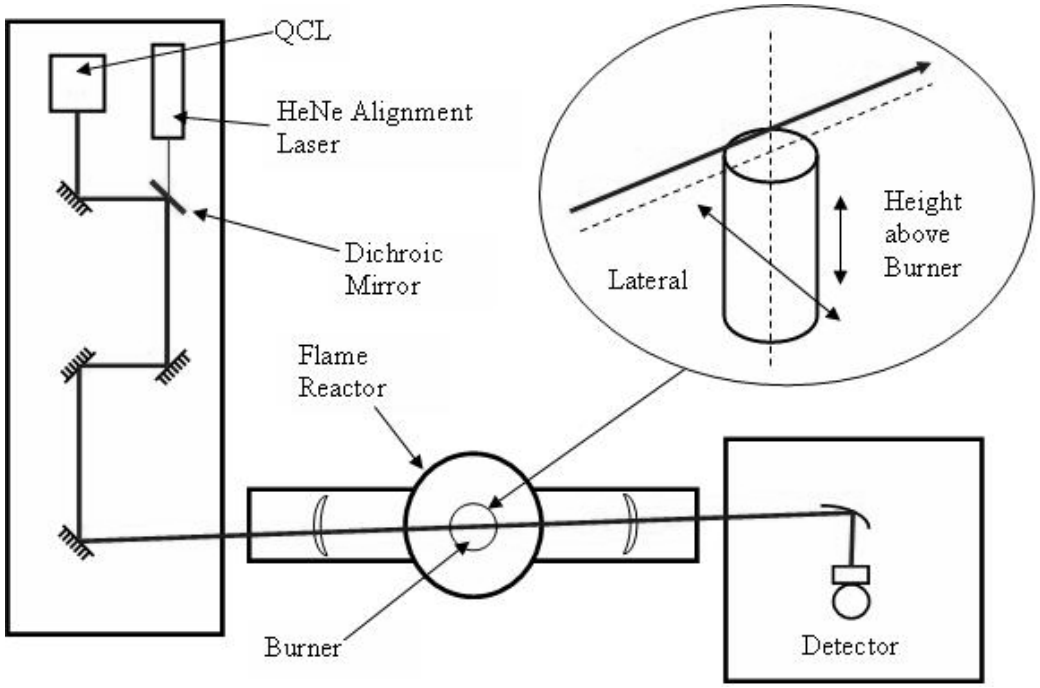

Figure 4.49: This shows the experimental setup used to perform the flame measurements. A dichroic mirror is used to co-align a HeNe laser with the QC laser allowing the system to be aligned visually. The Herriott cell mirrors are positioned within the flame reactor and allow multiple passes through a small spatial area. An off-axis parabolic mirror is used to focus light onto a detector. Within the reactor, the burner can be moved to allow different parts of the flame to be measured.

Since the burner could be manoeuvred within the flame reactor, detailed measurements of the reaction zones and boundaries could be recorded. This also allowed the flame to be completely removed from the beam path in order to remove any background absorptions from the reactor and isolate the data recovered from the flames themselves. Methane, water and acetylene were quickly identified along with an absorption line that was initially unassigned, though later attributed to acetylene [7] during QC laser measurements of a plasma reactor for the chemical vapour deposition of diamond. Due to the number of absorptions recorded simultaneously and their relative line strengths, specifically the methane absorptions, detailed temperature information could be extracted from the data. Measuring the temperature of what is similar to a plasma is very difficult to do accurately by any means,

however by observing the relative strengths of various methane lines it is possible to record temperature information. The plot in figure 4.50 shows the spectral window recorded by the QC laser used in the experiments, the plot shows a HITRAN [8] simulation of some of the absorption lines observed during the experiments.

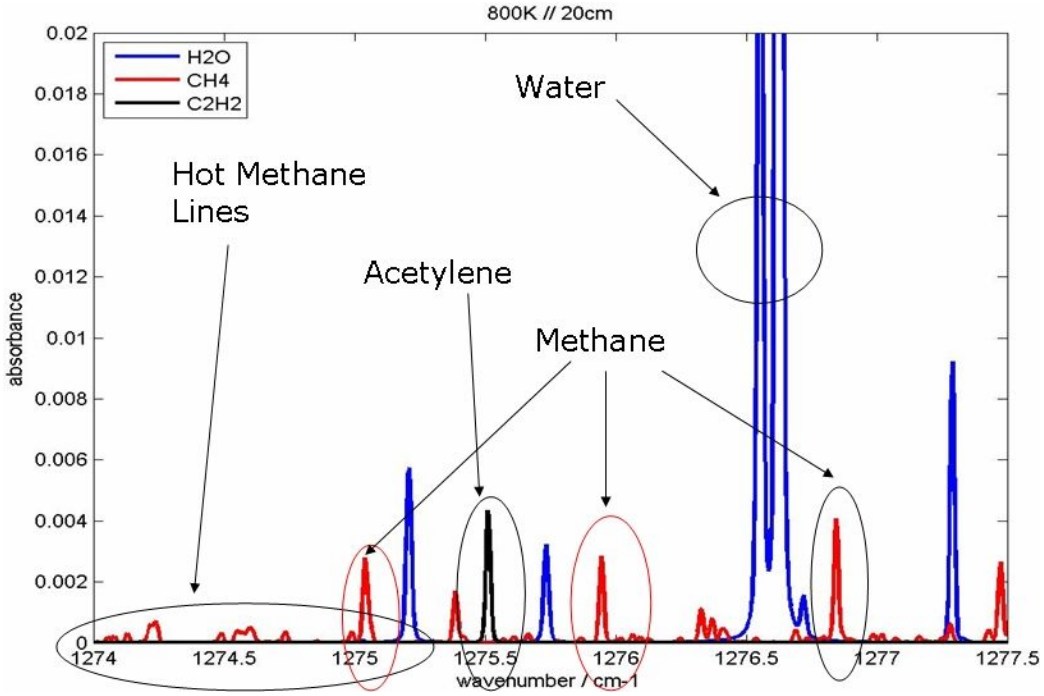

Figure 4.50: This shows a simulation of the gases found during flame reactor experiments over the spectral window of the QC laser. The pathlength used for the simulation is 20cm which is equivalent to three passes over the burner. This pathlength provides a good absorption strength balance between the various gases and their concentrations. The pressure is 50mBar and the temperature is 800K. Note that in this simulation, which is based on HITRAN data there appears to be a single C_2H_2 absorption line.

The laser used in these experiments was a $7.8\mu m$ DFB device. The spectral window that this laser accessed is shown above in figure 4.50. The laser was operated with a $1.3\mu s$ pulse length with a repetition rate of 20kHz. The QC laser beam was co-aligned with a HeNe red laser to aid alignment through the flame reactor. The beam combination was performed by means of a dichroic mirror as shown in figure 4.49. The dichroic mirror was a ZnSe

window with an appropriate optical coating to enhance the reflectivity of in the infrared region while preserving the high transmission in the visible wavelength region.

The detection system consisted of a Kolmar [9] mid-infrared detector connected through a Femto [10] pre-amplifier to a high-speed averaging digitiser. The digitiser was configured to average 20,000 pulses, this equates to a 1s measurement update rate.

4.5.2 Temperature Fitting

Due to the high-temperature conditions involved, direct measurement of the temperature within the reactor was extremely difficult. Initial observations of the generated spectra suggested that the temperature was subject to change between different areas of the flame. In order to extract concentration measurements from the recorded data it was necessary to include temperature as a fitting parameter. The methodology of the objective function used is described in section 3.7.6.

Also, due to the pressure levels the Lorentzian line shape was not a good match to the data and the Doppler broadened Gaussian contribution had to be considered. This led to the use of a Voigt profile being used to fit recorded spectra. A spectral fitting algorithm was developed to analyse the particular data recorded during this study, the application of this algorithm led to the results in the following sections.

4.5.3 Flame Measurements

An example of a QC laser pulse recorded during the study is shown in 4.51.

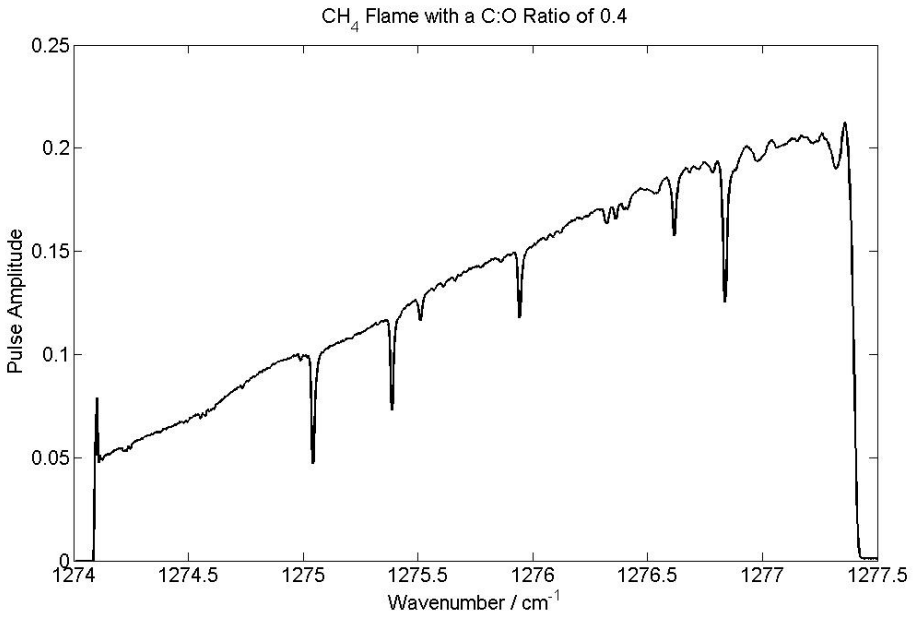

Figure 4.51: This shows an example of a QC laser pulse recorded during the study, the x axis is shown in wavenumber. In this case the data is from a CH_4 based flame with a C:O ratio of 0.4. In this pulse there are a number of absorption lines that can be observed, indicating the presence of methane, acetylene and water.

Figures 4.52, 4.53, 4.54 and 4.55, show two-dimensional plots of the analysed concentrations and temperature of a methane flame with a C:O ratio of 0.4. They were produced by removing the background absorptions from the reactor and fitting the resulting spectra with a variety of parameters, including the concentrations of the three species and the temperature of the flame. The concentrations and temperatures are averages across the section of the flame that the laser passes through. Because of the circular nature of the burner platform as shown above in 4.49, an Abel transform [11] could be used to extract a true three dimensional plot of the content of the flame.

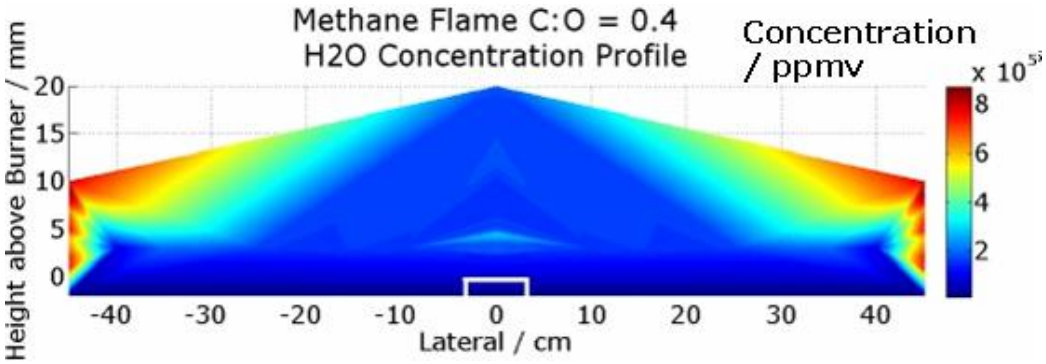

Figure 4.52: This shows a 3D profile of the H_2O concentration within the flame reactor. These measurements are from a CH_4 based flame, the majority of the H_2O is found outside of the flame. Within the flame there is am area of high concentration where the H_2O is formed.

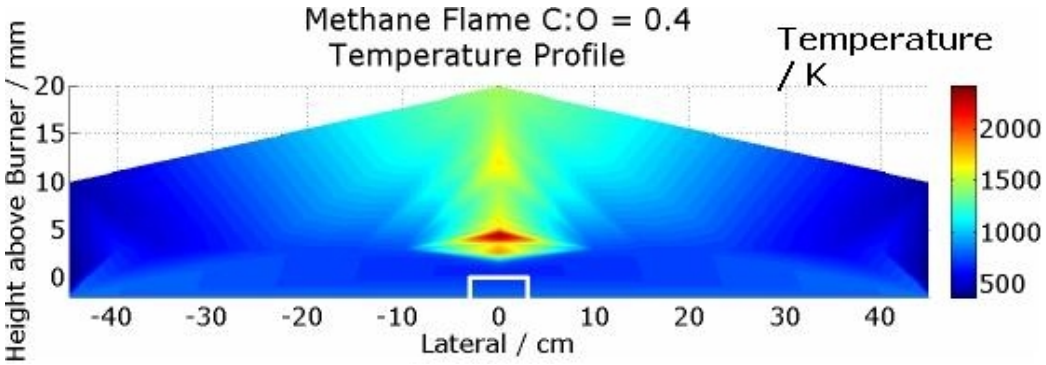

Figure 4.53: This shows a 3D profile of the temperature within the flame reactor. These measurements are from a CH_4 based flame, the temperature is calculated from the relative strengths of the various absorption lines which respond differently to temperature. The point of highest temperature is found at the centre of the flame, with the area above the flame also showing elevated temperatures.

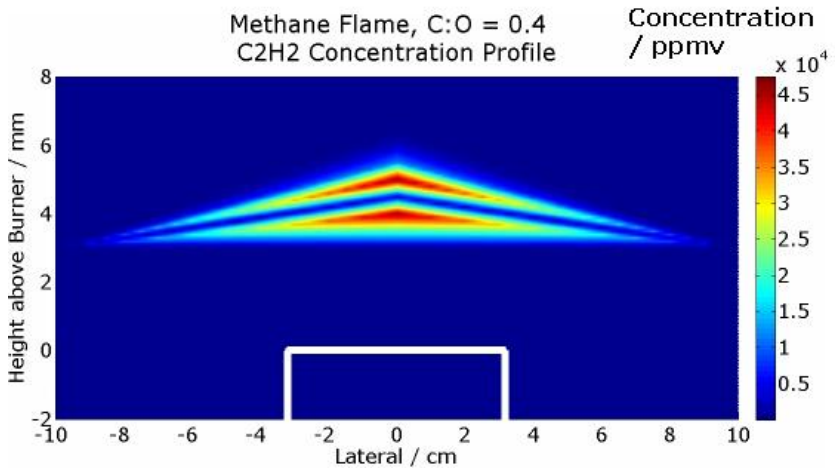

Figure 4.54: This shows a 3D profile of the C_2H_2 concentration within the flame reactor directly around the flame. These measurements are from a CH_4 based flame, the C_2H_2 is found in the flame, where two groupings are positioned above and below the peak of CH_4 concentration.

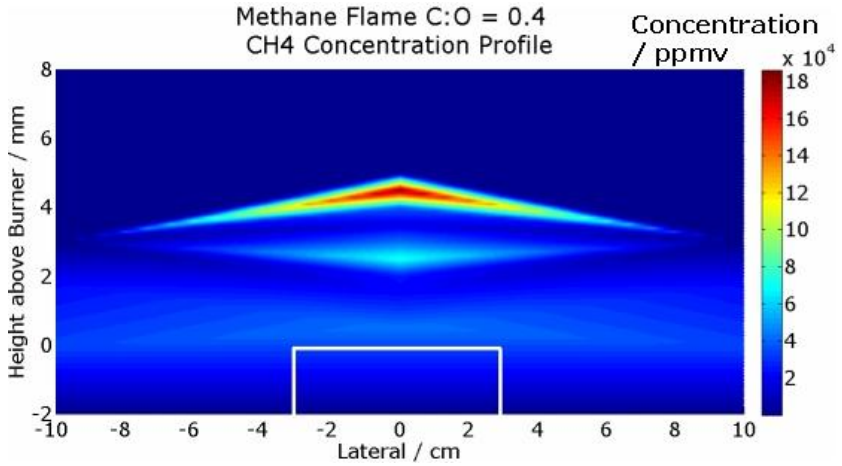

Figure 4.55: This shows a 3D profile of the CH_4 concentration within the flame reactor directly around the flame. These measurements are from a CH_4 based flame, the CH_4 is found in the centre of the flame, and is surrounded by an envelope of C_2H_2. There is no CH_4 found outside the flame indicating that it is entirely consumed.

These figures show a number of interesting results, it appears that except for a relatively small amount within the flame the vast majority of the water is contained outside the flame. The methane and acetylene concentrations are most interesting however since it appears the the peak of the methane concentration is positioned between two peaks of acetylene. Since the source fuel in this case is methane the concentration spikes show where some of the methane is converted to acetylene which then also combusts. The recorded temperature profile shows the hottest area of the burner to be the same area as the peak concentration of methane and acetylene. The reaction equation 4.8 shows a possible combustion route for the methane to acetylene reaction. This reaction would then be followed by equations 4.9 and 4.10. From these equations it is clear that the C:O ratio will influence the reaction processes.

$$2CH_4 + O_2 = C_2H_2 + H_2 + 2H_2O \tag{4.8}$$

$$2C_2H_2 + 5O_2 = 4CO_2 + 2H_2O \tag{4.9}$$

$$2H_2 + O_2 = 2H_2O \tag{4.10}$$

The plots in figures 4.56, 4.57, 4.58 and 4.59 show the absorbances of a variety of source fuel and C:O ratio flames through the central vertical axis of the flames denoted as height above burner (HAB) in mm. These graphs depict an intermediate step in the analysis of the data obtained from the flame reactor, however the comparison of the absorbances of the gases measured between the different fuels reveals some interesting information about the differing internal processes of these flames.

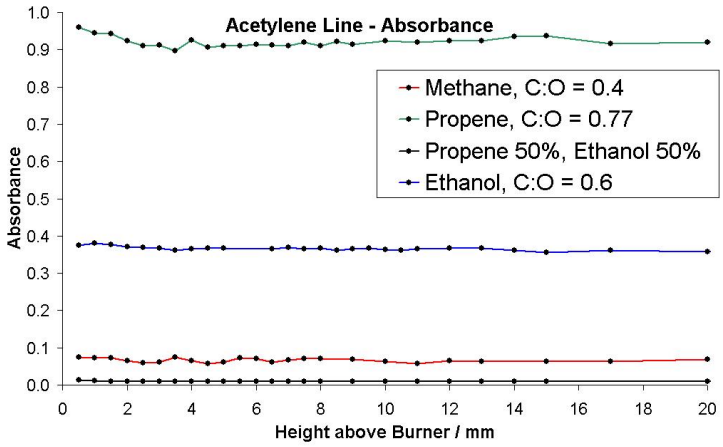

Figure 4.56: The peak acetylene absorbance of the absorption line positioned at 1275.5119 cm^{-1} with Height Above Burner (HAB) for different source fuels.

Figures 4.57 and 4.58, show the peak absorbance from methane. The difference between the lines is due to their different responses to temperature.

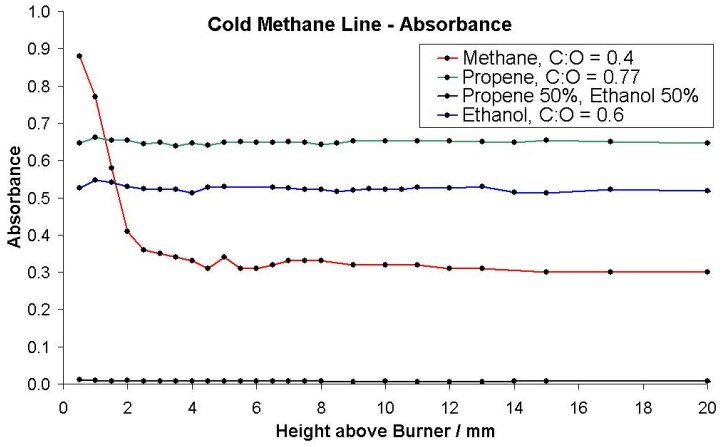

Figure 4.57: This shows the peak methane absorbance of the absorption line positioned at 1275.3872 cm^{-1} with HAB. This methane line has one of the lowest responses to temperature that could be found in the spectral window under study.

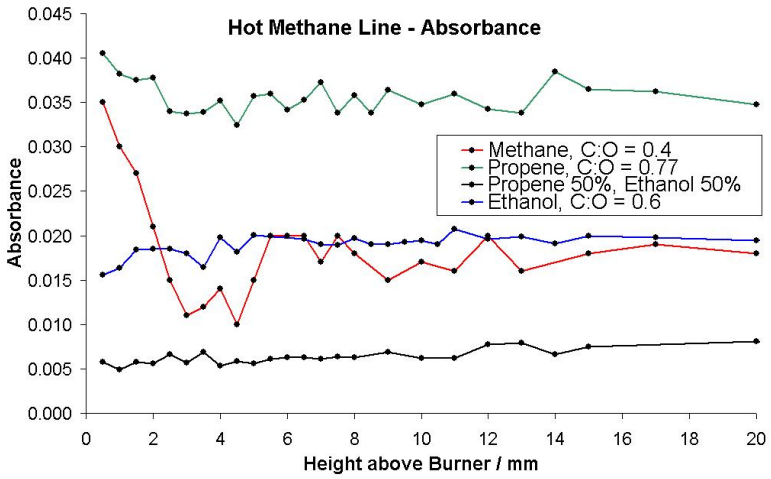

Figure 4.58: This shows the peak methane absorbance of the absorption line positioned at 1275.042 cm^{-1} with HAB. This methane line has one of the highest responses to temperature that could be found in the spectral window under study.

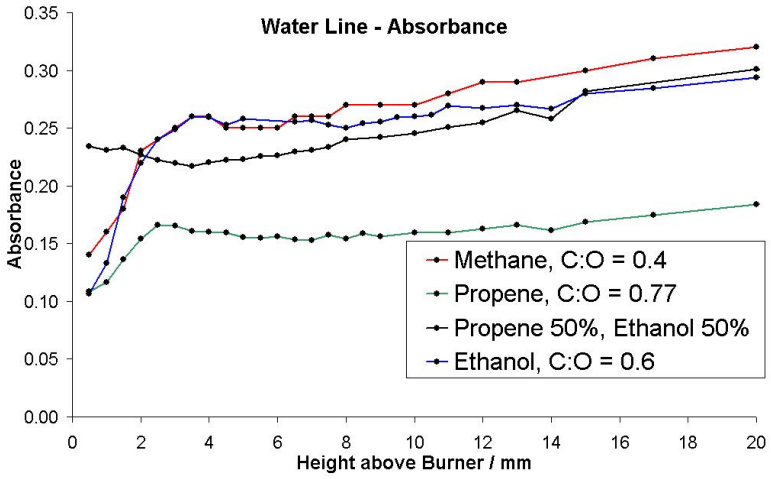

Figure 4.59: This shows the peak water absorbance of the absorption line positioned at 1276.6266 cm^{-1} with HAB.

It can be seen from comparing the absorbances of the methane flame to the two dimensional plots above how important the temperature information is in the full analysis of the spectra, however since all of the flames contain both hot and cold methane lines extracting the temperature profiles as well as absolute concentrations is possible.

Figure 4.60 below shows the absorption line that was not found in the HITRAN database. This data was collected from a methane based flame, the line was found to appear at 1275.95 cm^{-1}. The source of the unassigned line was not identified initially, the line could be found with all of the source fuels, its profile was similar in each case but with different absorption strengths.

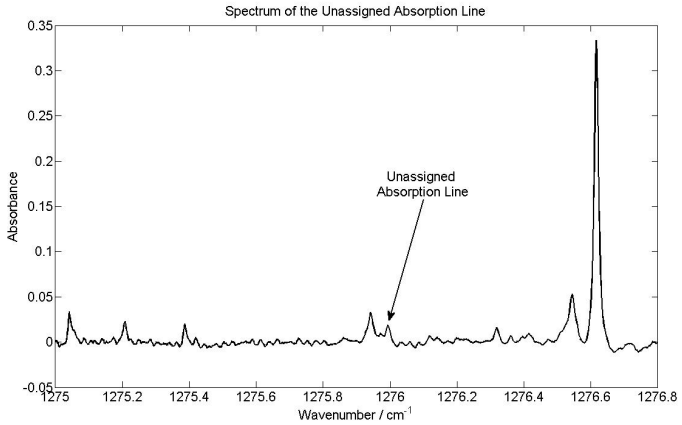

Figure 4.60: This shows a spectrum that was collected from a methane based flame with a C:O ratio 0f 0.25. The unassigned absorption line is indicated. All of the other absorption lines present can be attributed to methane, acetylene or water.

The absorbance of this line does not directly correlate with any of the other molecules that were identified, however given the high and dynamic temperature of the gases involved there was the possibility that the absorption line was a hot acetylene line. The most likely candidate at the time of the measurements was thought to be formaldehyde, however QC laser measurements performed recently have confirmed that the line can be attributed to acetylene.

4.6 Conclusions

The experimental data collected at RAL was not of a high enough quality to increase the precision or accuracy of the absorption line data compiled in HITRAN. However, within the scope of the intended application of QC laser technology to the continuous measurement of stack gases it verified that the HITRAN database was suitable for use in data analysis. The presence of optical fringing on the spectra motivated the development of spectral fitting routines capable of detecting and removing optical fringing.

The type approval tests performed at NPL proved that the spectral fitting routines developed in 3 were capable of measuring NO, NO_2, SO_2 and CO_2 under laboratory conditions. The linearity of response and susceptibility to cross-interference from other gases were proven to perform well enough to allow the use of a QC laser-based sensor to operate as a continuous emissions sensor. The field trials of a series of sensors onboard a cross channel ferry allowed the optical and analytical aspects of the sensor, detailed in chapters 2 and 3, to be further refined.

The experiments conducted at the University of Bielefeld with a low-pressure flame reactor has shown that QC lasers can be used to probe the chemical processes within flames. The ability to continuously measure multiple species with a high degree of spatial precision has allowed detailed profiles of the content of various flames to be generated.

The ability to monitor multiple absorption lines has allowed flame temperature information to be extracted from the raw data. This has been performed in a non-invasive manner and further advances the understanding of the chemical processes that occur within these flames.

References

[1] http://www.msf.rl.ac.uk/

[2] R. A. McClatchey, W. S. Benedict, S. A. Clough, D. E. Burch, R. F. Calfee, K. Fox, L. S. Rothman and J. S. Garing, *"AFCRL Atmospheric Absorption Line Parameters Compilation"*, AFCRL-TR-0096 (AFCRL, Bedford, MA, 1973).

[3] N. Martin, *"Cascade Test Report v46"*, NPL, E07020365 Cascade 01 (2007)

[4] International Convention for the Prevention of Pollution from Ships, 1973, as modified by the Protocol of 1978 (MARPOL 73/78)

[5] A. Schocker, A. Brockhinke, K. Bultitude, P. Ewart, *"Cavity ring-down measurements in flames using a single-mode tunable laser system"*, Appl. Phys. B, **77** (1), 101-108, (2003)

[6] G. Duxbury, N. Langford, M.T. McCulloch, S. Wright, *"Quantum cascade semiconductor infrared and far-infrared lasers: from trace gas sensing to non-linear optics"*, Chem. Soc. Rev., **34**, 921-934, (2005)

[7] Jie Ma, Andrew Cheesman, Michael N. R. Ashfold, Kenneth G. Hay, Stephen Wright, Nigel Langford, Geoffrey Duxbury, and Yuri A. Mankelevich, *"Quantum cascade laser investigations of CH_4 and C_2H_2 interconversion in hydrocarbon/H_2 gas mixtures during microwave plasma enhanced chemical vapor deposition of diamond"*, J. Appl. Phys., **106**, 033305. (2009)

[8] L.S. Rothman et al, *"The HITRAN 2004 molecular spectroscopic database"*, JQSRT, vol. 96, pp. 139-204, (2005)

[9] Kolmar Technologies 3 Henry Graf Rd. 9 Newburyport, MA 01950 USA, www.kolmartech.com

[10] http://www.femto.de/

[11] R. Bracewell, *"The Fourier Transform and its Applications."*, New York: McGraw-Hill., (1965), ISBN 0-07-007016-4

Chapter 5

Conclusions and Future Work

5.1 Overview

The purpose of this work was the development of intra-pulse QC laser spectroscopy and the applications of this technique. The advantages of the intra-pulse method of QC laser spectroscopy, such as the high speed generation of high resolution infrared spectra, have been discussed. Evidence of its suitability as a highly sensitive and accurate method of gas detection and monitoring has been presented in Chapter 4.

The development of QC laser based sensors, both from an optical and analytical perspective has been discussed in Chapters 2 and 3. Optical components that allow pathlengths sufficiently long enough to enable high sensitivity gas measurements have been developed. Spectral fitting routines and analysis algorithms that are capable of extracting accurate and precise gas measurements from high temperature gas mediums containing multiple species have been also been developed.

The demand for accurate gas measurements is often found in places that require instrumentation to be robust and easy to maintain, such as exhaust stacks or other industrial environments. Chapter 4 presents the results of

several significant applications. The data presented in this chapter shows that QC lasers are a preferable source for the laser based detection and monitoring of atmospheric gases and common pollutants. The performance of the sensor technology was verified at NPL before extensive industrial trials took place. The results of these trials were used to further improve the performance of the various components and hence the sensor technology as a whole.

The intra-pulse technique is capable of quickly producing high resolution spectra allowing novel research measurements to take place, such as the flame profile measurements recorded at the University of Bielefeld. There have been cases where other members of the research group have achieved high quality molecular measurements with the intra-pulse technique. Measurements of atmospheric gases [1], plasma measurements [2], car exhaust [3] have been documented.

5.2 Future Work

The immediate future work includes the further development of optical designs and analysis algorithms to provide increased improvements in sensor performance. Further details of the direction these developments may take are detailed in the section below. It is worth noting however that the results that can currently be obtained with QC laser based sensors are in many cases significantly better than competing technologies. This is not always directly because of the sensitivity that is possible but in many cases is due to the versatility of the technique.

5.2.1 Sensor Development

It is likely that future commercial research into the field of QC laser spectroscopy will centre on increasing sensitivity, selectivity, range of detection and measurement speed in an effort to produce more accurate and precise sensors. Increasing the pathlength of an absorption cell has so far been the

method used to increase the sensitivity of sensors, however an increase in pathlength results in only a linear gain in sensitivity. The mirrors that are used in astigmatic Herriott cells are expensive and increasing pathlength has other issues associated with it such as increasing volume, loss of detection range, loss of optical stability and loss of optical power and hence signal-to-noise ratio. These reasons mean that using astigmatic Herriott cells is not a very efficient method of increasing sensor sensitivity. Rather than increasing the absorption signal by extending pathlength, a more sensible approach to achieving higher sensitivities would be to lower the noise associated with the laser signals. The common sources of noise that limit the sensitivity of a sensor are optical fringing, bandwidth and nonlinear effects associated with QC laser spectroscopy.

Research into the application of QC lasers to other methods of spectroscopy may result in improvements in sensitivity without suffering the drawbacks listed above. QC lasers have been applied to cavity ringdown spectroscopy (CRDS) [4] and harmonic detection [5]. These methods of gas measurement could potentially be developed into robust gas detection products. There are cases where a sensitivity high enough to meet a performance specification can be met with an achievable pathlength. From an optical perspective, improvements to these sensors can be made by reducing the cost of the optical system. The most expensive components are the astigmatic mirrors used in long path cells. The development of absorption cell solutions that avoid astigmatic mirrors and the associated high cost will be a area of future work. Cell designs based on cylindrical mirrors [6] or Herriott cells with additional features designed to increase performance may allow similar cell performances to be achieved at lower product cost.

Sensitivity, selectivity, range of detection and speed can all be improved by further development of the analysis routines used to calculate gas composition and concentration. As more sophisticated algorithms are used to remove optical noise both the range and sensitivity of detection will be improved. This also leads to a reduced requirement for very long pathlengths. Future work will involve more sophisticated algorithms that are capable of

calculating concentration values more quickly and accurately. As the understanding of the behaviour of QC laser spectroscopy increases and the molecular databases become more accurate and comprehensive the models used to predict the appearance of absorption features will improve. The likely direction that work in this area will take is to increase the amount of information that can be directly calculated from the QC laser spectra as well as improving the prediction models.

References

[1] S. Wright, G. Duxbury, N. Langford, *"A compact quantum-cascade laser based spectrometer for monitoring the concentrations of methane and nitrous oxide in the troposphere"*, Appl. Phys. B, **85**, 2-3, 243-249, (2006)

[2] A. Cheesman, J.A. Smith, M.N.R. Ashfold, N. Langford, S. Wright, G. Duxbury, *"Application of a quantum cascade laser for time-resolved, in situ probing of CH4/H-2 and C2H2/H-2 gas mixtures during microwave plasma enhanced chemical vapor deposition of diamond"*, J. Phys. Chem. A, **110**, 8, 2821-2828, (2006)

[3] M.T. McCulloch, N. Langford, G. Duxbury, *"Real-time trace-level detection of carbon dioxide and ethylene in car exhaust gases"*, Appl. Opt., **44**, 14, 2887-2894, (2005)

[4] AA Kosterev, AL Malinovsky,FK Tittel, C Gmachl, F Capasso, DL Sivco, JN Baillargeon, AL Hutchinson, AY Cho, *"Cavity ringdown spectroscopic detection of nitric oxide with a continuous-wave quantum-cascade laser"*, Appl. Opt., **40**, 30, 5522-5529, (2001)

[5] D Weidmann, FK Tittel, T Aellen, M Beck, D Hofstetter, J Faist, S Blaser *"Mid-infrared trace-gas sensing with a quasi-continuous-wave Peltier-cooled distributed feedback quantum cascade laser"*, Appl. Phys. B, **79**, 7, 907-913, (2004)

[6] B. McManus, *"Paraxial matrix description of astigmatic and cylindrical mirror resonators with twisted axes for laser spectroscopy"*, Appl. Opt., **46**, 4, 472-482, (2007)